Generation of Intense Isolated Attosecond Pulses at 100 eV

Daniel E. Rivas

Ludwig-Maximilians-Universität
München 2016

Generation of Intense Isolated Attosecond Pulses at 100 eV

Daniel E. Rivas

Dissertation
an der Fakultät für Physik
der Ludwig-Maximilians-Universität
München

vorgelegt von
Daniel E. Rivas
aus Santiago, Chile

München, den 8. September 2016

Erstgutachter: Prof. Dr. Ferenc Krausz
Zweitgutachter: Prof. Dr. Giuseppe Sansone
Tag der mündlichen Prüfung: 17. November 2016

Abstract

Originally limited to big facilities, nonlinear optics experiments in the extreme ultraviolet (XUV) spectral region with table-top systems are becoming a reality. These fundamentally different sources arise from a process known as high-harmonic generation (HHG). In this process, intense mid-IR to UV radiation is converted into the XUV to soft x-rays spectral region when interacting with a gas medium. The broad bandwidth supported by this process additionally allows the isolation of pulses with durations in the attosecond regime. However, given the low conversion efficiency of the HHG process, reaching the necessary XUV intensities to probe nonlinear effects has proven to be a challenging task. The initial investigations in this direction have been realized with photon energies up to 50 eV, by successfully scaling the XUV pulse energy through the use of multi-terawatt driving lasers.

In this thesis, the generation and application of intense attosecond XUV-pulses in the 100 eV spectral region is presented. The XUV pulse energy increase is fundamentally enabled thanks to the development of a 16 TW optical-parametric synthesizer based on a two-color pumping technique, which provides pulse durations below two optical cycles. The achieved pulse energy, short pulse duration and the possibility to independently measure the carrier-envelope phase (CEP), makes this laser system a suitable driver of an XUV attosecond source.

Through a careful energy scaling scheme, pulse energies above 20 nJ are routinely achieved in a spectrum spanning from 70 to 130 eV. A continuous spectral region is observed in single-shot between 100-130 eV for the appropriate CEP. This allows the isolation of attosecond pulses through spectral filtering. In addition to these high energies and broadband spectra, the reproducibility and long-term stability of the XUV beam makes it suitable for its use towards applications.

As a proof-of-principle experiment, the XUV beam is focused to a measured beam size smaller than 3.1 μm, where the intensity is estimated to be above 10^{13} W/cm^2. At focus, the generation of Xe^{4+} and Xe^{5+} ions through the absorption of two photons is demonstrated. This is the first realization of such a measurement at these photon energies with a HHG source, paving the way to future attosecond time-resolved nonlinear spectroscopy of inner-shell electron dynamics.

Zusammenfassung

In der Vergangenheit war die Durchführung nichtlinearer optischer Experimente im Spektralbereich der extrem ultravioletten Strahlung (XUV) nur Großanlagen vorbehalten. Die fortlaufende Entwicklung von kompakten Hochintensitätslasern hat es jedoch ermöglicht, solche Experimente auf die Größenskala kleiner Labors zu übertragen. Diese von den Großanlagen grundlegend verschiedenen Strahlenquellen liegen dem Prozess der sogenannten „High Harmonic Generation“ (HHG) zugrunde, der Generierung höherer Harmonischen des treibenden Lasers. Während des HHG Prozesses werden die intensiven Laserpulse, deren Spektrum vom mittleren Infraroten (mid-IR) bis hin zum Ultravioletten (UV) reicht, durch die Interaktion mit einem Gasmedium in weiche Röntgenstrahlung konvertiert. Die hierbei emittierte Strahlung ist ebenfalls breitbandig, mit Pulsdauern bis in den Attosekundenbereich hinein. Der limitierende Faktor ist jedoch die geringe Konversionseffizienz, welche die für nichtlineare optische Experimente notwendige, hohe Intensität der ausgesendeten XUV Strahlung begrenzt. Bisher waren experimentelle Versuche auf Photonen-Energien bis maximal 50 eV beschränkt, welche bereits Multi-Terawatt Laser zur Erzeugung der höheren Harmonischen benötigen.

In dieser Arbeit werden die Erzeugung von intensiven XUV Pulsen mit Photonen-Energien im Bereich von 100 eV sowie die Erweiterung der nichtlinearen optischen Experimente auf solche Energien vorgestellt. Ermöglicht wird dies durch die Entwicklung eines 16 TW Synthesizers, welcher auf dem Prinzip der mit zwei Wellenlängen gepumpten, optisch parametrischen Verstärkung (OPA) basiert. Pulsdauern von weniger als zwei optischen Zyklen, hohe Pulsenergien von mehreren 100 mJ sowie die Möglichkeit zur unabhängigen Phasenmessung der Einhüllenden der optischen Trägerwelle (carrier-envelope-phase, CEP) machen den Synthesizer zum geeignet Werkzeug für die Erzeugung von intensiven XUV Attosekundenpulsen.

Mit Hilfe einer sorgfältig durchdachten Strahlführung und Strahlformung werden XUV Pulse mit Energien größer als 20 nJ im Spektralbereich von 70 bis 130 eV reproduzierbar und auf täglicher Basis erzeugt. Bei Einzelschüssen mit geeigneter Phase der Einhüllenden (CEP) ist darüber hinaus ein kontinuierliches Spektrum im Bereich zwischen 100 und 130 eV beobachtbar. Mit entsprechenden spektralen Filtern können aus diesem Bereich Attosekundenpulse extrahiert und für weitere Experimente verwendet werden. Neben der Erzeugung von hohen Pulsenergien sowie breitbandigen Spektren sind insbesondere die mit dem Synthesizer erreichte Reproduzierbarkeit sowie Langzeitstabilität der XUV Erzeugung attraktive Eigenschaften für zukünftige Anwendungen.

Als Beweis für die Anwendbarkeit der erzeugten XUV Pulse werden diese in einem beispielhaften Experiment auf einen Durchmesser unter 3,1 µm fokussiert, wodurch sich eine Spitzenintensität von mehr als 10^{13} W/cm^2 ergibt. Im Fokus befindet sich Xenon, das aufgrund der hohen Spitzenleistung eine Zwei-Photonen-Absorption erfährt und Xe^{4+} sowie Xe^{5+} bildet. Nach unserem besten Wissen ist dies die erste experimentell erfolgreich umgesetzte Anwendung solch hoher, durch HHG generierter Photonenenergien. Dieser Fortschritt ebnet den Weg für zukünftige Arbeiten im Bereich der zeitaufgelösten nichtlinearen Spektroskopie der Dynamik von kernnahen Elektronen.

Contents

Introduction

Motivation

It is hard to overstate the relevance of electron dynamics in today's developments in science and technology. Occurring in only a few attoseconds (10^{-18} s), under the right conditions, electron interactions can trigger series of events that alter their surroundings on much larger timescales. The understanding of these effects drives different research topics in physics, chemistry and biology with an impact on fundamental knowledge as well as technological developments. In spite of its importance, until recently these time-scales were unaccessible due to the insufficient time-resolution of the available tools.

Generally, in order to measure the time evolution of a certain process, two basic ingredients are needed: an instrument capable of probing the process in question and a correct timing of the instrument relative to the process. The time resolution is hence determined by the time precision of both the measurement mechanism and its relative timing. This idea has been repeatedly used throughout history, for example since the first approaches to measure the speed of light [1] or the development of the first high speed movie [2].

The extension of this approach towards dynamics of electrons, atoms and molecules was out of reach before the invention of the laser [3]. A few years after its initial development, the available pulse durations reached the femtosecond (10^{-15} s) scale [4]. With such pulses it was possible to time-resolve the breaking of molecules, gaining insight into the short-lived intermediate states created during chemical reactions. This field is nowadays known as femtochemistry [5].

In femtochemistry experiments, an initial pulse (pump) triggers a reaction while a second pulse (probe) measures a relevant variable, for example the absorption spectrum. By repeating the experiment at various delays between the pulses, a sequence of snapshots is obtained. This measurement thus retrieves the time evolution of the process, with a resolution given approximately by the duration of the pulses (and the jitter of the delay between them). This approach, termed pump/probe technique, paved the way towards the measurement of time-resolved processes in a variety of fields. However, the emission spectrum of the different laser materials used imposes a limit on the achievable bandwidth, and therefore new approaches are needed in order to reach sub-fs durations. For example a Fourier limited pulse of 100 as in duration needs a bandwidth of 18 eV. To reach this, photon energies at least in the extreme ultraviolet (XUV) spectral region are needed, where no lasing materials are available.

The coherent conversion of laser radiation into the XUV spectral region is possible by means of a process known as high-harmonic generation (HHG) [6, 7]. In traditional nonlinear optics,

harmonics of the fundamental driving frequency are generated with decreasing efficiency as the harmonic order increases [8]. However, when the driving electric field becomes comparable to the inter-atomic Coulomb field ($> 5 \times 10^8$ V/m), an efficiency *plateau* is reached. This constant efficiency is kept over many orders, allowing the generation of a broadband XUV to x-ray spectrum. This effect, in conjunction with few-cycle driving lasers allows the generation of isolated pulses with attosecond durations [9]. With these, the first steps towards measuring time-resolved electron dynamics have been achieved, establishing the field of attosecond physics [10]. Though, due to the low conversion efficiency of the HHG process, most of these experiments have been achieved in a XUV-pump/laser-probe (or vice versa) configuration.

Though opening a wide range of new research topics, the limited bandwidth of the intense laser pulses still restricts the possible observable processes due to its duration in the few-fs scale and comparatively low photon energy. Pump/probe studies with attosecond resolution using only the XUV radiation would allow to study a whole new variety of processes, in addition to a direct temporal characterization of the pulses. Intrinsically, a pump/probe scheme involves the interaction with at least two photons, which in many cases makes it intensity dependent. However, reaching the necessary intensities for such experiments with an attosecond time resolution is an extremely challenging task, and several paths are being investigated towards this goal.

A fundamentally different approach to this problem is taken at free-electron laser (FEL) facilities, where coherent XUV and x-ray radiation is emitted by relativistic electrons from conventional RF accelerator through self-amplified spontaneous emission [11–16]. In these facilities, experiments in a XUV-pump/XUV-probe configuration have been widely demonstrated [17–20], but until now only with a time resolution on the order of tens of fs. Limited both by the achievable pulse duration and intrinsic timing jitter, an attosecond time resolution still needs to be demonstrated and is a topic of active investigation [13, 21, 22]. Moreover, the great complexity and costs associated with these infrastructures strongly limits their use and availability for researchers around the world, with only a few facilities in operation today.

In contrast to traditional gas-based HHG, an alternative high-harmonics source has been realized thanks to the availability of lasers capable of producing extreme intensities [23]. Dubbed surface high-harmonic generation (SHHG), the frequency conversion is based on the coherent oscillation in the relativistic laser field of an overdense plasma surface, arising from laser-induced ionization of solid targets. This novel approach is scalable with driving-laser intensity, enabling an increase in both the overall efficiency and obtainable photon energies [24, 25]. At a lower laser-intensity regime, attosecond control of the XUV emission has been demonstrated [26], as well as its application towards XUV-pump/XUV-probe experiments [27–29]. However, the isolation of attosecond pulses is not possible in this regime without the appropriate gating mechanisms [30]. The generation of isolated attosecond pulses through the use of high laser intensities still lacks demonstration [25].

Despite the overall low conversion efficiencies of the HHG in gases, by driving the process with more energetic lasers these sources have been shown to reach suitable intensities for pump/probe experiments in the XUV spectral region [31–34]. Still, these experiments were realized at photon energies in the range of 15-50 eV, which is lower than what has been achieved.

For the currently available high-energy laser systems (with a central wavelength of approximately 800 nm) the generated photon energies can be increased by using gases with higher ionization potential, though at the cost of even lower efficiency [35]. For this reason, no HHG sources have been shown to achieve the necessary intensity for pump/probe experiments at photon energies above 50 eV.

A particularly interesting region is that close to 100 eV, which has been actively investigated since the early measurements at synchrotron facilities in the 60's [36, 37]. In comparison to lower photon energies, inner-shell electron dynamics take place during photo-absorption of 100 eV photons. For instance, an active topic of research is the broad absorption resonance of the 4d transition in xenon. This initial observation has not only driven fundamental research [38, 39], but its understanding has been motivated by industrial applications towards the development of sources for XUV-lithography [40–42]. Recently, nonlinear photo-ionization experiments at FELs have revealed additional features of this resonance [43–45], but until now the attosecond dynamics of these processes have only been studied theoretically [46, 47].

Activities at MPQ

The Light Wave Synthesizer 20 (LWS-20), a laser system capable of delivering high energy pulses in only a few optical cycles, has been in continuous development at the Max Planck Institute for Quantum Optics (MPQ) in Garching [48]. Based on the optical parametric chirped-pulse amplification (OPCPA) technique, the system delivered pulses containing 130 mJ in energy with FWHM durations of 7.9 fs, thus reaching a peak power in the order of 16 TW, making it at the moment the most intense few-cycle laser ever demonstrated. These characteristics make the system an appropriate driver to scale the generated pulse energy of the HHG process, thus reaching the necessary flux for nonlinear XUV applications.

The first steps achieved with this driver laser towards XUV-pump/XUV-probe experiments with attosecond resolution have been taken both with a SHHG source and through gas HHG. In the first case, the necessary steps towards isolated attosecond pulses were studied numerically and experimentally [49, 50]. This approach, despite being quite promising goes beyond the scope of this thesis and will only be mentioned when relevant. On the other hand, the feasibility of using the system for HHG from gases is reported in reference [51]. In this preliminary investigation, the design and construction of the harmonic beamline was accomplished, along with the demonstration of an XUV attosecond pulse train arising from neon. This constitutes the initial milestone from which this thesis is based on.

In order to generate an isolated attosecond pulse, an additional temporal gating method is needed; namely an external mechanism which temporally limits the harmonic emission to less than an optical cycle[1]. In this work, the approach is to drive the HHG process with a sub-two-cycle pulse, which means under 5 fs for the LWS-20 central wavelength. This translates

[1] References [52, 53] provide an overview of the different gating mechanisms and the corresponding main results achieved through HHG in gases.

to an extension of the laser amplifier's bandwidth, which is achieved by using multiple pump wavelengths [54, 55].

Outline

The main topic of this work is the demonstration of a broadband HHG-based source centered at 100 eV, with intensities that allows pump/probe experiments with attosecond temporal resolution. This source provides an additional tool for the study of inner-shell electron dynamics in a time-resolved manner. The results presented are divided into three main topics: the LWS-20's pulse duration upgrade, the energy scaling of the XUV source and its applicability to XUV-pump/XUV-probe experiments.

In chapter 1 the reduction of the LWS-20's pulse duration to sub-5-fs is presented, which is achieved while maintaining its peak power. First the basic ideas and experimental steps necessary for this upgrade are discussed. This includes a description of both the pump laser two-color upgrade and the corresponding extension of the OPCPA-based amplifier. The main operation parameters of the system are then shown, along with its temporal characterization.

Chapter 2 describes the necessary conditions needed to efficiently drive the HHG process with the LWS-20 system. The theoretical background of the HHG process is first summarized, in order to discuss the experimental parameters relevant to the process, particularly the role of ionization. The energy scaling scheme used in the experiments is presented as well, where the use of long focal-length optics is required.

The main properties of the experimental setup used to realize the scaling scheme are described in chapter 3. The over 30 m long vacuum beamline is described, along the experimental parameters relevant for HHG. This includes the NIR focus characterization, on-target temporal characterization, the HHG target and the basic XUV characterization devices.

In chapter 4 the main properties of the high-energy HHG source are presented, along with its optimization procedure. Particular emphasis is placed on the experimental conditions necessary for good stability, high pulse energies and the isolation of attosecond pulses.

The proof-of-principle experiment towards XUV-pump/XUV-probe measurements is described in chapter 5. First the XUV beam focus is characterized through a novel technique in order to give an estimate of the achieved intensities. This is followed by the generation of Xe^{4+} and Xe^{5+} through two-photon absorption, which confirms the applicability of the source towards nonlinear XUV experiments.

Finally the main results of the project are summarized in chapter 6, along with an outlook towards the future possibilities with the LWS-20 and the XUV source.

The description of the LWS-20 system along its application towards attosecond and laser-plasma physics has been submitted for publication [56]. The main results on the XUV source and its application on nonlinear optics at 100 eV are in preparation to be submitted in two different manuscripts [57, 58]. All of these results have additionally been published in various proceedings, which are summarized at the end of the text.

Chapter 1

The LWS-20 sub-5-fs upgrade

The initial step towards the goal of generating intense isolated attosecond pulses is the reduction of the pulse duration of the LWS-20 system to under 5 fs. In this chapter, the approach to achieve this is presented, starting with the description of the general principles of broadband amplification through OPCPA and two-color synthesis. Following this, the LWS-20's upgraded setup is shown with a description of the broadband seed generation setup, the two-color pump laser and the synthesis process. In the final section the temporal compression and characterization scheme is shown, along with the single-shot measurement of the pulse duration and carrier-envelope phase (CEP).

1.1 Optical parametric chirped pulse amplification

1.1.1 Basic Principles

Growing interest in increasing the peak intensities of laser pulses while maintaining a few-cycle pulse duration lead to the development of optical parametric amplification (OPA) [59]. In comparison to the standard laser amplification, this technique allows the amplification of ultra-short pulses from the MIR spectral region to the UV while maintaining bandwidths supporting pulse durations of only a few cycles[1].

This process is generally described through the use of coupled-wave equations (see for example [61], on which the following section is mainly based). OPA is a special case of difference-frequency generation, a second-order nonlinear process, where the interaction of an intense pump of frequency ω_p and a seed of frequency ω_s in a nonlinear medium of second-order susceptibility $\chi^{(2)}$ (which for a given orientation determines d_{eff}), an idler wave of frequency ω_i is generated (see figure 1.1). Due to energy conservation the angular frequency of these three waves are related by

$$\omega_p = \omega_s + \omega_i. \tag{1.1}$$

Because of this conservation, the difference in energy between pump and idler is added to the seed, amplifying it as the idler field grows. Under the assumption of no pump depletion,

[1] A summary of some of the state-of-the-art OPA-based laser systems can be found in reference [60].

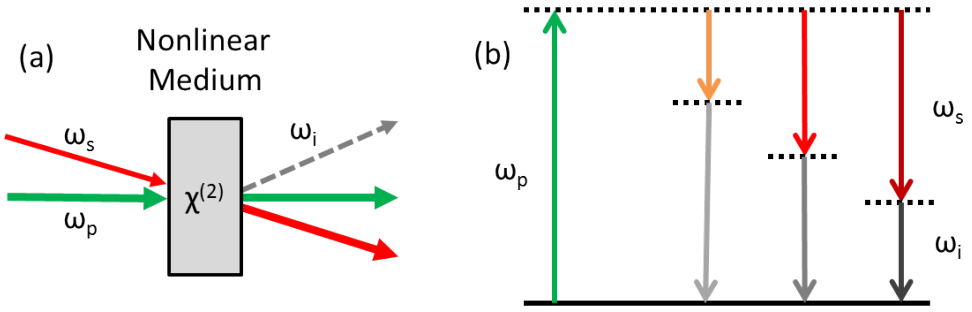

Figure 1.1: (a) Through the interaction between an intense pump (frequency ω_p) and a weak seed (frequency ω_s) an idler wave (frequency ω_i) is generated and the input seed is amplified. (b) The pump, seed and idler satisfy the energy conservation relation $\omega_p = \omega_s + \omega_i$.

a slowly-varying envelope, and that propagation occurs in the $+z$ direction, the electric field amplitude is written as $E(z,t) = Ae^{i(kz-\omega t)}$ and the following coupled wave equations for the seed and idler amplitude can be obtained:

$$\frac{dA_s}{dz} = i\frac{2\omega_s^2 d_{\text{eff}}}{k_s c^2} A_p A_i^* e^{i\Delta kz}, \tag{1.2a}$$

$$\frac{dA_i}{dz} = i\frac{2\omega_i^2 d_{\text{eff}}}{k_i c^2} A_p A_s^* e^{i\Delta kz}, \tag{1.2b}$$

where A_s, A_i and A_p are the corresponding amplitudes for the seed, idler and pump respectively, k_s, k_i and k_p are the corresponding wave-vectors, c is the speed of light, and Δk is the wave-vector mismatch, given by:

$$\Delta k = k_p - k_s - k_i. \tag{1.3}$$

Assuming only the pump and seed are present at the input of the crystal ($A_i = 0$), the coupled wave equations can be solved to obtain the intensity gain [62]:

$$G = 1 + (gL)^2 \frac{\sinh^2(\sqrt{(gL)^2 - (\Delta kL/2)^2})}{(gL)^2 - (\Delta kL/2)^2}, \tag{1.4}$$

where L is the medium length,

$$g = |A_p| \frac{\omega_s \omega_i}{c^2} d_{\text{eff}} \sqrt{\frac{1}{k_s k_i}} = 4\pi d_{\text{eff}} \sqrt{\frac{I_p(0)}{2\epsilon_0 n_p n_s n_i c \lambda_s \lambda_i}}, \tag{1.5}$$

is the gain coefficient and

$$I_p(0) = \frac{1}{2}\epsilon_0 c n_p |A_p(0)|^2, \tag{1.6}$$

is the input pump intensity.

In this formalism the finite pulse durations are not taken into account. Because the main interest of OPA is the amplification of a broadband seed, the Fourier limited pulse duration is in general orders of magnitude smaller for the seed in comparison to the pump. For the amplification process to take place efficiently, both pump and seed pulses need to overlap as they propagate through the crystal and therefore the seed pulse duration needs to match the pump pulse duration. This is achieved by temporally stretching the pulses through the addition of a temporal chirp before the amplification stage [63]. When this is done, the technique is named OPCPA.

From equation 1.4 it can be seen that the amplifier gain depends on three parameters: the gain coefficient (proportional to the square-root of the input intensity), the medium length and the wave-vector mismatch. Increasing both the medium length or the pump intensity, or decreasing the Δk would result in higher gains.

The pump intensities necessary to increase the amplification gain can be achieved by using a short pump pulse duration and/or by increasing its energy. Reducing the pulse duration of the pump can make the synchronization with the seed very challenging. On the other hand, using longer and more energetic pump pulses creates an additional challenge in the stretching and compression of the seed. However, in either approach the pump intensity is ultimately limited by the damage threshold intensity of the amplifier medium (though in general, this intensity threshold is higher for shorter pulses, thus allowing a higher gain [64]).

Alternatively, increasing the medium length allows for higher gains as shown in equation 1.4. Knowing that the gain is not constant as a function of ω_s, increasing the medium length results in a narrower spectral gain window . Consequently, for a fixed medium length and pump intensity, Δk should be minimized for the broadest bandwidth possible in order to have high-gain broadband amplification. Additionally, the pump depletion has been assumed negligible, but saturation through depletion additionally helps to increase the amplification bandwidth.

1.1.2 Phase-matching

For broadband phase-matching two different parameters are of relevance: the crystal and the noncollinear angles. To understand their effect, the wave-vector mismatch can be written as:

$$\Delta k = k_p - k_s - k_i = \frac{n_p \omega_p}{c} - \frac{n_s \omega_s}{c} - \frac{n_i \omega_i}{c}. \tag{1.7}$$

This equation cannot be fulfilled under normal conditions, so in order to achieve phase-matching birefringence in the amplifier crystals is necessary. Then phase-matching is achieved by choosing the pump polarization along the fast axis. For BBO, the crystal used in the LWS-20's amplifiers, $n_e < n_o$, so for type-I configuration we have:

$$\Delta k = \frac{n_p^e(\theta) \omega_p}{c} - \frac{n_s^o \omega_s}{c} - \frac{n_i^o \omega_i}{c}, \tag{1.8}$$

where θ is the angle between the crystal axis and the wave-vector. This parameter allows to change the k_p while keeping the k_s and k_i constant, thus selecting the phase-matching wavelength.

Additionally, an angle α can be added between the pump and seed. This angle is known as the noncollinear angle and therefore when using this technique the amplification is named noncollinear optical parametric chirped-pulse amplification (NOPCPA) or simply noncollinear optical parametric amplification (NOPA). These names will be used indistinctly in what follows. For this case the wave-vector mismatch can be written as:

$$\Delta k = \sqrt{k_p^2 + k_s^2 - 2k_p k_s \cos\alpha} - k_i. \tag{1.9}$$

This second angle allows an additional spectral bandwidth extension. Experimental details regarding phase-matching with the LWS-20 system can be found in reference [65] and the final results of the amplification process are summarized in section 1.3

1.1.3 Optical parametric synthesis

The previous version of the LWS-20 system provided sub-8-fs pulses, which corresponds to a wavelength range of approximately 700-1000 nm, amplified by the second harmonic (532 nm) of a Nd:YAG pump laser. The pulse energy reached a value of 130 mJ through amplification in two sequential NOPA stages. The possibility of increasing the bandwidth towards shorter pulse durations was investigated by adding additional stages which could address different spectral regions. This was achieved by using the pump beam in a different alignment configuration [66] or by pumping at different frequencies [54]. This two-frequency (two-color) pump approach proved to be highly successful, reaching a bandwidth of 575-1050 nm, which supports less than two cycles in duration. This was possible by additionally pumping with the third-harmonic (355 nm) of the pump laser, amplifying between 575-700 nm. This approach is named optical-parametric synthesis (OPS) or sequential-OPS.

In a parallel development, motivated by the lack of multilayer dispersive mirrors covering more than a full octave, optical synthesizers have demonstrated the possibility to compress extremely large bandwidths [67]. By separating the beam in separate spectral components, the dispersion management can be realized separately at each channel, before recombining. This approach, which has been shown to compress bandwidths of over 2 octaves, has lately been proposed to be used in conjunction to OPA, with the aim of having both the high amplification capabilities and the broad bandwidths [68, 69]. This approach, named parallel-OPS, holds great promise though until now its application remains to be demonstrated.

Given that the bandwidth achieved by the two-color pump approach can be compressed directly [70, 71], for the upgrade of the LWS-20 system there was no need of separating the beam into different spectral channels. Therefore the sequential-OPS approach is taken, which however is limited in its scalability in bandwidth. Nevertheless, as described in the next chapter, this wavelength range is enough for the goal of generation of isolated attosecond pulses.

The LWS-20's 5 fs upgrade consists of the extension of the two-stage two-color proof of principle experiment to a four-stage amplifier and the corresponding dispersion management. The amplifier stages are described in the following sections and further details regarding phase-matching and their modeling can be found in reference [72]. The details regarding the dispersion management in addition to the systems temporal contrast are described in reference [70, 71].

1.2 The LWS-20's experimental setup

1.2.1 The front-end

A schematic of the upgraded LWS-20's experimental setup is shown in figure 1.2. The system starts with a broadband Ti:Sa oscillator (Rainbow, Femtolasers) which generates pulses with a bandwidth supporting 7.8 fs in duration. These pulses are split (60:40) in order to generate the broadband seed in the system's 'front-end' and the high energy pump beam respectively. These beams are then combined in the amplification stages, where the energy of the pump is transfered to the broadband seed through the NOPA process.

The 'seed' portion of the oscillator pulses are fed into a 1 kHz, 9-pass, chirped-pulse amplification (CPA) (Femtopower compact pro, Femtolasers) which generates pulses with an energy of 1 mJ and down to 24 fs in duration. These pulses are broadened in a neon-filled hollow-core fiber (HCF), reaching a bandwidth supporting down to 4 fs in duration with pulse energies up to 400 μJ (see figure 1.3). Additionally, a cross-polarized wave generation (XPW) setup can be used after the HCF in order to improve the pulse contrast and additionally reduce phase modulations, making the compression process faster. When the XPW setup is in use, the pulse energy is reduced by an order of magnitude approximately.

The seed is stretched to 100 ps by adding a negative phase through a grism stretcher [70]. The stretcher is designed in accordance with two goals. First, the compression after amplification should be realized with a high throughput, in order to maximize the energy for experiments. In general a grating compressor supporting the amplified bandwidth (440 nm), which adds negative group-delay dispersion (GDD) has a reduced transmission. In order to achieved this goal, the stretcher was design to add negative GDD such that the compression is carried out with AR-coated bulk material and chirped mirrors. As a consequence, after stretching approximately 35 μJ of energy are transmitted through the stretcher, with a bandwidth ranging from 580-1020 nm. Further details regarding the design and properties of the grism stretcher can be found in reference [71].

The second design goal is that the acousto-optic phase modulator (Dazzler, Fastlite) should be able to compensate the residual dispersion at the end of the system, such to ensure that the pulses are compressed at the location of the different experiments. This was achieved through a careful design of the grism stretcher, realized in collaboration with Fastlite [71]. After the modulator, a pulse energy of approximately 2 μJ is seeded into the amplification stages, at a repetition rate of 10 Hz which is synchronized with the pump laser.

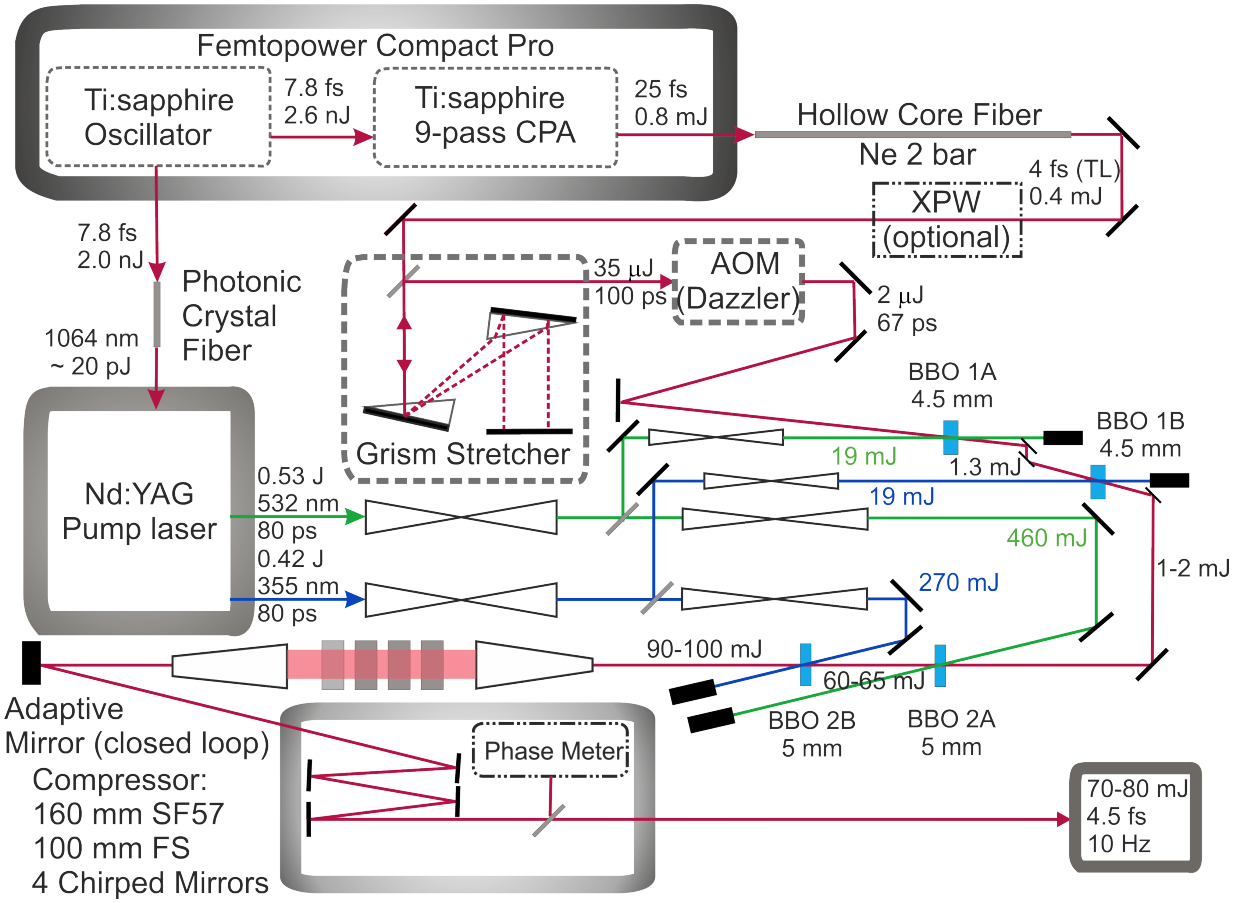

Figure 1.2: Diagram of the LWS-20's experimental setup (see main text for details).

1.2.2 The pump laser

The 'pump' portion of the oscillator is sent into a photonic-crystal fiber which generates approximately 20 pJ of energy after a 10 nm FWHM filter, centered at 1064 nm [73]. This is realized in order to have enough energy to seed the Nd:YAG-based pump laser (see figure 1.4). The pulses are then amplified to 2.5 nJ in a fiber amplifier (Keopsys) from which approximately 1-2 pJ are contained within the pump laser bandwidth .

After the fiber amplifier, the pulses are seeded into a CPA-less Nd:YAG pump laser (EKSPLA) operating at a 10 Hz repetition rate. Given the sensitivity of the OPA process to changes in the intensity or wavefront of the pump laser, the development of a stable and spatially homogeneous pump laser is a crucial step towards the development of the amplifier system. Schematically the pump laser starts with the diode-pumped regenerative amplifier (Regen). In the cavity the pulses make 29 passes, after which a pulse energy of approximately 2 mJ is reached, with an RMS stability below 0.8%. In order to ensure a good quality flat-top beam profile, the pump beam is relay-imaged into each crystal following the Regen until the OPA stages are reached. With a home-made second-harmonic autocorrelator a pulse duration of

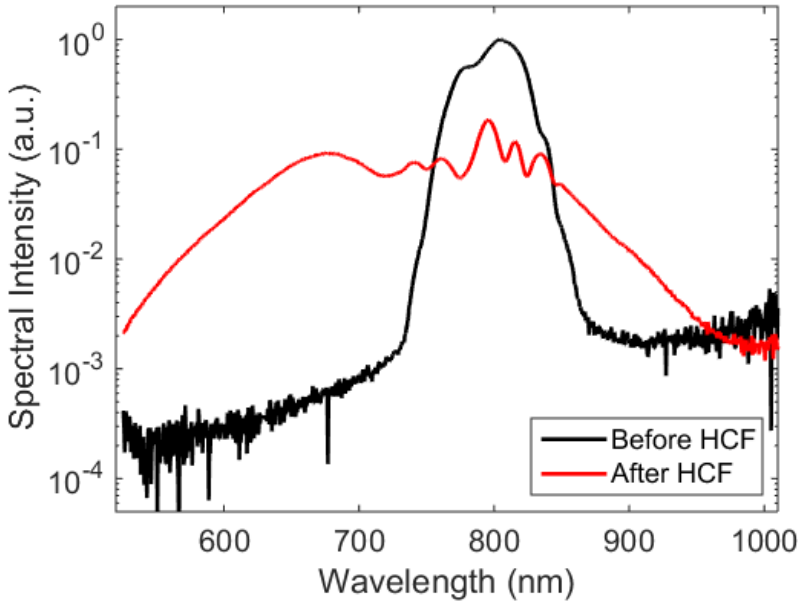

Figure 1.3: Spectrum before and after the HCF. The spectral intensities are normalized to the total input (800 μJ) and output energy (350 μJ).

80 ps is measured.

After the Regen, the pulses are split in order to generate the so-called 2ω and 3ω arm. On both arms an energy of 1 J is reached through a double-pass amplifier and two single-pass amplifiers. The Nd:YAG crystal rods of the double-pass amplifiers are 8 mm in diameter and the single-pass are rods are 12 mm and 18 mm in diameter. All of these crystals are pumped through flash-lamps at a repetition rate of 10 Hz. Given that all amplifiers are operated in saturation, a remarkable pump energy stability of less than 0.4% is reached.

As their name suggest, one of the arms is frequency doubled and the other is frequency tripled. For the second-harmonic, approximately 850 mJ of fundamental energy is sent into a 5 mm long LBO crystal. After separating the fundamental and the second harmonic with dichroic mirror, pulse energies of up to 530 mJ are reached at 532 nm. Similarly for the other arm, the frequency is first doubled and then the sum between the fundamental and second harmonic is generated, both in LBO crystals. After separation of the third harmonic, pulse energies up to 420 mJ are reached at 355 nm.

The amplifier system is divided into four stages: two pre-amplifiers and two high-energy amplifiers. Each amplifier pair is pumped by the second harmonic in the first stage and third harmonic in the second stage, in order to address the different spectral regions. To this purpose, both pump arms are further split such that 5% and 7.5% of the pump energy goes to the 2ω and 3ω pre-amplifiers, respectively. Polarizers are placed before both of these preamplifier stages in order to reduce the energy to 19 mJ. Both arms reach a tenth-order super-Gaussian beam profile on target of 1.8 mm FWHM for the 2ω and 2.3 mm FWHM for the 3ω, reaching

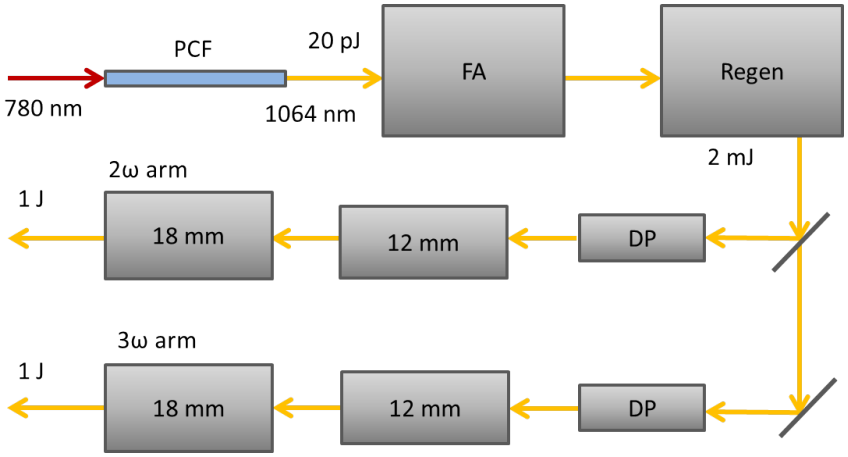

Figure 1.4: Pump laser experimental setup. PCF: photonic-crystal fiber, FA: fiber amplifier, Regen: regenerative amplifier, DP: 8 mm diameter double-pass amplifier, 12 mm: 12 mm diameter single-pass amplifier and 18 mm: 18 mm diameter single-pass amplifier. After the Regen, the beam is split into two arm, which later become the 2ω and 3ω arms.

an estimated intensity of 8.9 GW/cm^2 and 5.7 GW/cm^2 respectively. For the other two stages, approximately 460 mJ of pulse energy at 532 nm and 270 mJ at 355 nm are used. Again With a super-Gaussian beam with a diameter of 9 mm and 10.8 mm FWHM, intensities around 8.6 GW/cm^2 and 3.5 GW/cm^2 are reached respectively.

1.2.3 Amplification stages

As explained in reference [65], changes in the noncollinear angle of 0.05° already change the amplification spectrum significantly and therefore an angle precision better than this is needed. Similar to the one described in that reference, a beam direction and position alignment system was implemented on all four stages. By imaging the seed position and direction on each of the amplification stages it was possible to reproducibly align the seed for an optimum amplification.

As the amplification medium, type-I BBO nonlinear crystals are used. These are mounted in motorized rotation stages which allow the tuning of the phase-matching angle with a precision better than 0.01°. At the 2ω-pumped stages, the crystals have a cut angle of 24° and the non-collinear angle between the pump and the seed is 2.23°. For the 3ω stages, the crystals are cut at 34.5° and a non-collinear angle of 3.40° is used. The crystals of the first two stages are 4.5 mm in length and of the second two 5 mm.

1.3 Amplification results

The evolution of the spectral intensity in the different OPA stages can be seen in figure 1.5. Reference values of the achieved energy and spectrum are included in the figure, and from

day-to-day similar results can be reproduced. In what follows, the expressed values will refer to this measurement in particular unless specified.

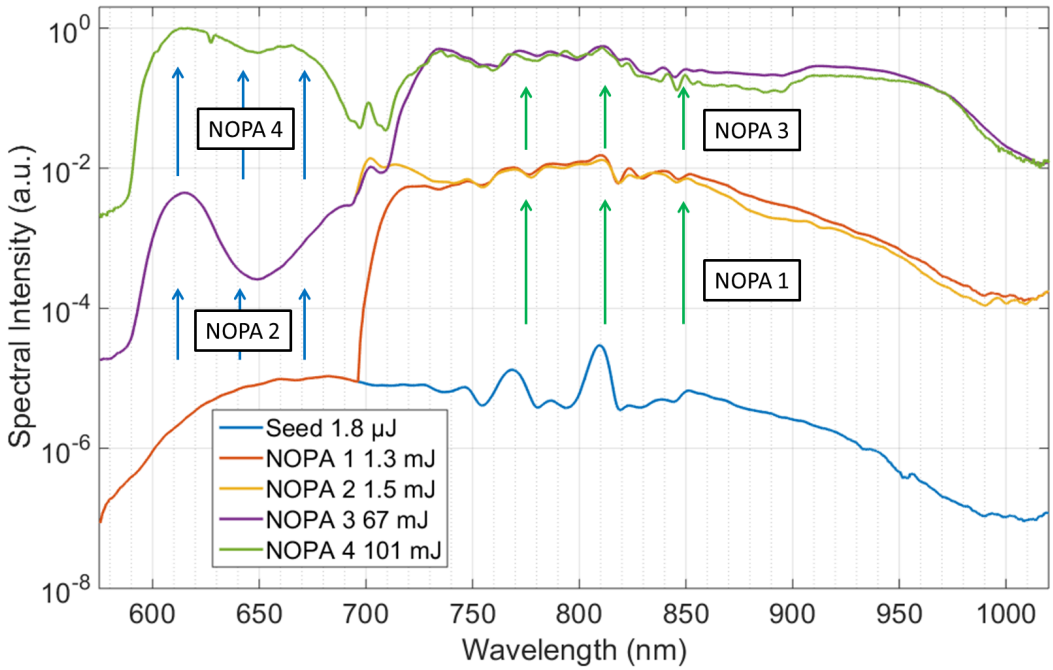

Figure 1.5: Spectrum of seed (blue), and after the first (orange), second (yellow), third (purple) and fourth (green) amplification stage .

As expected from reference [54] an amplification bandwidth between 700-1020 nm is achieved from the 2ω pump and an amplification between 580-700 nm from the 3ω arm. After the first stage the seed energy increases to 1.3 mJ, which translates into an pump-to-seed efficiency of 6.8%, while on the second stage the energy increases by 0.2 mJ in the corresponding bandwidth, resulting in a efficiency of 1.1%. After the second stage the seed is expanded in order to have an homogeneous seed over the whole pump profile at the following amplification stages. As a consequence, approximately 1 mJ of the energy is used as an input for the following stages.

In the third stage, the approximately 1 mJ seed is now amplified to 67 mJ, again covering a bandwidth of only 700-1020 nm, with an amplification efficiency of approximately 15%. Finally, the whole bandwidth is recovered again in the fourth stage, where the seed energy is increased by 34 mJ between 580-700 nm, corresponding to an efficiency of 13%. At the output, pulses with above 100 mJ in energy are regularly reached, with an RMS shot-to-shot stability of approximately 2%.

In the amplified spectra the effects of saturation can be seen. The amplification gain around 1000 nm is higher than at the center, increasing the amplification bandwidth. Additionally, from the second to the fourth stage, the 'hole' at 650 nm is reduced, as well as the modulations

in the region between 750-850 nm in after the first stage. The final spectrum is therefore smoother due to this effect.

Given the difference in size between the 2ω and 3ω pumps, there is a 1 mm region at the border of the amplified beam which only contains components between 580-700 nm, which can generate a focal spot size difference. In any case such a difference is already expected, arising naturally when focusing different wavelengths. This effect can be eliminated by placing a telescope between the third and fourth amplification stages, though it was not attempted during the development of this work. Further details regarding the focus characterization are given in section 3.1.2.

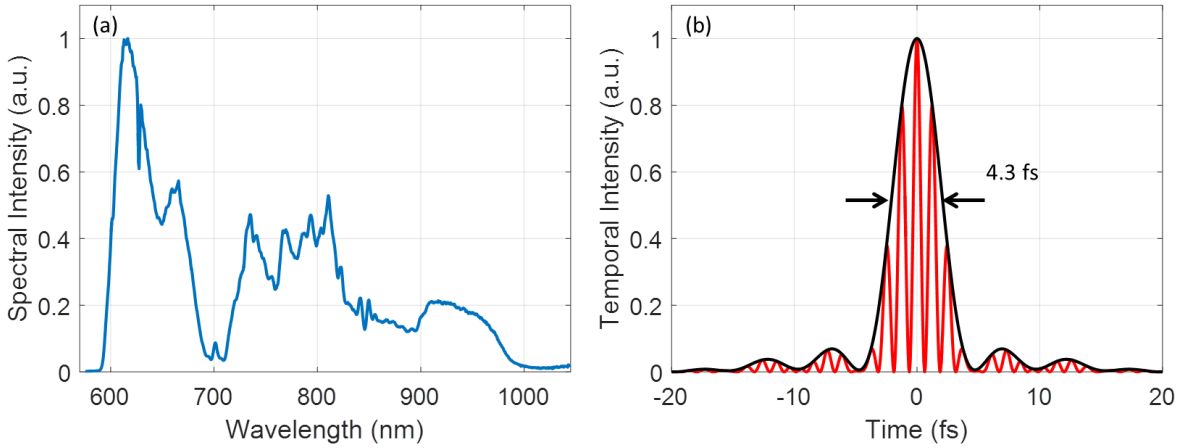

Figure 1.6: (a) Spectral intensity after the fourth NOPA stage, plotted in a linear scale. (b) Temporal intensity calculated from the measured spectral intensity, showing a pulse duration of 4.3 fs.

The amplification spectral regions pumped by the 2ω and 3ω overlap only slightly at 700 nm. This gap and the sharp edge at 580 nm are translated to modulations in the temporal intensity, as it is shown in figure 1.6. By fine tuning the phase-matching parameters and the delay between the different pump pulses and the seed it is possible to tune the amplification region, the amplified spectral shape and total energy (see figure 1.7). As a consequence the pulse Fourier-limited duration changes as well as the energy content in its FWHM (an ideal Gaussian beam has an energy content of 76.1%). Among day-to-day variations and slight alignment changes it is possible to regularly achieve over 100 mJ after the fourth NOPA stage, with a spectrum that supports between 4.0-4.3 fs. However, these values (energy and Fourier limit) degrade when the pulses get compressed with the right Dazzler phase, as discussed in the next section.

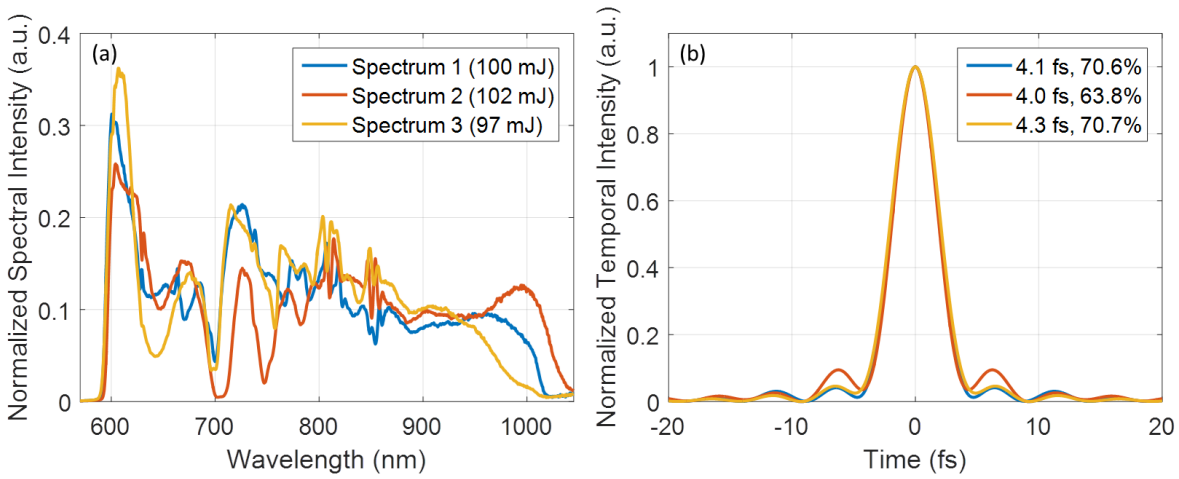

Figure 1.7: (a) Amplified spectra and the overall amplified energy at different alignments. By tuning the phase-matching parameters it is possible to reduce the gap at 700 nm at the cost of amplification energy and overall bandwidth. (b) Fourier-limited temporal intensity profile calculated from the different spectra, with the corresponding pulse duration and energy content in the FWHM. For an ideal Gaussian pulse an energy content of 76.1% is reached.

1.4 Temporal compression and characterization

1.4.1 Compression setup

After amplification, the beam is compressed in two separate steps: bulk compression and chirp mirror compression. The beam reaches a size of approximately 12 mm after the fourth NOPA stage. In order to minimize nonlinear effects in the bulk material, the beam is expanded to a diameter of around 120 mm. The amplified beam is then compressed from approximately 65 ps to 400 fs after propagating through 160 mm of SF57 and 100 mm of fused silica.

The beam size is then reduced to 50 mm in diameter and sent to an adaptive mirror which corrects for wavefront aberrations. The adaptive mirror plane is imaged onto a Shack-Hartmann wave-front sensor which measures these aberrations, which are compensated for in a closed-loop configuration. This setup provides an RMS wavefront error of $40-50$ nm and a Strehl ratio of 0.9, which permits diffraction-limited focusing. Further details about the beam focus are described in section 3.1.2. After the mirror, the beam is sent through a motorized iris which allows to control the beam size for experiments, and then into a vacuum chamber for additional compression. In order to minimize the nonlinearities at the entrance window of the vacuum chamber, the final compression step is realized in the chamber through the reflection on four chirped mirrors which add 75 fs^2 of GDD each [74]. Approximately 80% of the energy after the NOPA stages is transmitted to this position.

1.4.2 Chirp-scan

According to the stretcher design, a residual spectral phase needs to be compensated after the reflection on the last chirped mirror. In order to retrieve this phase, the chirp-scan technique is used [75], which is then corrected with the Dazzler. In order to ensure the pulses are compressed at the target experimental chambers, this technique is applied at those locations by coupling out a small portion of the beam into the characterization setup.

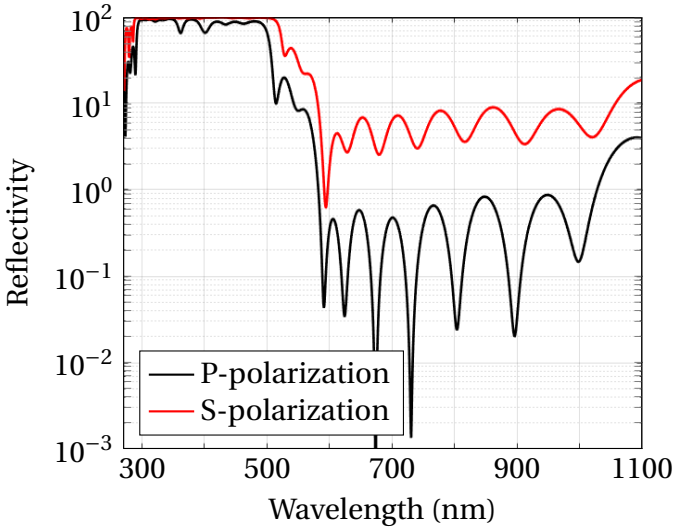

Figure 1.8: Reflectivity curves for p-polarized (black) and s-polarized (red) light on a logarithmic scale, of the separator mirrors used to attenuate the fundamental after the generation of the SH in the chirp-scan setup.

The technique consists of scanning the spectral phase of the NIR pulses while measuring its SH. This method was chosen because of its simplicity: it does not involve IR beam separation before generating the SH, nor sensitive alignment. The SH is generated in a 5 μm BBO crystal, mounted on a 2 mm glass substrate. The beam is then reflected twice by home-made separator mirrors, which attenuate the fundamental spectrum (by two orders of magnitude for the p-polarization) in order to later measure the SH spectrum. Figure 1.8 shows the reflectivity curves for such a separator.

The spectral phase is varied using the Dazzler. The phase-retrieval principle is described in detail in reference [76] for a sinusoidal phase and in reference [75] for the quadratic phase used in this case. The concept can be understood by the fact that for a single frequency ω the SH signal is maximized once the GDD for that frequency $\phi''(\omega)$ is 0. The total GDD is given by $\phi''(\omega) = \phi''_0(\omega) + \phi''_{DAZZ}(\omega)$, where $\phi''_0(\omega)$ is the second derivative of the intrinsic spectral phase to compensate and $\phi''_{DAZZ}(\omega)$ is the GDD introduced by the Dazzler. Then, by scanning $\phi''_{DAZZ}(\omega)$ and knowing at which values the SH signal is maximized, the $\phi''_0(\omega)$ can be retrieved. The total phase $\phi_0(\omega)$ is then known up to two unknown constants (which do not affect the pulse duration).

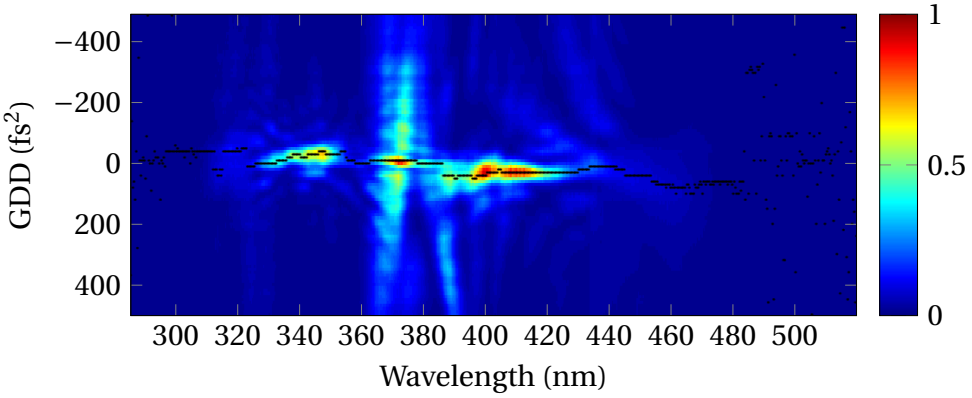

Figure 1.9: SH signal as a function of wavelength and GDD for a chirped pulse. The black curve shows the GDD value at which the signal is maximized for each wavelength.

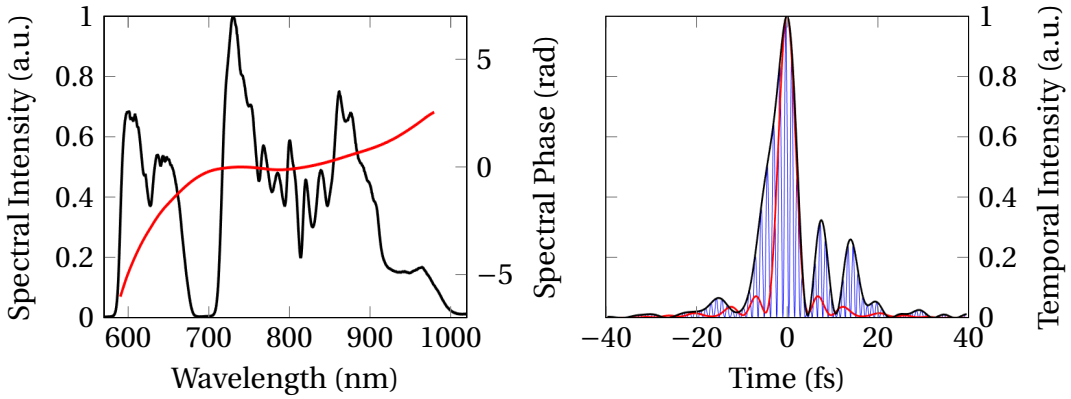

Figure 1.10: a) Spectral intensity (black) and phase (red) retrieved from the scan shown in figure 1.9. b) Instantaneous temporal intensity (blue), intensity envelope (black), and Fourier limit (red) calculated from the measured spectrum and phase. The FWHM pulse duration is 6.8 fs, while the Fourier limit is 4.3 fs.

Figure 1.9 shows such a scan, where the black curve shows the maximum value for each wavelength $\lambda = 2\pi c/\omega$, where c is the speed of light in vacuum. In this case the scan corresponds to initial, uncompressed pulses before the measured phase is fed to the phase modulator. The regions below 295 nm and above 490 nm are discarded because there the SH signal was too low to be measured. In the remaining region, the curve is integrated twice to obtain the phase and then this is used, along with the spectrum measured that day, to calculate the temporal structure through a Fourier transform. Figure 1.10 (a) shows the spectrum (black curve) from that day and the retrieved phase (red curve). The Fourier transform is plotted in figure 1.10 (b), where the black curve shows the temporal intensity envelope, the blue line shows the instantaneous intensity coming from the oscillating electric field and the red curve shows the Fourier limit for that spectrum. The FWHM pulse duration in this case is 6.8 fs, while the Fourier limit is 4.3 fs.

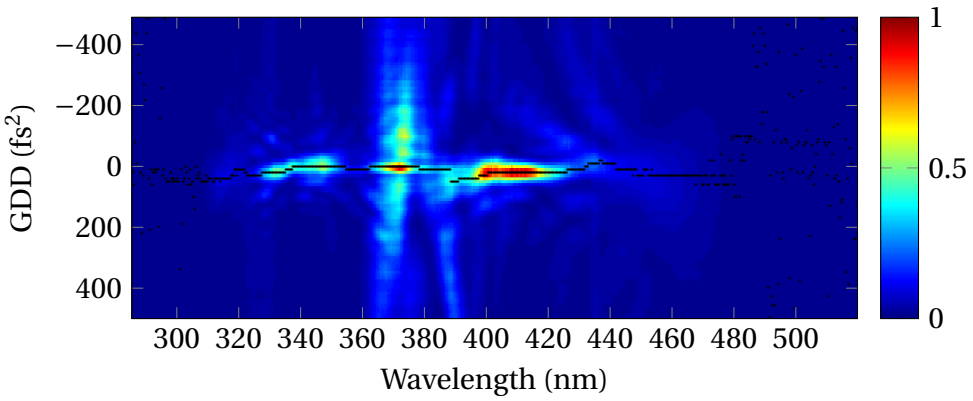

Figure 1.11: SH signal as a function of wavelength and GDD for a compressed pulse. The black curve shows the GDD value at which the signal is maximized for each wavelength.

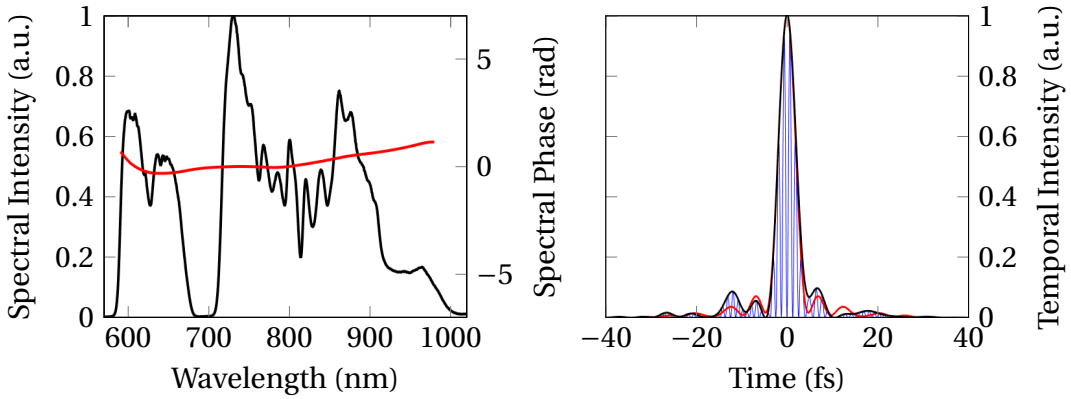

Figure 1.12: a) Spectral intensity (black) and phase (red) retrieved from the scan shown in figure 1.11. b) Instantaneous temporal intensity (blue), intensity envelope (black), and Fourier limit (red) calculated from the measured spectrum and phase. The FWHM pulse duration is 4.4 fs.

The Dazzler is then programmed to compensate for this measured phase and the scan is repeated. Figure 1.11 shows the result after the phase is compensated. Integrating the same region as before to get the phase, and then using it in the Fourier transform yields a pulse duration of 4.4 fs as shown on figure 1.12. If the algorithm is used correctly, from day to day it is possible to achieve pulse durations around 2 – 3% from the Fourier limit. When using the XPW setup, in general less iterations are needed for compression, but the overall amplification energy and bandwidth is slightly reduced.

When using the Dazzler to compensate for the residual spectral phase, its transmission is reduced, affecting the overall amplification. In normal conditions, losses around 10% in the overall energy after the amplification stages are observed. Taking this into account, energies up to 70 mJ are obtained after the chirp mirrors. These results show that sub-two-cycle pulses with up to 16 TW of peak power are available for experiments, making this the most intense

few-cycle source currently available.

1.4.3 Single-shot autocorrelation

The chirp-scan technique works by averaging over multiple shots. Although it confirms the compression to sub-5-fs durations, it provides no information regarding the temporal shot-to-shot stability of the pulses. For this purpose a home-made single-shot second-harmonic autocorrelator (SHAC) was developed. Based on the standard autocorrelation technique, the delay scan is achieved by splitting and then crossing the pulses at an angle θ (see figure 1.13 (a)). By focusing only on the vertical direction with a cylindrical mirror, transversally the pulses will overlap at different delays at the nonlinear medium. This translates the time delay Δt into a transversal position x, and therefore it works in a single shot. The measured signal is the second harmonic of the fundamental frequency, which is generated in a 5 μm thick BBO crystal, supporting the necessary bandwidth. The transversal position is calibrated by delaying one of the two pulses with respect to the other and monitoring the intersection position.

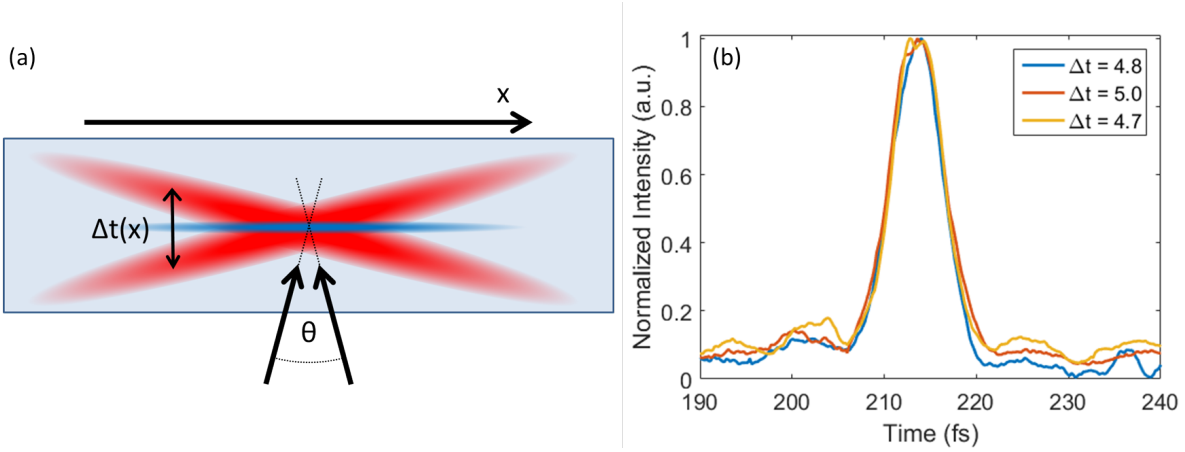

Figure 1.13: (a) Diagram depicting the basic principle of the single-shot SHAC. The noncollinear interaction in the nonlinear crystal generates a time delay scan along the transversal position. (b) Three single shot measurements exhibiting pulse durations between 4.7-5.0 fs FWHM (which assumes a Gaussian pulse shape, which corresponds to a conversion factor of 1.4).

Figure 1.13 (b), shows three different shots showing pulse durations between 4.7-5.0 fs FWHM. The duration is extracted by assuming a Gaussian shape, and therefore dividing the SHAC FWHM duration by 1.4. By measuring over 100 shots a RMS pulse stability of 0.08 fs is obtained, which translated into a $< 2\%$ pulse duration stability. Moreover, this might originate from the measurement technique, leading to even a more stable pulse duration. It is important to emphasize that this method does not uniquely retrieve the spectral phase but serves the purpose of characterizing the pulse duration stability. Additionally, the filters used at the camera have a decreased sensitivity below 350 nm, possibly influencing the measured pulse duration. Nevertheless this measurement confirms the pulses are stable temporally with no big phase fluctuations between the four different NOPA stages.

1.5 Carrier-envelope phase measurement

The last requirement on the driving system for the generation of isolated XUV pulses is the precise control or measurement of the CEP. Considering an optical pulse as a sinusoidal oscillation modulated by an envelope, it is described as $E(t) = E_0(t)\cos(\omega_0 t + \phi)$, where E_0 is the electric field amplitude function, ω_0 the central frequency and ϕ the CEP. Due to the short pulse durations, changes in the CEP play a role in the HHG process [77]. Depending on the CEP value, the HHG process gives rise to a single or double emission of the most energetic XUV photons, as described in the next chapter.

The value of the phase changes when the pulses travel through material, and therefore already at the oscillator the CEP of each emitted pulse has a different value. Changes in, for example, pump laser intensity, temperature, or cavity size affects the phase of the emitted pulses, so without stabilization it can be assumed to vary randomly. For bigger systems, the stabilization of the CEP gets increasingly challenging, and even though it has been recently demonstrated for multi-TW system [78, 79], it was not attempted in the scope of this work.

As an alternative, a homemade stereo above-threshold ionization (ATI) phase meter was developed [80]. This device, by using a small portion of the overall compressed energy, allows to measure the CEP of every shot. The measured phase can later be correlated to the relevant measurement for every recorded shot, a process known as CEP-tagging.

After the last chirped mirror, a few hundred μJ of energy are taken from the beam by the use of a pellicle beam-splitter placed at Brewster-angle. A 5 mm wide silver-coated circular area reflects the pulses into the phase-meter beam path. A pair of chirped mirrors add approximately -200 fs^2 of GDD to pre-compensate for the dispersion of the 2 mm entrance window of the device. A pair of fused silica wedges mounted on a motorized stage allow additional fine-tuning of the dispersion. In the device, the central chamber is filled with xenon gas, which is ionized by the incoming pulses (see figure 1.14 (a)). The free electrons are accelerated by the field of the laser, traveling in the polarization direction into two micro-channel plate (MCP) detectors positioned opposite to each other. The ATI time-of-flight (TOF) electron spectra is measured in a single-shot at each of the detectors (see figure 1.14 (b)).

From the measured spectra, an asymmetry parameter is extracted, defined as

$$A_{x,y} = \frac{S^L_{x,y} - S^R_{x,y}}{S^L_{x,y} + S^R_{x,y}}, \tag{1.10}$$

where x and y are two integration regions (shown shaded in blue and green in figure 1.14 (b)), and $S^L_{x,y}$ and $S^R_{x,y}$ are the integrated signal over those regions for the left and right shot respectively. From these calculated asymmetry parameters, a parametric plot is constructed (for example, see figure 1.15), on which the angle $\tan(\phi) = A_y/A_x$ is proportional to the CEP of the measured shot. The relative error of the asymmetry radius $r = \sqrt{(A_x^2 + A_y^2)}$ gives a measure of the precision of the measured CEP phase [81], which for the example shown here corresponds to approximately 130 mrad. The integration regions are chosen such that this value

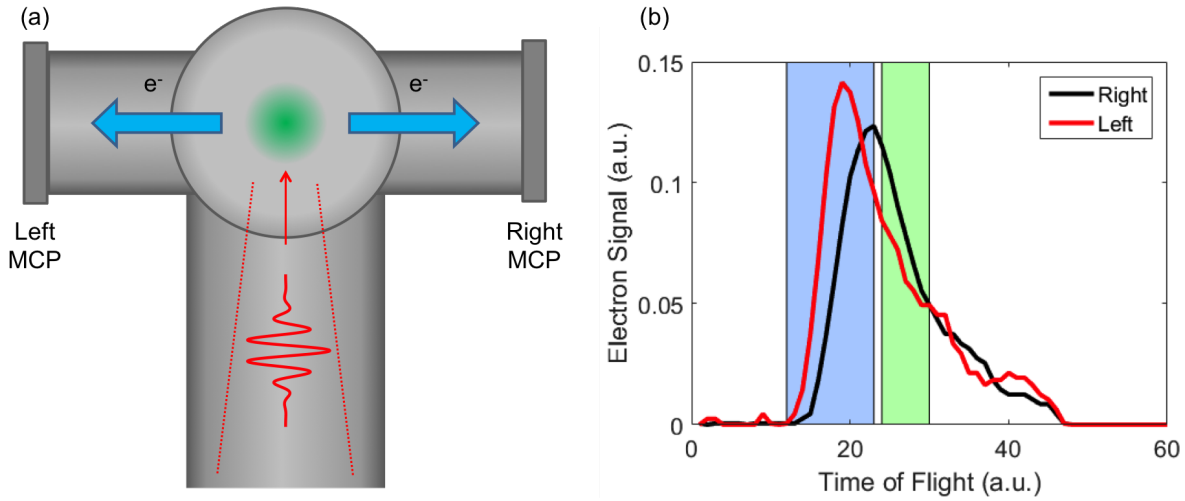

Figure 1.14: (a) Schematic of the phase-meter setup. Xenon gas is ionized in the middle chamber, and the electrons are accelerated to the left and right TOF spectrometers with MCP detectors. (b) Measured electron spectra arising from a single shot. The asymmetry parameters are constructed by integrating the measured signal in the blue- and green-shaded regions.

is minimized. This value is comparable to what can be achieved with standard CEP stabilization setups [82] and much better than what has been demonstrated for > 10 TW systems [78, 79]. Additionally, the average value of the radius of the plot is related to the FWHM pulse duration t_p by $r = 1 - \exp(-9.73/(t_p - 1.61)^2)$ [83]. This can be understood by the fact that the asymmetry is calculated at the higher-energy region of the spectrum, which is more sensitive to the CEP. The shorter the pulses, the stronger the dependence and therefore the higher the asymmetry. For this case, the radius is approximately 0.19, which corresponds to a duration of 8.4 fs. This value is not the pulse duration in the experiment (which is < 5 fs), but the one that reaches the phase-meter.

Although these values can be improved upon, they are already good enough for the purpose of generation of isolated attosecond pulses as described in section 4.2.1. At the moment, the limiting factor arises from the separate compression of both the main beam, and the portion going into the phase-meter. This can be solved by characterizing the residual phase at the phase-meter's target chamber and compensating it with the proper chirped mirror pair.

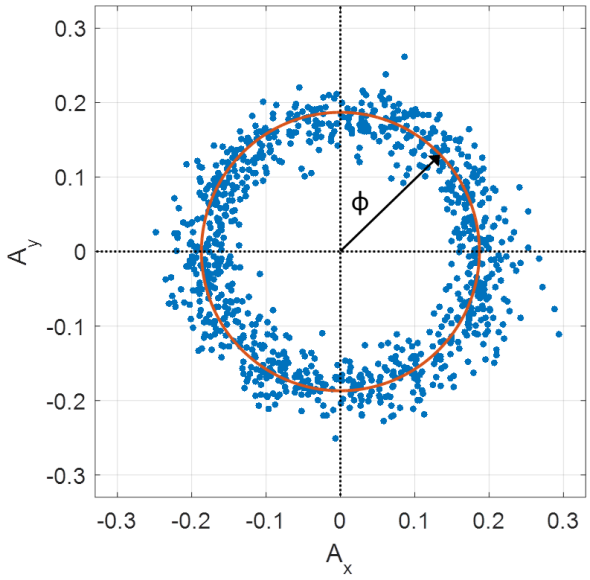

Figure 1.15: Measured asymmetry plot of the LWS-20 from which the angle ϕ is proportional to the CEP. Additionally, the phase RMS error and pulse duration can be extracted from the asymmetry radius (see text), which for this case correspond to to 130 mrad and 8.4 fs respectively.

Chapter summary

- By applying the NOPA technique, pumped by two different wavelengths, a sequential four-stage optical-parametric synthesizer is demonstrated. After amplification, energies above 100 mJ are regularly reached, with a bandwidth supporting sub-5-fs pulses and a shot-to-shot energy stability of approximately 2% RMS.
- For temporal compression, the spectral phase is retrieved through the chirp-scan technique and then compensated with the Dazzler. Near-Fourier-limited ~ 4.5 fs pulses, with energies up to 70 mJ are achieved. This corresponds to a peak power of 16 TW, making the system the most intense few-cycle laser currently available. Through a home-made SHAC, a pulse duration stability of 2% is measured.
- With a home-made CEP meter, the phase can be measured in single shot with a precision of 130 mrad. The setup allows this measurement without significantly affecting the main beam, thus allowing the CEP tagging of relevant processes.
- These characteristics make the system applicable to drive the HHG process with the goal of generating intense attosecond pulses at 100 eV.

Chapter 2

Theoretical description of high-harmonic generation

The main goal of the development of the LWS-20 system is the generation of intense attosecond pulses at the XUV spectral region, which allows the study of time-resolved nonlinear optical effects in a pump/probe configuration. One possible approach to this, is to scale the existing gas HHG setups to the peak-power level provided by the LWS-20, for which several considerations need to be taken into account. In this chapter, the procedure to achieve this goal is discussed.

First the semi-classical model for HHG is introduced, which despite its simplicity allows to describe the main properties of the XUV generation process. When taking this model to a real-life situation the effects of propagation through the generation gas need to be considered and are described in the second section of this chapter, along the energy-scaling scheme. Finally, the effects of varying degrees of ionization in the generation process are described in the last section.

2.1 Single-atom response

For high enough intensities, the nonlinear optic's perturbative model fails to describe the observed constant efficiency high-order harmonics coming from nobel gases [6, 7]. Even though the absolute intensity of these harmonics is quite low, it stays relatively constant for several harmonic orders (named the *plateau* region) and then quickly drops (named the *cutoff* region).

To explain this, first a semi-classical model was developed [84, 85], which can describe most of the important features of the process. Short after, a quantum mechanical model allowed to describe these features and others under the strong-field approximation [86]. For our purpose the semi-classical model describes the necessary properties to understand the scaling-scheme and therefore the quantum model will not be discussed.

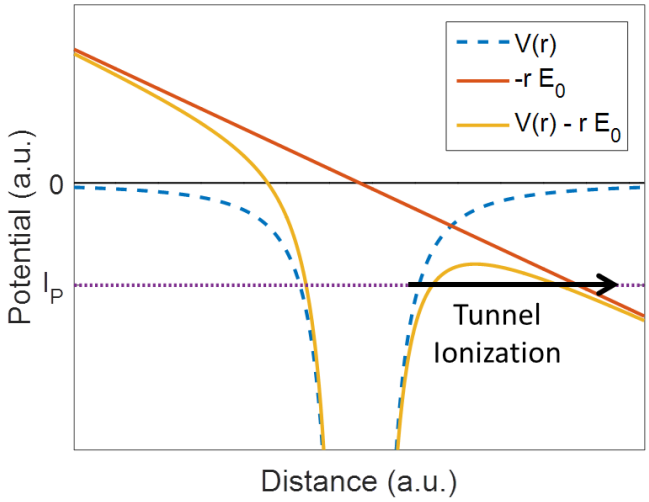

Figure 2.1: The potential arising from the driving electric field (red curve) tilts the Coulomb potential (blue dashed curve) forming a barrier potential (yellow curve). Depending on the driving field and ionization energy the electron is allowed to tunnel through this barrier (depicted by black arrow).

2.1.1 The 3-step model and amplitude gating

The perturbative model fails to describe the HHG process because when the laser electric field reaches a comparable value to the inter-atomic electric field, the valence electrons no longer remain bound to the parent ion, but are allowed to tunnel through its potential (see figure 2.1). The simplicity of the semi-classical model comes from assuming that once the electron is free, it follows classical trajectories driven by the oscillating laser-field. Depending on the moment of ionization, the electrons follow different trajectories and can return to the position of the parent ion and recombine. If this happens the acquired kinetic energy, plus the ionization energy are converted into a single photon. Due to its three steps: ionization, acceleration and recombination, this model is colloquially termed the *three-step model*. Both the ionization and recombination rates are not accounted for with this model.

We start with a sinusoidal electric field of the form $E(t) = E_0 \cos(\omega_0 t)$, where E_0 is the peak electric field and ω_0 is the driving laser's central angular frequency. Assuming the electron is ionized at time t_0 and position $x = 0$ with no initial velocity, the velocity as a function of time is given by

$$v(t) = -\frac{eE_0}{m_e\omega_0}\big[\sin(\omega_0 t) - \sin(w_0 t_0)\big], \tag{2.1}$$

where e is the electron charge and m_e the electron mass. Depending on the ionization time some electrons will drift off and others will cross the $x = 0$ at a later instant. The returning electrons have a non-zero probability of recombining with the parent ion. Assuming the elec-

tron return and recombines with its parent ion at $t = t_1$, the energy of the emitted photon is given by

$$\hbar\omega_{hhg} = I_p + \frac{1}{2} m_e v^2(t_1) = I_p + 2U_p\big[\sin(\omega_0 t_1) - \sin(w_0 t_0)\big]^2, \tag{2.2}$$

where I_p is the ionization potential and

$$U_p = \frac{(eE_0)^2}{4m_e\omega_0^2}, \tag{2.3}$$

is the ponderomotive potential. In order to find the instant of return t_1 as a function of t_0, equation 2.1 is integrated to find the electron position as a function of time, giving

$$x(t) = \frac{eE_0}{m_e\omega_0^2}\Big\{\big[\cos(\omega_0 t) - \cos(\omega_0 t_0)\big] + \omega_0 \sin(\omega_0 t_0)(t - t_0)\Big\}. \tag{2.4}$$

The return time is then implicitly given by $x(t_1) = 0$. Using this condition, equation 2.2 is numerically solved in order to find the return energy of the electron as a function of ionization time (see figure 2.2). The time scale is relative to the driving electric field, where $t_0 = 0$ corresponds to the peak of the driving electric field.

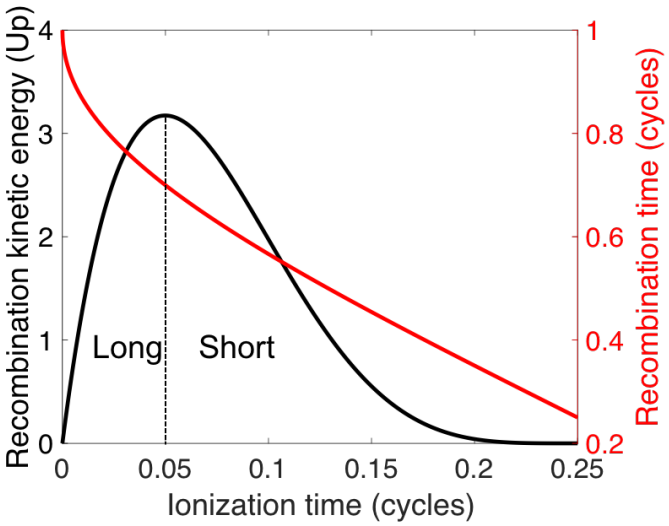

Figure 2.2: Electron recombination time and kinetic energy as a function of ionization time. Electrons released after 0.25 cycles do not return to $x(t) = 0$. For a given recombination energy, there are two different ionization times leading to that energy, which corresponds to the short and long trajectories. This is true for all energies except the maximum, given by $K_{\max} = 3.17\ U_p$. $t_0 = 0$ corresponds to the peak of the driving electric field.

From this model several features of the HHG process can be retrieved. First, the kinetic energy curve reaches a peak value of $K_{\max} = 3.17U_p$, which leads to a maximum photon energy of

$$\hbar\omega_{\text{cutoff}} = I_p + 3.17\ U_p. \tag{2.5}$$

This relation can also be expressed as

$$\hbar\omega_{\text{cutoff}} = I_p + 2.96 \times 10^{-13} I_0 \lambda_0^2, \tag{2.6}$$

where I_0 is the peak instantaneous intensity of the laser in W/cm^2, λ_0^2 its central wavelength in μm, and the ionization potential I_p in eV.

This maximum corresponds approximately to the previously mentioned cutoff energy observed in experiments. For example, for neon as a the generation gas (I_p = 21.6 eV) and a intensity of 4.8×10^{14} W/cm^2 a maximum photon energy of 100 eV is reached. For a few-cycle driving pulse this theoretical value is slightly different, and moreover, it can be modified due to propagation effects on the laser and phase-matching. This topic is additionally discussed in chapter 4.

Additionally, from figure 2.2 one can see that for a given acquired kinetic energy, there are two different ionization times leading to that energy (except, of course, for the cutoff energy). Given that the recombination time decreases monotonically with ionization time, these two electrons will experience different *flight times* and thus acquire a different phase. These two paths are named *short trajectories* for electrons ionized after the energy peak and *long trajectories* for the ones ionized before the energy peak.

For long pulses, ie., pulses where the peak electric field does not vary significantly from one half-cycle to the next one, the described effects will be repeated after each half-cycle, generating an XUV pulse train. Due to spectral interference between the generated pulses, the XUV spectra that is finally measured results in clear odd-harmonics [7]. However, for decreasing pulse durations electron acquiring the same kinetic energy will spend different times in the continuum, thus acquiring different phases from half-cycle to half-cycle. Spectrally this means the harmonic line energies will not be equidistant anymore [87]. Additionally when changing the CEP of the driving pulse, the harmonic line position changes as well.

For the limiting case of pulses below two cycles in duration, the higher energy photons are generated once during pulse propagation, for the right CEP values [77, 88]. Spectrally, this is translated to the disappearance of the interference pattern (forming the so-called *continuum*), which is an easily measurable indicator of this effect[1].

These high-energy spectral components can be separated from the others through proper spectral filtering, for example with thin metallic filters and/or broadband XUV mirrors [90], leading to an isolated pulse. Given that ionization occurs only at the peak of the electric field, it is expected that these pulses are much shorter than a half-cycle, entering the attosecond domain.

Using the reported continuum of approximately 10 eV from reference [77], a Fourier limit of 180 as FWHM for a Gaussian pulse is obtained. However, given the different travel times of the electrons, an intrinsic chirp is embedded in the generated pulse , which is positive for the

[1] Though it is a necessary condition, it is not sufficient as shown for example in reference [89].

short trajectories and negative for the long trajectories [91]. By careful dispersion management, pulses as short as 67 as have been demonstrated [92].

2.1.2 Intensity limit

Equation 2.5 shows a linear dependence of the cutoff photon energy with I_p and U_p, the latter depending linearly on the laser intensity and is proportional to λ_L^2. Changing the generation gas permits some tunability on the generated photon energies, with the cost of reduced efficiency as the atomic number decreases [35]. Additionally propagation effects play a role on the measured cutoff, and will be discussed in the next section. The approach of increasing the cutoff energy by driving the process with longer wavelengths is a topic of active research but it is outside the scope of this thesis[2].

The other alternative to increase the generated photon energies is to drive the process with higher intensities. Ultimately this approach is limited by ground-state depletion; as the ground-state population decreases the number of emitters decreases accordingly. One can argue that the process can continue by generating harmonics from ions instead of neutrals [94], but free-electrons become a limiting factor as described in the next section.

Beside the obvious effects of ground-state depletion, a more subtle effect dominates at slightly lower intensities, as discussed in reference [95]. In this work the single atom response is studied when transitioning between tunnel ionization and barrier-suppression ionization (BSI) for increasing intensities. The latter occurs when the driving field is strong enough to lower the potential barrier to below the energy level of the ground state, allowing the electron to directly leave the parent atom (see figure 2.3). By equating the ionization potential I_p to the peak of the tilted coulomb potential, the BSI intensity is given by

$$I_{\mathrm{BSI}} = \frac{c\epsilon_0^3\pi^2}{2Z^2e^6} I_p^4, \tag{2.7}$$

where c is the speed of light, ϵ_0 the permitivity of free space, Z the charge-state of the ion and e the electron charge. In terms of the ionization potential in eV, the I_{BSI} intensity in W/cm^{2}can be expressed as

$$I_{\mathrm{BSI}} = \frac{4.00}{Z^2} \times 10^9 I_p^4. \tag{2.8}$$

Table 2.1 shows the BSI intensities for the main noble gases used for HHG.

In this regime, the effective harmonic yield not only saturates with increasing intensity (as expected from depletion) but decreases. This is attributed to a reduction of the emission cross-section when the ground state population is decreased in addition to the increased spreading of the traveling electron wave-packet at higher intensities. This effects start dominating at $I_0 \approx 3 \times I_{BSI}$, so at this intensity the HHG process becomes less efficient. Another important effect is that the assumption of zero initial velocity for the ionized electron stops being valid at this intensity, which can be shown to reduce the maximum attainable energy by the electrons.

[2] More information can be found in reference [93] and references therein.

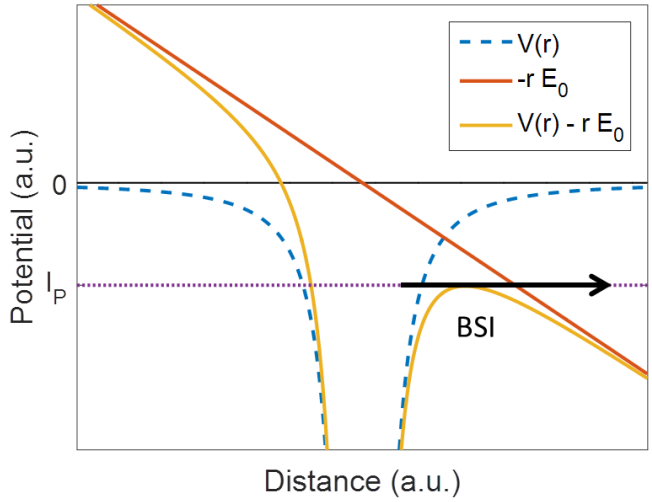

Figure 2.3: The potential arising from the driving electric field (red curve) tilts the Coulomb potential (blue dashed curve) such that the potential barrier (yellow curve) is lower than the ionization energy of the electron (purple dotted curve), allowing the electron to be directly ionized (depicted by black arrow).

Even though this model serves to understand the main properties and limitations of gas HHG, the propagation effects of both the driving laser and generated XUV beam need to taken into account for a complete understanding of the process.

2.2 Macroscopic response

2.2.1 Harmonic yield optimization model

The macroscopic harmonic emission, depends not only on the response of individual atoms to the driving electric field, but also on how these atoms collectively respond and affect the driving and emitted radiation. Three main macroscopical effects take place during the HHG processes: laser propagation effects, phase-matching and absorption.

Even though for this work the effects of laser propagation are of extreme importance, they were not taken into account in the initial scaling model. To correctly describe HHG in macroscopic media where the laser field changes during propagation, intensive calculations are needed, for which detailed knowledge of the generation conditions is advantageous. This was done after the main experimental results were achieved, and are described in detail in section 4.4.4.

For an unaltered laser propagation, the generation processes is said to be phase-matched when the different atoms emit the radiation in phase, leading to a constructive interference at the detector. The more atoms in the ensemble, the stronger the radiation. However, this

effects competes with absorption due to the nonzero ionization cross-section of gases in this XUV frequency range. A very simple model developed in reference [96] allows to describe the interplay between these two effects. For a single harmonic frequency ω_q of q times the fundamental frequency $\omega_0 = ck_0$, the coherence and absorption lengths are defined respectively as

$$L_{\text{coh}} = \frac{\pi}{\Delta k_q}, \tag{2.9}$$

and

$$L_{\text{abs}} = \frac{1}{\sigma_q \rho}, \tag{2.10}$$

where $\Delta k_q = k_q - qk_0$ is phase mismatch between the driving laser and the generated harmonic, σ_q is the ionization cross section at the frequency ω_q, and ρ is the gas number density. Assuming a 1-D propagation, with both the dipole response A_q at frequency ω_q and gas density independent of propagation distance, the number of emitted photons at frequency ω_q as a function of the generation medium length L_{med} is proportional to

$$N_q(L_{\text{med}}) \propto A_q^2 \rho^2 \frac{4L_{\text{abs}}^2}{1+4\pi(L_{\text{abs}}^2/L_{\text{coh}}^2)} \left[1 + \exp\left(-\frac{L_{\text{med}}}{L_{\text{abs}}}\right) - 2\cos\left(\frac{\pi L_{\text{med}}}{L_{\text{coh}}}\right)\exp\left(-\frac{L_{\text{med}}}{2L_{\text{abs}}}\right)\right]. \tag{2.11}$$

Figure 2.4 shows the normalized photon yield as a function of medium length, for different coherence and absorption lengths. As expected, for perfect phase-matching ($L_{\text{coh}} \to \infty$) and no absorption ($L_{\text{abs}} \to \infty$) the yield grows exponentially (dotted line). However, in the presence of absorption, even in the case of perfect phase-matching the yield reaches an asymptotic maximum (to which the curves are normalized). For decreasing coherence lengths, the maximum achievable yield decreases.

Defining an optimized yield as half of the perfect phase-matched yield, one can conclude that a medium length longer than $3 \times L_{\text{abs}}$ and a coherence length longer than $5 \times L_{\text{abs}}$ are needed. For example, at 100 eV neon has a cross-section of 3.92 Mb [97], which at 5 mbar would lead to an absorption length of $L_{\text{abs}} = 2.1$ cm. It is worth noticing that these conditions have to be satisfied separately for different harmonics in order to have broadband emission (the absorption length at 70 eV and 125 eV are $L_{\text{abs}} = 1.3$ cm and $L_{\text{abs}} = 3.1$ cm respectively).

Experimentally, the first condition is trivially achieved by simply ensuring the medium is long enough. However the second condition involves several experimental parameters.

2.2.2 Phase-matching and energy scaling

The phase mismatch can be separated into four contributions: neutral gas dispersion, free-electron dispersion, geometric (Gouy) phase and dipole phase [98, 99], which can be respectively written as

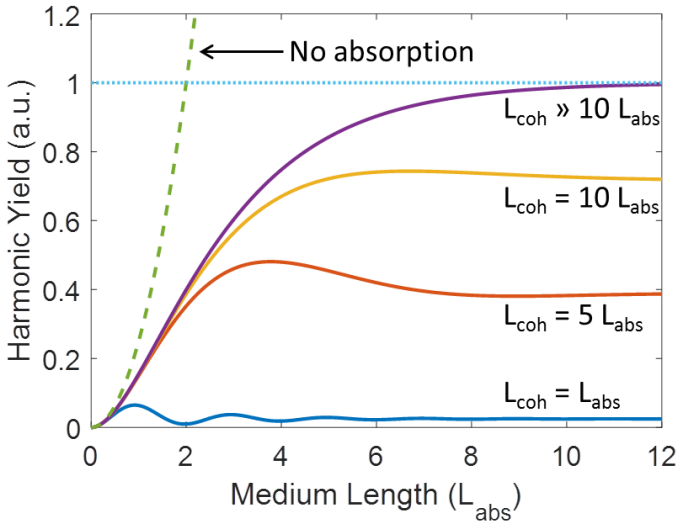

Figure 2.4: Normalized yield as a function of medium length. For $L_{\text{coh}} \to \infty$ and $L_{\text{abs}} \to \infty$ the yield increases exponentially with medium length (dotted line). For $L_{\text{coh}} \to \infty$ but finite absorption length, the yield asymptotically increases to a maximum and for decreasing L_{coh} the maximum decreases. An optimized yield is reached for $L_{\text{med}} > 3 \times L_{\text{abs}}$ and $L_{\text{coh}} > 5 \times L_{\text{abs}}$. (This plot has been adapted from [96]).

$$\Delta k_q = \Delta k_n + \Delta k_e + \Delta k_g + \Delta k_d. \tag{2.12}$$

The first two terms have opposite sign and are directly proportional to the gas pressure. The second term however, additionally depends on the laser pulse duration and intensity. As the driving laser interacts with the gas, the ionization process takes place, increasing the number of free electrons in time.

The third and fourth term depend on the focusing geometry of the driving laser and are independent on the gas pressure. Δk_g arises from the phase acquired by the laser when it goes through the focus and is opposite in sign as the neutral gas dispersion. The last term, Δk_d, depends on the phase acquired by the traveling electron, which depends on the intensity gradient [86, 100]. It has a higher value for the long trajectories in comparison to the short trajectories and it acquires a negative value for $z < 0$ and a positive value for $z > 0$ ($z = 0$ being the focus position). For this reason, when scanning the generation medium longitudinal position with respect to the focus position an optimum in the yield is observed when the focus is located strictly before or after the medium [100].

It is well known that for correct phase-matching the ionization level should be kept down to only a few percent [96, 98, 101, 102]. This is because the phase acquired by the free-electron dispersion needs to be compensated by the other terms, which is translated into a limit in the driving laser intensity. By integrating the ionization rate given by the cycle averaged ADK model [103], the ionization level at the peak of the pulse can be found. Figure 2.5 shows the ionization probability at the peak of a 5 fs FWHM Gaussian pulse, as a function of the peak in-

tensity, for different noble gases. During this evolution there will be a time window for which the phase-matching condition is achieved transiently, the more intense the pulse, the earlier this condition is achieved.

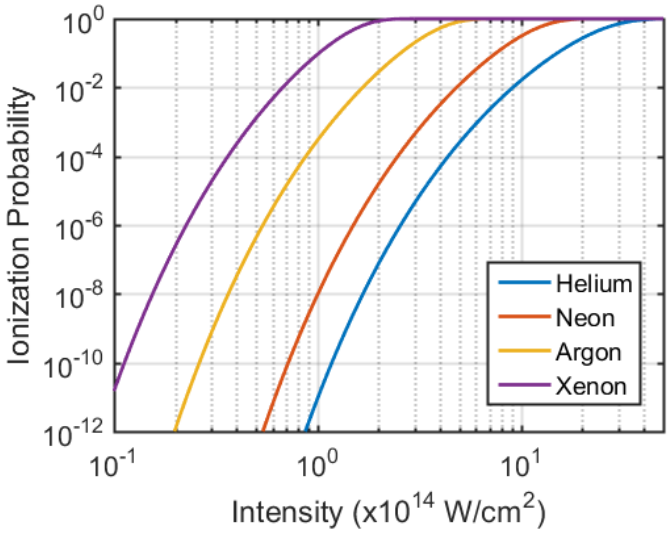

Figure 2.5: Ionization probability at the peak of a 5 fs FWHM Gaussian pulse, as a function of the peak intensity, for helium (blue curve), neon (orange curve), argon (yellow curve) and xenon (purple curve).

Lighter noble gases allow to generate harmonics with a higher cutoff [7]. From equation 2.5, it can be seen that this is partly due to the increased ionization potential. However figure 2.5 shows that for a constant intensity, lighter gases have a lower ionization probability. This means the ionization level necessary for phase-matching occurs at higher intensities for lighter gases. For neon as the generation gas, a peak intensity of approximately 6×10^{14} W/cm^2 generates a 3% ionization at the peak of a 5 fs pulse. Table 2.1 provides additional examples for the other gases, which all require intensities below the BSI intensity in order to keep the ionization level low.

Experimentally the phase-matching parameters need to be scanned in order to optimize the XUV yield. The neutral gas dispersion is controlled by simply changing the gas pressure in the generation medium. The free-electron density is controlled through the driving laser energy, which generally is controlled through an iris before the focusing optic. However, by changing the beam size the focusing geometry is also altered, affecting the geometric and dipole phase. For this reason, in order to gain an extra degree of freedom, independent control of the beam size and energy is desirable, as reported in reference [99]. In that work it is shown that up to a factor of two in the yield of a single harmonic can be gained by separately scanning the laser energy and beam size. The focusing geometry phases are controlled by changing the position of the generation medium with respect to the focus. In chapter 3 the implementation of these scans in the HHG setup is described.

Loose-focusing energy scaling

In order to drive the harmonic generation process efficiently with high-energy pulses (such as the ones provided by the LWS-20), the focus size should be increased such that the intensity is kept at the desired level. Larger focal spots are reached by increasing the focal length of the focusing optic. If the generation conditions are kept constant, the XUV generation spot is larger and thus increasing the overall yield. This scaling procedure is known as the loose-focusing geometry energy-scaling scheme and is described in detail in reference [98].

When increasing the focal length, the Rayleigh length z_R is also increased. For a harmonic order q, the phase mismatch arising from the geometrical phase is given by $\Delta k_g = q/(z_R + z^2/z_R)$, so increasing z_R decreases this contribution. In order to keep the phase-matching condition, the pressure needs to be reduced accordingly and to compensate for the reduced number of emitters, the medium length needs to be extended.

Even though the scaling principle is straightforward, the determination of a general optimum generation condition is challenging. The main results achieved so far at 100 eV photon energy and beyond have been realized under very different conditions [77, 88, 99, 102, 104–107] and moreover, the generation parameters are not always reported or carefully characterized. This is particularly true for the driving intensity, which is reported (or estimated) to range from 4 - 45×10^{14} W/cm^2.

The work realized by Takahashi et al. [105] is usually referenced as to what is achievable with neon. In their work, they report photon energies up to 100 eV, with a total XUV pulse energy of ~ 400 nJ. The driving intensity reaches a value in the order of 7×10^{14} W/cm^2, by using the loose-focusing approach with a 50 mJ, 30 fs laser. In this work, they already mention a discrepancy between the generation intensity and the calculated intensity through the cutoff ($\sim 4 \times 10^{14}$ W/cm^2), which is attributed to laser propagation dynamics. Results similar to this one have been later reproduced by using the loose-focusing energy scaling scheme[99], and thus were achieved at a similar intensity. For neon, this intensity is below its BSI intensity.

For the generation of isolated attosecond pulses, shorter driving lasers are needed. Initial work realized with few-cycle driving lasers was first able to demonstrate the disappearance of the modulations at the cutoff region around 100 eV [77, 104] and later confirm the isolation of pulses with attosecond durations [9]. As an example, in the work of Schnürer et al. an average intensity of 5×10^{14} W/cm^2 is used, with a 7 fs, 0.7 mJ driving laser. This value is calculated by averaging over an effective area of πw_0^2, where w_0 is the $1/e^2$ radius, which is measured to be 60 μm. For correct comparison, we estimate that the peak intensity is 2.4 times the $1/e^2$ average, leading to 1.2×10^{15} W/cm^2. In figure 2.5 it can be seen that at these intensities the low ionization condition is not fulfilled at the peak of the pulse. For comparison, this intensity is above the BSI intensity of neon.

In order to scale the generation conditions from references [99, 105] to the parameters provided by the LWS-20 (50 mm in diameter, flat-top beam with approximately 50 mJ on target and 4.5 fs FWHM in duration), a focal length of ~ 30 m is needed, with which several tens of nJ are expected to be reached. Besides the technical challenge of using such a long focal length mirror, an additional difference can be seen between this generation conditions and the one

reported in [104]. The cutoff energy achieved in the work of Takahashi reaches approximately 100 eV, while in reference [104] it goes up to 150 eV. Moreover, despite the fact that modulations are expected at the cutoff region for pulses longer than 5 fs [87], this was not the case for certain CEPs. This topic is discussed in more detail in the next section.

2.3 Phase-matching at above-BSI intensities

2.3.1 Ionization gating

The concept of harmonic generation in highly ionized media was initially studied with the goal of stopping the generation process during the pulse propagation. By driving the generation process at higher intensities, Bouhal et al showed that the fast increase in free-electron density was used to reduce the duration of the 19th harmonic by half of the expected value [108]. Later, through the same principle, shorter pulses were achieved as reported in references [109, 110], and finally isolated pulses with attosecond duration were demonstrated from a gas-filled hollow-core fiber [111] and a gas jet [102].

The underlying mechanism relies on the increase of the phase-mismatch with increasing free-electron density. If at a certain moment the phase-matching condition stops being fulfilled during the pulse propagation, all the harmonics that are generated later will no longer be phase-matched and therefore will not contribute to the overall measured XUV radiation (see figure 2.6). This process is known as ionization gating.

When the intensity is tuned such that the loss of phase-matching occurs before the main peak, the high energy photons are phase-matched for only a single half-cycle, which spectrally corresponds to the continuum region. With proper spectral filtering, it is possible to isolate a single pulse with durations in the attosecond regime. As seen in figure 2.6, the bandwidth of the continuum region is broader in comparison to the low ionization regime. This argument is still valid for pulses much longer than two cycles if the intensity is increased accordingly (see figure 2.7). However, achieving this experimentally becomes very challenging. On one hand the generation process occurs at the leading edge of the pulse, where the spatio-temporal pulse properties are not easily accessible and on the other hand the generation process becomes much more sensitive to fluctuations in phase and intensity.

A remarkable result from references [102, 109, 110] is that this process already occurs at intensities slightly higher than 5×10^{14} W/cm^2 for pulses of 8 fs duration. These conditions are similar for the ones reported in [77, 104], where a 7 fs pulses was used. This might explain why a continuous spectrum was observed at the cutoff energies in these cases.

Even though, in this regime the conditions necessary for the generation of isolated attosecond pulses are relaxed, the overall efficiency is comparable to the lower intensity case. As in the case of amplitude gating, it is still necessary to filter out the lower order harmonics for the isolation of the attosecond pulse. Moreover, the generation process is phase-matched only in the leading edge of the pulse which effectively discards the harmonics generated in main portion of the pulse.

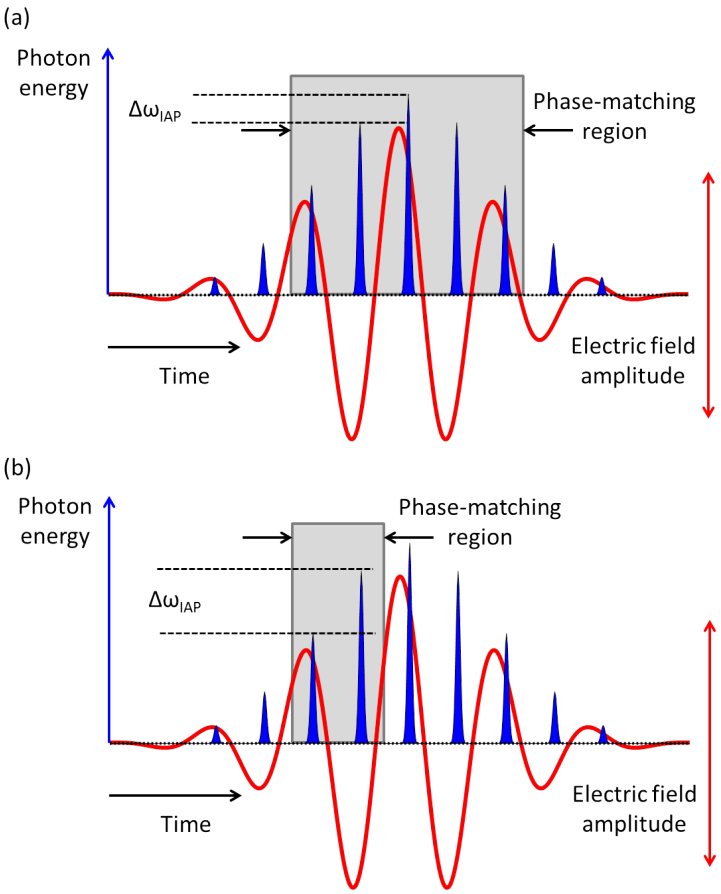

Figure 2.6: Phase-matching process schematic, where the red line is the driving pulse and the blue lines are the harmonics emitted through the single-atom response. (a) Phase-matching process for a low intensity pulse, where the phase-matching window contains several generated harmonics. These harmonics thus interfere after propagation, with only a small bandwidth generated only once near the peak of the driving field ($\Delta\omega_{IAP}$). (b) Phase-matching schematic for a high intensity pulse, where the free-electrons reduce the phase-matching window. Only the harmonics at the leading edge of the pulse are phase-matched, allowing the generation of isolated attosecond pulses with a broader bandwidth ($\Delta\omega_{IAP}$).

In practice the process becomes even more complex when considering that the intensity also has a transversal dependence. For a transversal plane of the generation medium, optimum phase matching occurs earlier in the laser pulse near the center of the focus and is delayed on the outside. Additionally, the central part of the beam will experience stronger phase modulations given the higher ionization degree, so the driving beam's transversal shape will be modified during propagation. A further theoretical description of these processes are beyond the scope of this work. Additional comments on this topic in relation to the experimental results are presented along the simulation in section 4.4.4.

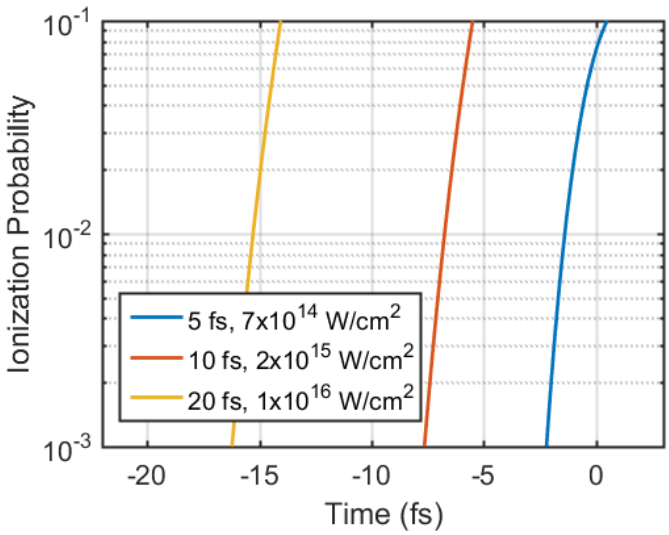

Figure 2.7: Temporal evolution of the ionization for three different pulse durations and intensities. For these values a similar ionization slope is achieved for the ideal probability $p \approx 0.01$. This shows that ionization gating can be achieved for longer pulses if the intensity is increased accordingly.

2.3.2 Sub-cycle ionization gating

An extreme case of ionization gating occurs when using sub-two-cycle pulses along intensities much above the BSI intensity. Under these conditions the generation of isolated pulses with extremely high bandwidths has been demonstrated [107, 112], with the additional requirement of low pressures and spatial filtering of the generated XUV. In this case, similar to what is reported in reference [95], the effect is explained through the single atom response [112, 113], where a rapid increase in ionization depletes the neutral atom population within a single-cycle, allowing only a single emission of XUV radiation. This process has been observed for few-cycle pulses and only for a certain CEP range.

The intensities at which this process takes place are reported to be ranging between 2.3-4.5×10^{15} W/cm^2 for xenon, krypton, argon and neon for a 5 fs pulse. From figure 2.5 it is clear that at these intensities the gases are depleted completely at the peak of the pulse (krypton is not included in the figure but its curve should be between xenon and argon). As in normal ionization gating, the efficiency is expected to be comparable (or worse) to the one at the below-BSI regime, and given the additional need of spatial filtering and lower pressures the overall energy on target is smaller. However, the spectral filtering necessary for amplitude and ionization gating greatly reduces the XUV energy available for experiments. The possibility of directly generating an isolated attosecond pulse without spectral filtering might compensate the reduced efficiency of the generation process and can find applications when extreme bandwidth are required. Experimental results regarding generation at this regime with the LWS-20 are described in chapter 4.

Gas	I_p (ev)	I_{BSI} (W/cm^2)	$I_{3\%}$ (W/cm^2)	P_{BSI}
Xe	12.1	8.7×10^{13}	8.1×10^{13}	4.5%
Ar	15.8	2.5×10^{14}	2.0×10^{14}	9.0%
Ne	21.6	8.6×10^{14}	5.9×10^{14}	18%
He	24.6	1.5×10^{15}	1.1×10^{15}	9.9%

Table 2.1: Relevant ionization parameters for the four main gases used for HHG. The columns show the ionization potential, BSI intensity, and intensity required to ionize up to 3%, and ionization probability at the peak of a 5 fs pulse with a peak intensity equal to the BSI intensity.

In summary, we can identify three different generation regimes which depend on the driving laser intensity: below-BSI intensity, above-BSI intensity, and depletion intensity regime. The transition intensity is not an exact value and depends on the other phase-matching conditions in addition to the laser propagation effects, however the BSI intensity serves as a good reference point to estimate which generation process dominates.

Chapter summary

- The semiclassical model predicts that a minimum intensity of 4.8×10^{14} W/cm^2 is needed in order to generate 100 eV photons from neon.
- For a single harmonic two conditions need to be fullfiled for efficient generation: $L_{\mathrm{med}} > 3\times L_{\mathrm{abs}}$ and $L_{\mathrm{coh}} > 5\times L_{\mathrm{abs}}$. For 100 eV radiation, neon has a $L_{\mathrm{abs}} = 2.1$ cm.
- For intensities below I_{BSI}, the phase-matching is experimentally optimized by changing the generation gas pressure, laser energy and beam size, and medium position with respect to the focus.
- The energy scaling scheme predicts the need of a focusing optic with a focal length of tens of meters in order to keep the ionization level low. Nevertheless, it is still possible to generate harmonics with shorter focal lengths at higher ionization levels, which has the additional advantage of increasing the continuum bandwidth.
- For the extreme case of sub-cycle depletion, a continuum can be generated over a extremely broad bandwidth, if the XUV beam is spatially filtered. This occurs approximately at an intensity of 4.5×10^{15} W/cm^2 for neon.
- Three generation regimes are identified: below-BSI, above-BSI and depletion intensity regime.

Chapter 3

Experimental setup

As discussed in the previous chapter, in order to efficiently generate high-harmonics using the LWS-20 laser system a loose-focusing geometry needs to be employed. In this chapter the experimental setup through which these ideas are implemented is presented.

In the first part of the chapter, the general HHG beam-line layout is described along its different components. The NIR beam focus characterization results for both a 8 m and 16 m focusing geometry are then shown. Among other experimental parameters, the focus dependence on initial beam size and focus adaptive mirror defocusing are finally described, due to their relevance to the HHG process.

In the second part of this chapter, the devices at the XUV experimental chamber are presented. Particular emphasis is done on the XUV beam characterization devices: the XUV profiler, the XUV spectrometer, and the absolutely calibrated XUV energy photodiode. The ion microscope, the main device for experiments with the XUV beam, is described in detail in section 5.1.

3.1 HHG experimental setup

3.1.1 Beam-line layout

After the beam is compressed through the reflection on the four chirped mirrors and a small portion from the center of the beam is coupled out for the CEP measurement, the beam is sent in the upward direction (with a polarization maintaining periscope) towards a rotating mirror. This mirror is part of the automated beam-line system at the MPQ. There, a set of motorized mirrors and cameras allow aligning and sending the beam towards different experimental chambers located in the building. After aligning the beam on this mirror and setting it towards the gas harmonics setup, a second periscope sets the beam to the right height. Therefore, after the chirped mirrors there is a total of five enhanced silver mirrors, before the beam enters the experimental setup. Detailed information on the beam-line design and construction can be found in reference [51]. Figure 3.1 shows the beam-line schematic, as seen from above, when using a 16 m focusing mirror.

For alignment into the setup, a motorized flip mirror, which sends the beam to an iris outside is positioned at the entrance of the focusing chamber, (see figure 3.2). By reducing the beam

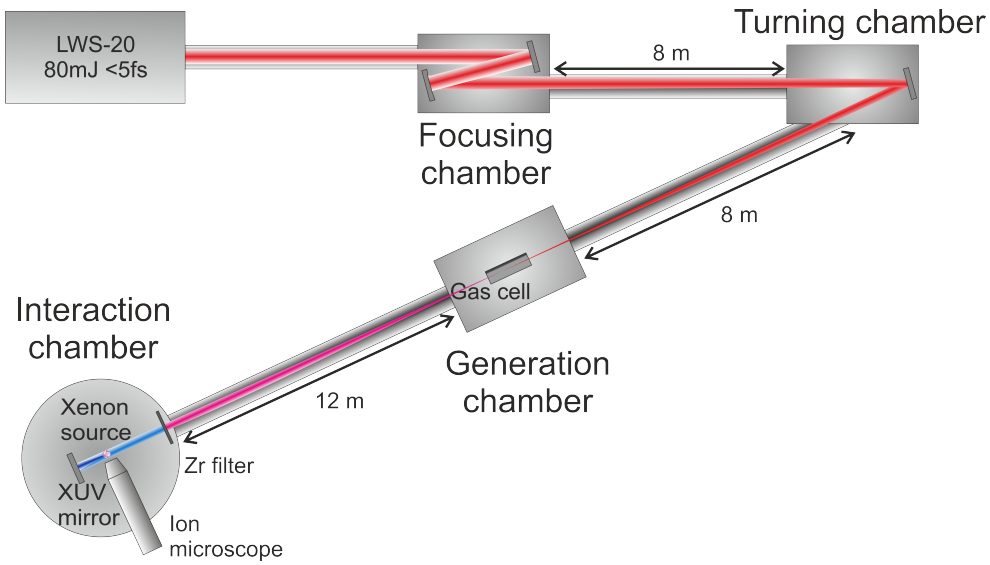

Figure 3.1: High-harmonic generation experimental setup for the 16 m focusing geometry.

size with the iris at the entrance of the compressor chamber, the beam is aligned to this iris. Following the beam propagation, the two mirrors in the focusing chamber correspond to a flat and a 16 m focal length mirror respectively. They are set up in such a way that the distance between them is maximized and the lateral separation is minimized while avoiding any clipping of the beam. This is done to minimize the astigmatism introduced by the focusing mirror. The focusing mirror is mounted on a motorized mount in order to further align the beam into the generation chamber while in vacuum.

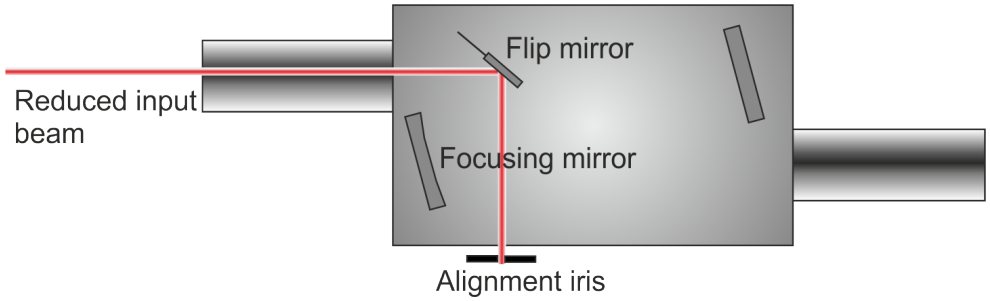

Figure 3.2: Focusing chamber diagram showing the alignment of the input beam.

After 8 m propagation the beam enters the turning chamber, which as its name says contains a single flat mirror which 'turns' the beam towards the generation chamber. The beam size is approximately 25 mm on this mirror, which still does not get damaged. This mirror is the last one before generating the XUV beam, therefore the pulse characterization setup described in section 1.4 is located also in this chamber, just after the beam is reflected on the turning mirror. This mirror is also mounted on a motorized stage in order to align the beam into a reference on the experimental chamber while in vacuum. For the use of a 8 m focal length mirror instead of the 16 m, the second mirror on the focusing chamber is replaced by a flat

one, and two more mirrors are included in the turning chamber: another flat one and the 8 m focusing mirror. These mirrors are aligned such that the astigmatism is minimized by reducing the reflection angle down to ~ 5° on the focusing mirror.

After another 8 m propagation the NIR beam is focused into the generation chamber. The chamber's cover is transparent, allowing the direct observation of the generation setup, which eases the alignment. Details about the focus characterization are described in the next section. As generation gas, neon is mainly used in order to achieve photon energies around 100 eV, though, argon and helium are also used for other purposes. The gases flow through a 1.5 mm exit diameter supersonic de Laval gas nozzle, or are contained in gas cells of varying lengths. The results achieved with each of the targets and media are described in detail in the next chapter.

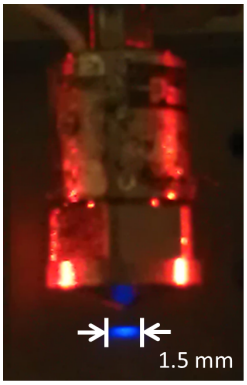

Figure 3.3: Supersonic de Laval nozzle with argon as the generation medium. The generated plasma can be used as an initial reference for the XUV beam optimization.

The gas nozzles were originally designed for laser-plasma experiments, providing high and homogeneous densities in the area close to the nozzle's exit [114]. These characteristics are not strictly necessary for HHG but it was still useful to have such nozzles available, as it is described in the next chapter. One of the advantages is the possibility to observe the generated plasma directly and use its brightness as an initial reference for the optimization of the XUV beam (see figure 3.3, which shows a gas nozzle in operation with argon as the generation medium).

In addition, fixed-length gas cells of 5 cm, 10 cm, 20 cm, and 30 cm, with 2 mm opening are used. For alignment of the different components a motorized holder is used. It contains four motorized stages to transversally align both the entrance and exit position of the gas cell, in addition to a long range translation stage which allows to easily switch between the nozzle and the cell. Figure 3.4 shows the motorized holder with the 10 cm cell and the nozzle, with the respective alignment stages.

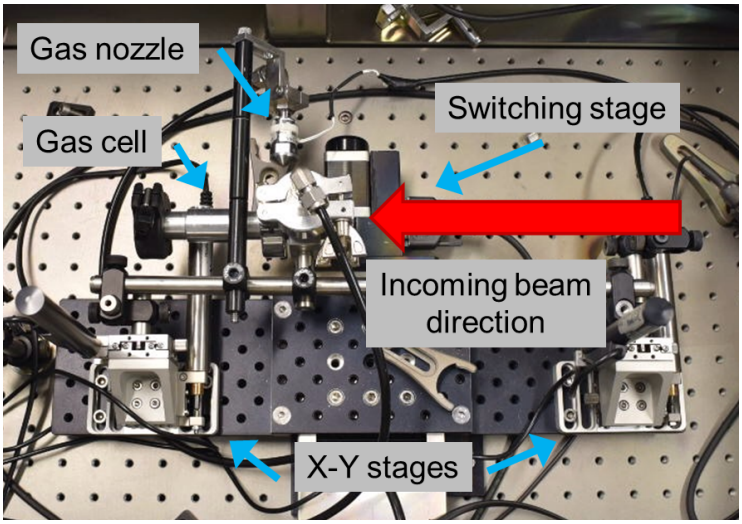

Figure 3.4: HHG target. The switching stage allows to exchange between the gas nozzle and cell, which are transversally aligned with the X-Y stages.

3.1.2 Laser focus

Focus characterization

In order to measure the focus of the NIR beam, neutral density (ND) filters are placed at the entrance of the compressor chamber. At least an optical density of 4.5 is needed in order to avoid nonlinearities in the observation window of the generation chamber. After entering the generation chamber, a flip mirror sends the beam outside of the chamber onto a beam profiler camera (Grasshopper2, Point Grey). The camera is positioned such that it images the plane where the nozzle is located. With this system the focus spot is measured and then optimized with the adaptive mirror before the generation of harmonics. It is worth noting that the neutral density filters have reduced transmission below 700 nm and therefore the focus measurement and optimization is only done for the longer wavelengths. However, if the OPCPA system is properly aligned, the beam properties of the shorter wavelengths are comparable to the ones at longer wavelengths. This was tested by optimizing the beam using only the 2B amplification stage (see figure 3.8).

As explained in chapter 1, the adaptive mirror corrects for wavefront aberrations up to its location before the compressor chamber. After that there is a total of 14 mirrors (16 for the 8 m focusing geometry) until the beam reaches the generation chamber, therefore an additional correction is needed to have a good quality focus for HHG. Additional astigmatism correction is particularly important given the employed focusing geometry. In general correcting for this aberration is enough in order to have a good focus profile, but additional higher order aberrations can further improve the quality. For optimization, the focus shape and energy content in the FWHM are monitored. For an ideal Gaussian beam 50% of the energy is contained in the FWHM.

Because the adaptive mirror settings change from day to day the relative aberrations that need

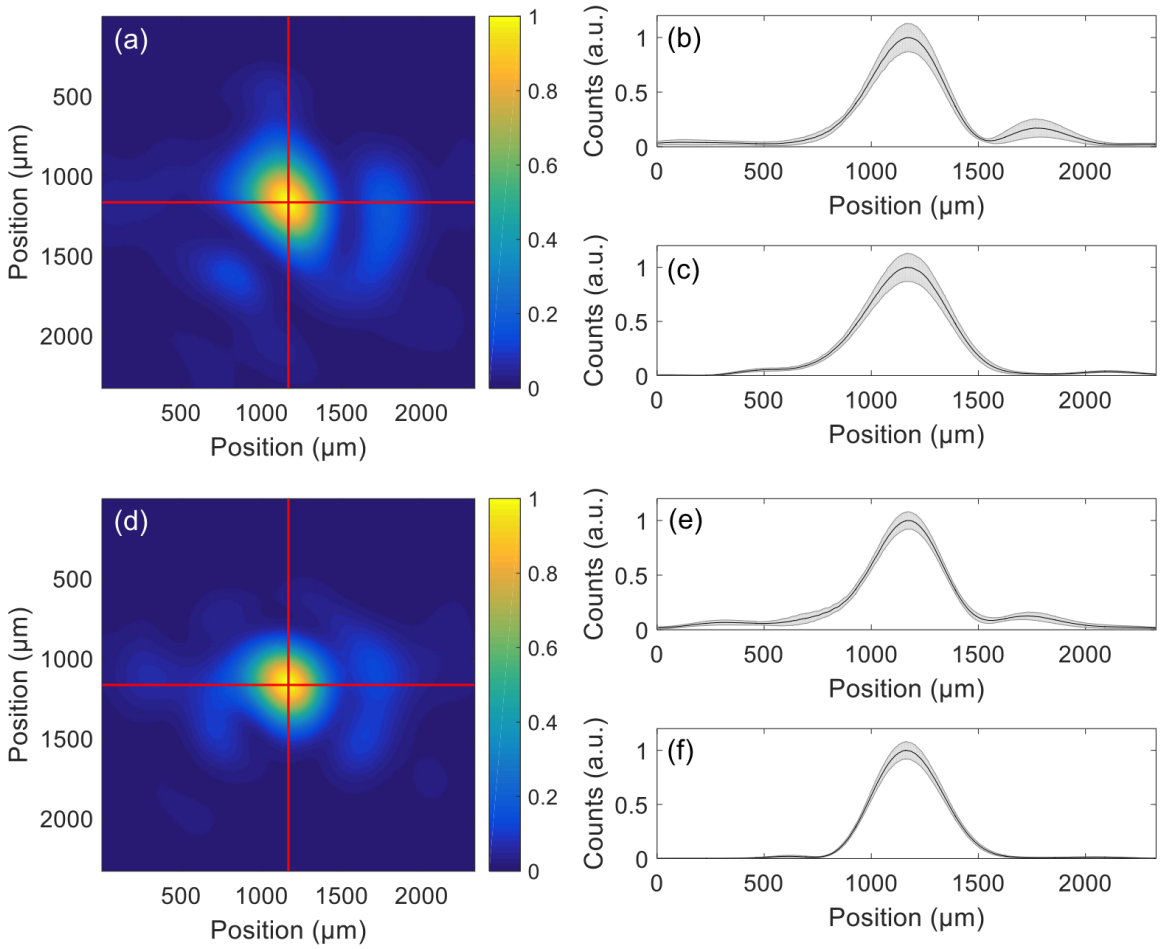

Figure 3.5: (a) Unoptimized focus exhibiting a non-symmetric shape with an average diameter of 424 μm FWHM. The red lines show the line-out positions. (b) Line-out in x-axis with a FWHM diameter of 392 μm. (c) Line-out in y-axis with a FWHM diameter of 442 μm. The shaded area represents the RMS error in the detected counts. (d) Optimized focus with a symmetric shape and an average diameter of 381 μm FWHM. Red lines represent the line-out positions. (e) Line-out in x-axis with a FWHM diameter of 383 μm. (f) Line-out in y-axis with a FWHM diameter of 377 μm. Shaded area represent the RMS error in the detected counts. Before and after optimization 34% of the energy was contained in the FWHM.

to be compensated also change. The first step is to find the right defocusing of the adaptive mirror by minimizing the beam size at the nozzle plane. Even though this minimal focus size is not necessarily the optimum beam profile used for HHG, it is a good measure of the beam quality on that day. After the minimum focal spot size is found, the higher order aberrations are compensated such that the beam is as symmetrical as possible, and contains more than 30% of its energy in the FWHM (see for example figure 3.5).

For the image analysis,an average of 100 shots is taken, after centering each image to its first moment. The beam pointing is defined as the RMS fluctuation of the position of this first

moment. In order to extract the beam properties from the images, each is first independently filtered with a Fourier filter to find out its *peak value*. Knowing this, the *effective peak* is defined as all pixels with counts above or equal to 95% of this *peak value* and the *half-maximum* is defined as all pixels above or equal to 50% of the *peak value*. Then the peak flux is calculated as the total counts within the *effective peak* divided by its area, and the beam size is calculated taking an effective circle of area equal to the total area of the *half-maximum* pixels. The equivalent circle approach is taken in addition to the size of the x-axis and y-axis line-outs to account for inhomogeneous beam shapes. At focus these two approaches give similar results, but the equivalent diameter approach is more accurate outside the focal plane. The line-outs are constructed by integrating over a 5 pixel window at the positions marked by the red lines, which are position at the first moment of the measured signal. The shaded areas represent the RMS error in the integrated counts.

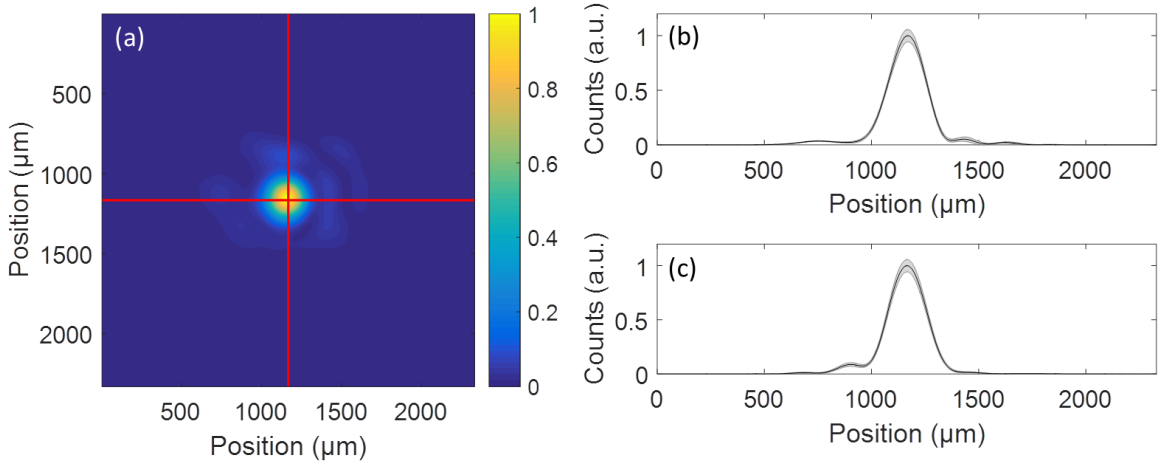

Figure 3.6: (a) Optimized focus for the 8 m focusing geometry, with a FWHM spot of 201 μm, an RMS pointing stability of 63.2 μm (7.9 μrad) and a RMS peak flux fluctuation of 6%. The red lines show the line-out positions. (b) Line-out in x-axis with a FWHM diameter of 198 μm. (c) Line-out in y-axis with a FWHM diameter of 201 μm. The shaded area represents the RMS error in the detected counts.

Figure 3.6 shows a focal spot obtained after optimization with the 8 m focusing geometry. From these definitions, the focus on figure 3.6 has a FWHM size of 201 μm, a pointing stability of 63.2 μm and the peak flux RMS fluctuation is approximately 6%. Figure 3.7 shows an optimized focus under the 16 m focusing geometry. In this case the focus reaches a size of 365 μm, a RMS pointing stability of 86.1 μm with a peak flux RMS stability of 4%. The low peak intensity fluctuations reached are the results of covering the laser to minimize fluctuations due to air movement. Without this cover, intensity fluctuation above 15% are present (some results presented in next chapter were done without this laser cover, significantly affecting the stability of the generated XUV beam).

Both the measured focus shape and temporal intensity have some additional part of the energy outside their main peak. For an accurate intensity estimation, both the counts on the

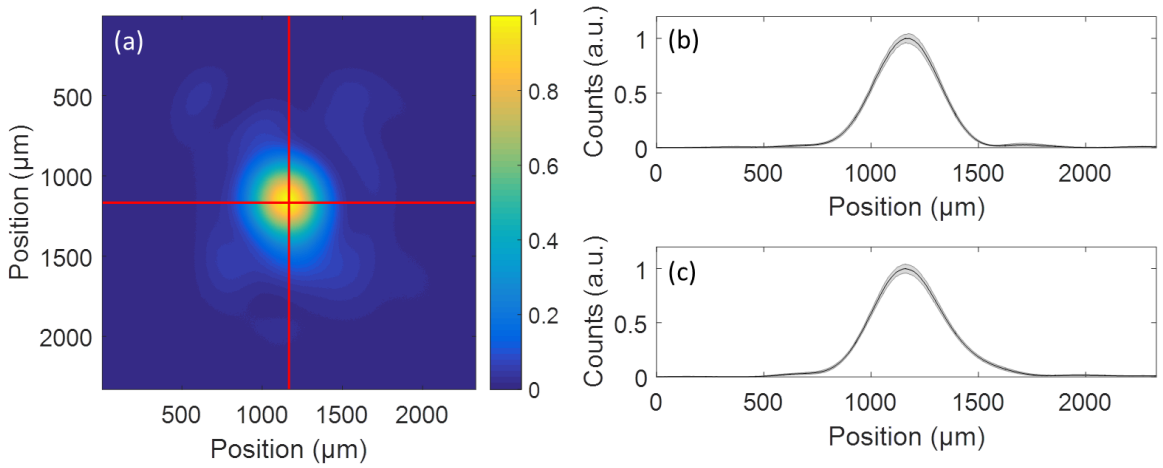

Figure 3.7: (a) Optimized focus for the 16 m focusing geometry, with a FWHM beam size of 365 μm, a RMS pointing stability of 86.1 μm (5.4 μrad) and a peak flux RMS fluctuation of 4%. The red lines show the line-out positions. (b) Line-out in x-axis with a FWHM diameter of 347 μm. (c) Line-out in y-axis with a FWHM diameter of 376 μm. The shaded area represents the RMS error in the detected counts.

camera and on the calculated temporal profile (determined through the chirp-scan algorithm described in section 1.4) are integrated and then normalized to the measured energy on target (38 mJ for both examples). The peak intensity then corresponds to the peak of the measured spatio-temporal intensity after normalization. For the focus generated under the 8 m focusing geometry the peak intensity is estimated to be 1.0×10^{16} W/cm^2. As described in the previous chapter, this value is far above the depletion intensity for Neon. Doing the same for the focus generated with the 16 m focusing mirror, the intensity is estimated to be 3.0×10^{15} W/cm^2. This value is below the depletion intensity, but above the BSI intensity for neon. Both these values represent the intensities achieved regularly on other measurement days through at the corresponding focusing geometry.

Given that the focus characterization is done for wavelengths longer than 700 nm, the issue of having different beam sizes in the amplification stages for the region below and above 700 nm is not generally characterized. By optimizing the beam for the region above 700 nm, a focus of approximately 330 μm is reached for the region below 700 nm (see figure 3.8), for the 16 m focusing geometry. This focus difference should be taken into consideration in the interpretation of the following results.

Parameter scans

As described on the previous chapter, in order to achieve optimum phase-matching three different experimental parameters from the driving laser need to be scanned: the beam size at the entrance of the compressor chamber, the total beam energy and the focus position with respect to the generation medium. This means that the actual focus used for the optimal

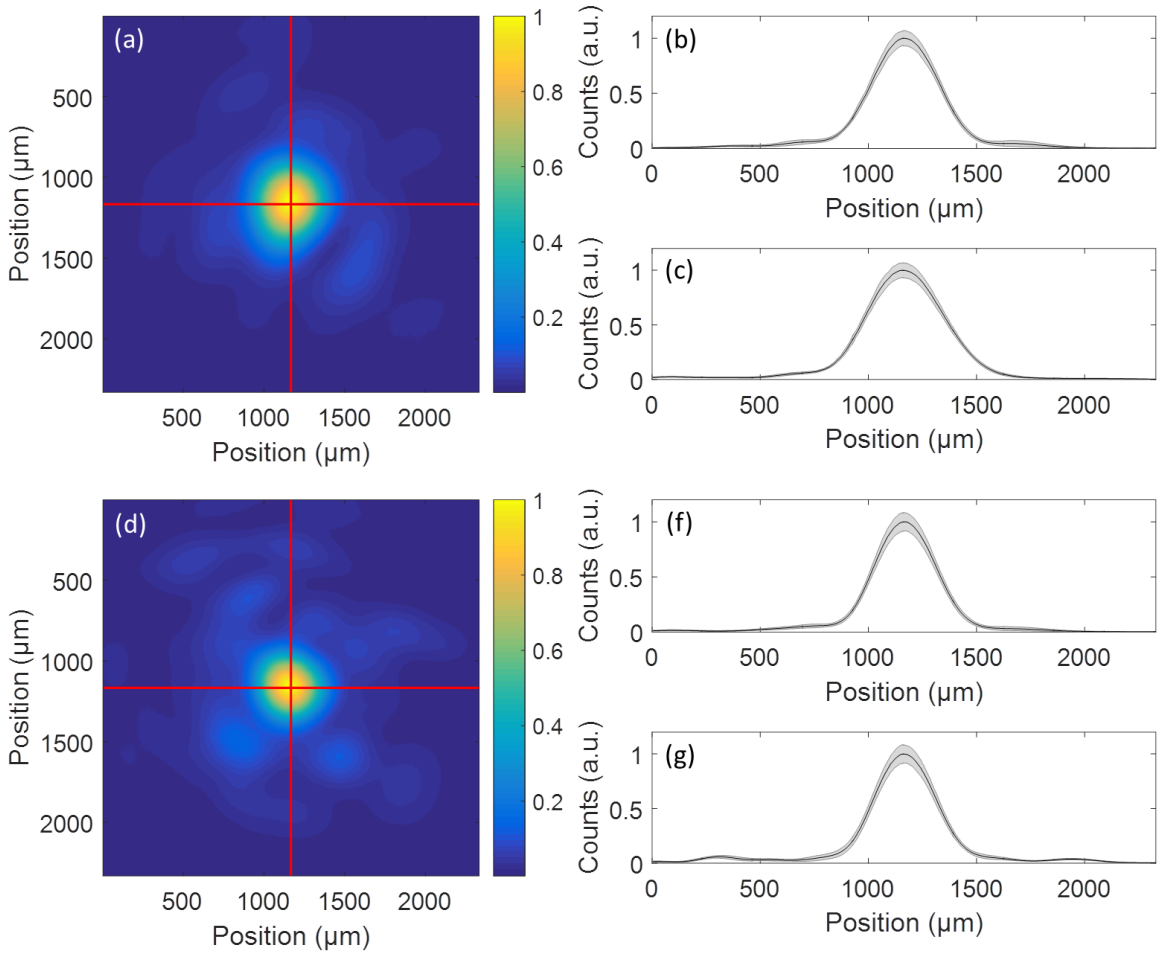

Figure 3.8: (a) Optimized focus for the region above 700 nm, under 16 m focusing geometry, with a FWHM beam size of 383 μm a peak flux RMS fluctuation of 6%. The red lines show the line-out positions. (b) Line-out in x-axis with a FWHM diameter of 354 μm. (c) Line-out in y-axis with a FWHM diameter of 405 μm. The shaded area represents the RMS error in the detected counts. (d) Optimized focus for the region below 700 nm, under 16 m focusing geometry, with a FWHM beam size of 331 μm a peak flux RMS fluctuation of 8%. The red lines show the line-out positions. (e) Line-out in x-axis with a FWHM diameter of 327 μm. (f) Line-out in y-axis with a FWHM diameter of 326 μm. The shaded area represents the RMS error in the detected counts.

HHG process could be bigger than the ones estimated above. In the following figures the peak intensity is plotted in normalized units, given that it also depends on the pulse duration and energy content from the different days.

The beam size before entering the compressor chamber can be reduced with a motorized iris, which has a maximum opening of 50 mm in diameter. Fig 3.9 shows how the focus size (black curve) and peak intensity (red curve) are affected by reducing the iris diameter, for the 16 m focusing geometry. It can be seen that the beam size is not significantly increased until the

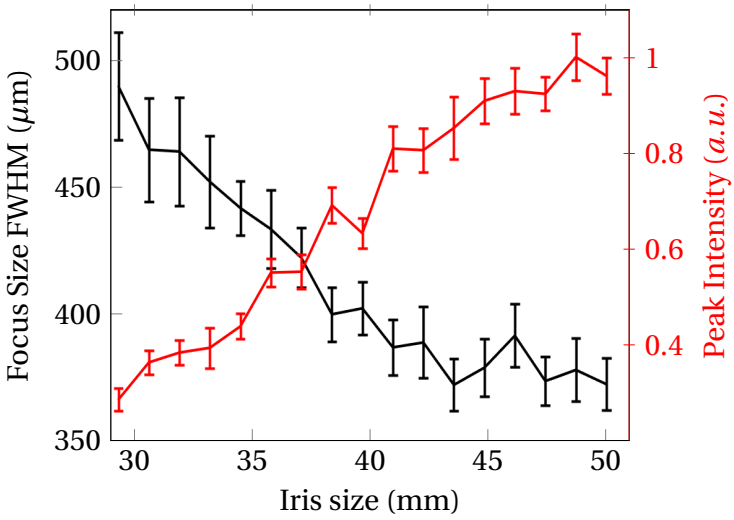

Figure 3.9: Measured focus size and peak intensity as a function of iris opening diameter, for the 16 m focusing geometry. Error bars represent the RMS error at each iris position.

iris is closed to around 43 mm. This can be explained by the fact that the size of the beam on 2A is 1.8 mm smaller than at 2B as explained in chapter 1, leading to an estimated size of 42 mm between 700-1020 nm at the iris. Given that the measured focus corresponds to wavelengths above 700 nm, no significant changes are observed when cutting the first few mm of the beam. The same can be concluded from the peak intensity as a function of iris size. For the 8 m focusing geometry, similar scans were performed but with a smaller iris size resolution (see figure 3.10).

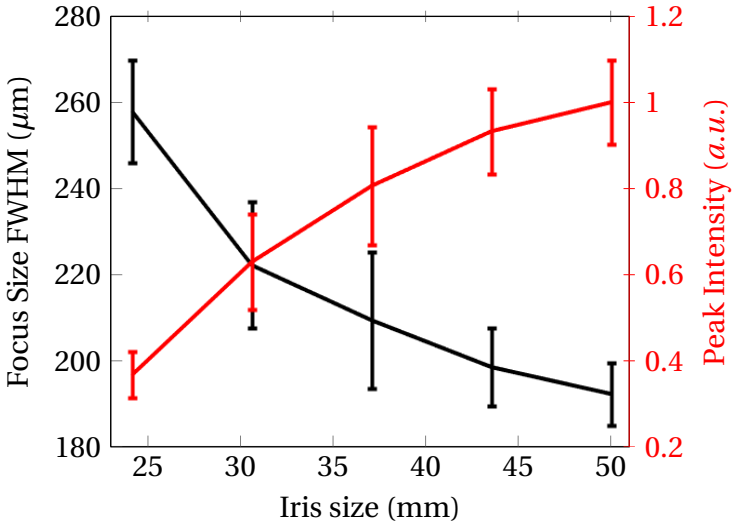

Figure 3.10: Measured focus size and peak intensity as a function of iris opening diameter, for the 8 m focusing geometry. Error bars represent the RMS error at each iris position.

Although reducing the iris size changes the beam energy, it could be necessary to do this without affecting the focus size, as explained in the previous chapter. For this purpose, homemade high-damage threshold broadband transmission ND filters were developed. These are installed on two motorized filter wheels just after the 2B amplification stage. Figure 3.11 shows the measured transmission of the different filters used. Using these transmission curves and the measured laser spectrum, transmissions of 90%, 75% and 10% are obtained. Given the possibility of using two of them simultaneously, the laser energy can be set to 1%, 7.5%, 9%, 10%, 56%, 68%, 75%, 81%, 90% and 100% of its original value. To achieve the 100% transmission, two substrates with AR coatings (the same as the one used for the BBO at the 2B stage) are used. This is done in order not to change the compression of the laser when using filters, due to dispersion in the material substrate of the filters. Additionally, these filters are used to control the intensity on target for the pulse characterization setup described in section 1.4.

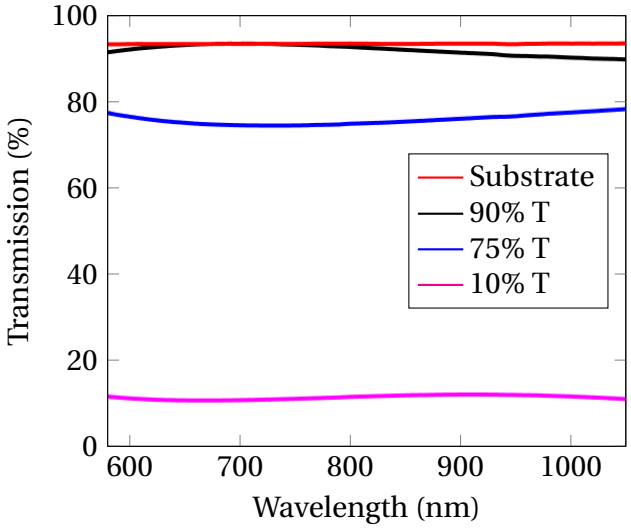

Figure 3.11: Spectral transmission for the substrate (red), 90% (black), 75% (blue) and 10% (cyan) filters used after the 2B stage to reduce the laser energy.

Finally, the longitudinal position of the focus with respect to the generation target is controlled with the adaptive mirror. After tilt, the next order aberration introduced by the mirror is the beam focusing or defocusing (defocusing Zernike polynomial coefficient, z). To understand how this aberration changes the longitudinal focus position, the mirror is calibrated for both the 8 m and 16 m focusing geometry. This is done using a HeNe laser positioned before the adaptive mirror and recording the focus size as a function of z. The HeNe laser is expanded to a beam size such that the focus size is comparable to the one of the LWS-20. By doing such scans at different camera positions it is possible to extract the focus position (P) as a function of z. In centimeters, the calibration for the 8 m focusing geometry lead to $P(z) = 80.9z$ and for the 16 m, $P(z) = 333z$.

Figure 3.12 shows the beam size in the target plane (black curve) and peak intensity (red curve) as a function of focus position for the 8 m focusing geometry. The 'zero' position is

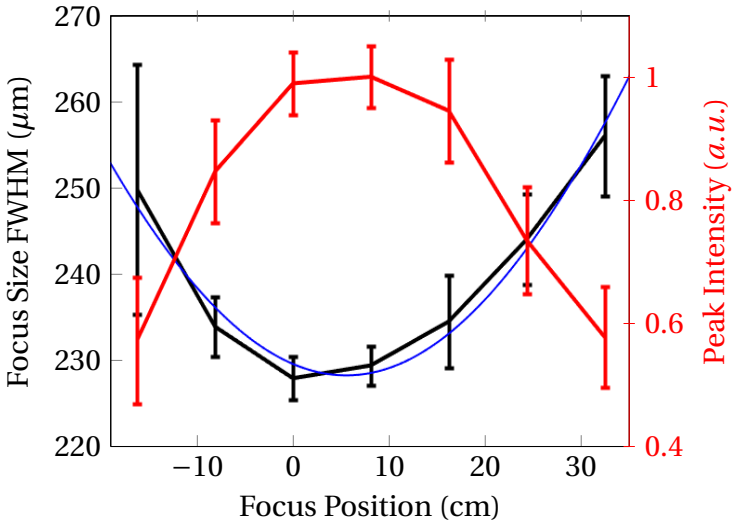

Figure 3.12: Measured focus size (black) and peak intensity (red) at the target position as a function of focus position for the 8 m focusing geometry. The blue curve shows the fit assuming a Gaussian beam providing a FWHM beam waist of 228 μm and a Rayleigh length of $z_R = 51$ cm.

defined as the position where the beam size is minimal at the target plane. As an approximation it can be assumed that the beam size $w(z)$ behaves as if it would be a Gaussian beam and therefore fitted by $w(z) = w_0\sqrt{1+(z/z_R)^2}$, where z is the longitudinal distance, w_0 the beam waist and z_R the Rayleigh length. This equation is valid for both $1/e^2$ radius as well as FWHM. From the fitting (blue curve) a FWHM beam waist of 228 μm and a Rayleigh length of $z_R = 51$ cm can be extracted. The changes in intensity are plotted as well (red curve), though the dependence on z is stronger than expected due to changes in the beam shape.

The same kind of analysis can be applied to a similar scan for the 16 m focusing geometry, as shown in figure 3.13. In this case the fitting leads to a beam waist of 376 μm and a Rayleigh length of $z_R = 167$ cm.

Real-time focus monitoring

In addition to the focus characterization setup described in the previous section, another setup is used in order to monitor the beam in real-time during experiments. The motivation for developing this secondary setup was the observation of slow-drift in focus position while working with the XUV beam. In case the focus position starts drifting, the experiments could be stopped and the beam be realigned, thus reducing systematic errors during the measurements. This is particularly critical during the few hours after pumping down the beam-line.

The real-time beam monitoring system uses a pierced focusing substrate with a 12 m ROC, positioned at the entrance of the experimental chamber. The diameter of the pierced hole is 1.5 cm. Figure 3.14 shows the substrate after installation at the entrance of the experimental chamber.

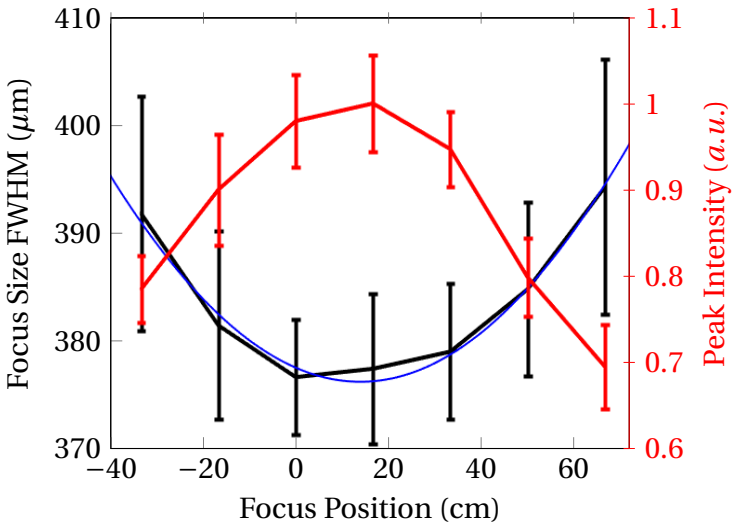

Figure 3.13: Measured focus size (black) and peak intensity (red) at the target position as a function of focus position for the 16 m focusing geometry. The blue curve shows the fit assuming a Gaussian beam providing a beam waist of 376 μm and a Rayleigh length of z_R = 167 cm.

Figure 3.14: Pierced substrate for focusing the laser beam back after HHG.

Given that after HHG the NIR beam has a much bigger divergence than the XUV beam, the latter goes through the piercing in the substrate, while the outer part of the NIR is back reflected into the generation chamber. Again, this substrate is aligned such that the beam returns almost on the same path as the incoming beam, realizing a 4f imaging. Another small substrate couples the beam outside into a camera.

With this system the gas cell can be precisely aligned. Before installing the cell the total number of counts on the camera are recorded. Then, after positioning the cell in place for HHG, the total number of counts are measured, and used as reference for the alignment of the four

axes of the cell. A transmission of 80−90% is in general achieved when the cell is aligned. This value can be monitored in real-time, and if it drops during a measurement the cell or beam can easily be realigned.

Moreover this setup could be used to study the NIR beam after generation. Unfortunately the beam quality is not good enough to characterize the properties of the beam focus. A reason for this might be that only the exterior part of the beam is back reflected, changing the focus. Additionally, strong nonlinearities are experienced by the NIR when going through the output window. A smaller piercing on the substrate could be used to improve the reflected focus quality, in addition to coating the substrate with an AR coating such that a smaller portion of the beam energy is reflected.

3.2 Experimental chamber and XUV diagnostics

3.2.1 Chamber design

As described in the previous section, after the XUV beam is generated it travels collinear with the driving beam in to the experimental chamber located 12 m away. The XUV beam goes through the pierced mirror and into the experimental chamber, where the NIR beam is filtered out using thin metallic filters. Depending on the spectral region of interest, different filters are used. The filters are made from Aluminum, Zirconium and Silicon, and their thickness varies around a few hundred nanometers, depending on the application. Figure 3.15 shows the transmission for these 3 different materials for a thickness of 200 nm [115]. The Aluminum and Silicon filters can be used for calibrating the spectrometer given their sharp absorption edges at 73 and 100 eV respectively (see appendix B). For the goal of experiments at 100 eV, the zirconium filters are mainly used.

The manufacturing of these filters becomes very challenging because of their reduced thickness, and the final product is extremely fragile. Small pressure variations, can damage the filters and therefore it is common that small holes are present on them. In order to minimize the transmission of the NIR, usually two filters are used at the same time for the XUV characterization. Additionally, in some cases presented in the next chapter, the used filters were mounted on a mesh for additional support. The mesh has a transmission of 82%, corresponding to its filling ratio, and can significantly affect the quality of the beam profile. The filters are mounted on two motorized filter wheels located at the entrance of the experimental chamber which allow their exchange without venting the chamber.

After filtering out the NIR beam, the XUV radiation enters the experimental chamber, which is schematically represented in figure 3.16. There is a translation stage at the center of the chamber which allows to control which device is used for beam characterization. On the left side there is a silver mirror (not shown in figure 3.16) which sends the beam into a reference iris. When initially aligning the beam-line, the NIR is irised down to a few millimeters and the metallic filters are removed in order to see this beam at the reference. The last mirror in the beam-line is used for alignment to this reference.

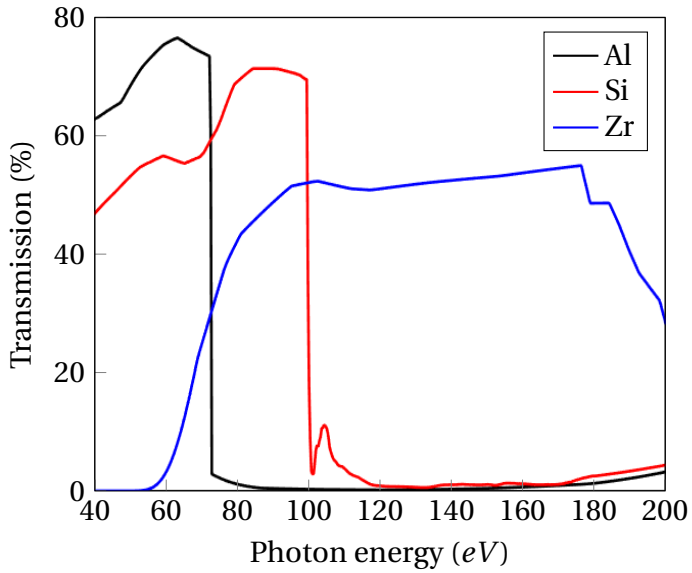

Figure 3.15: Transmission curve for 200 nm thick Aluminum (black), Silicon (red) and Zirconium (blue) [115].

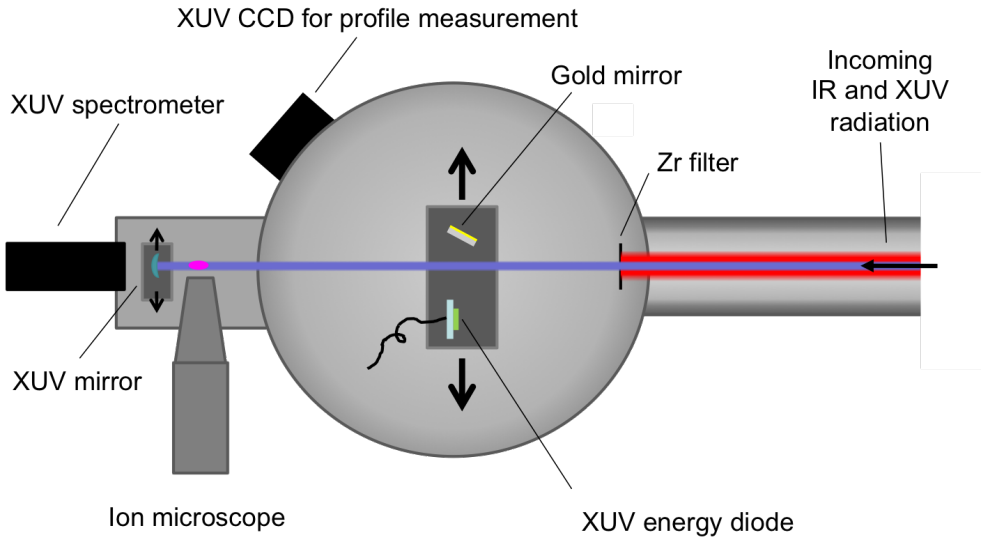

Figure 3.16: Schematic of the experimental chamber setup.

An XUV photodiode is located to the right of the alignment mirror and to its right there is an XUV surface quality gold mirror which sends the beam into an XUV CCD to measure the beam profile. Between the diode and the gold mirror there is enough space for the beam to go through into the ion microscope (described on chapter 5) and the XUV spectrometer. The XUV photodiode, beam profiler and spectrometer are described on the following section. Before the spectrometer there is another motorized stage which can move in and align the XUV focusing mirrors for experiments, which are described in chapter 5.

3.2.2 XUV characterization devices

For the initial characterization of the of the XUV beam three main parameters are of importance: the pulse energy content, beam profile quality and spectrum. These can be measured with the XUV photodiode, CCD profiler and spectrometer respectively.

The XUV photodiode corresponds to the model AXUV576C manufactured by Opto Diode Corporation. It has a 24.01×24.01 mm^2 active region and its main advantage is the linear dependence of the efficiency with photon energy, at the spectral region of interest (see figure 3.17).

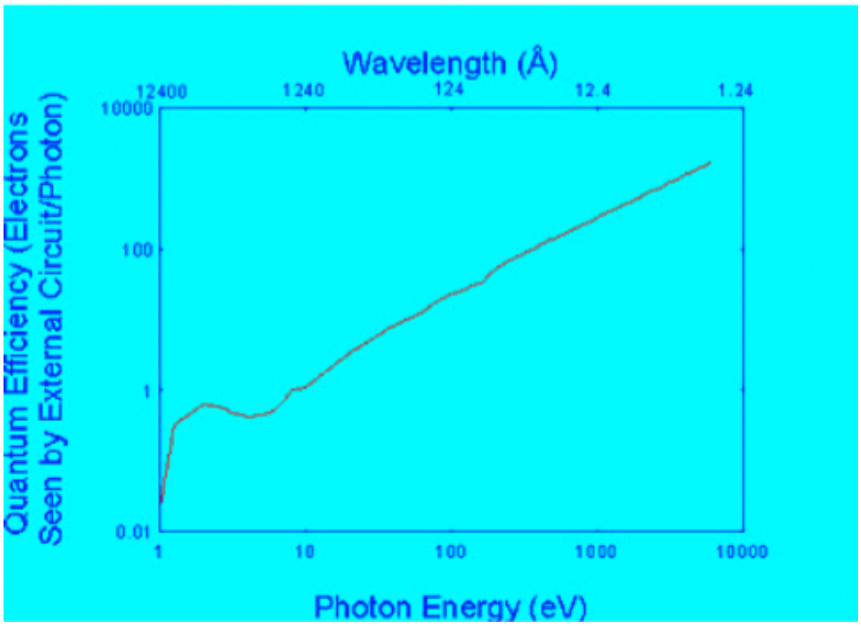

Figure 3.17: Quantum efficiency versus photon energy for the XUV photodiode from the AXUV series. (Source: Opto Diode Corp.)

From this curve it can be concluded that 3.7 eV are need to generate an electron-hole pair for photons from 10 eV to a few keV. Therefore the total pulse energy on the diode is given by

$$E = \frac{3.7}{g} \int V(t)\,dt, \tag{3.1}$$

where $V(t)$ is the time dependent voltage measured on the diode, after amplifying it with a current amplifier (DLPCA-200, Femto) set to a gain of g (in units of impedance) and the integral goes over the whole pulse duration.

The XUV spectrometer uses a 30×50 mm^2, 1200 lines flat-field grating (Hitachi) at an angle of 84.4° and is available at Ultrafast Inovations GmbH. At the current settings it images a point source located over 3 m away into an XUV camera (Newton, Andor). Figure 3.18 shows the image plane and corresponding wavelength position onto the camera for an 8 m distance source.

This provided figure serves as an approximate calibration, but by using the XUV beam a more accurate calibration can be obtained (see appendix B). The XUV camera in use has a chip size of 26.6 × 6.7 mm^2, a pixel size of 26 × 26 μm^2 and can be triggered at 10 Hz. However, unless specified otherwise, the images shown in the next chapter are all with a 2 × 2 binning. Additionally, the CCD chip has a slight efficiency drop at photon energies above 100 eV. This drop is corrected for the data presented in the next chapter (see appendix C).

Finally the beam profiler (iKon, Andor) has a beam chip size of 27.6 × 27.6 mm^2 and a pixel size of 13.5×13.5 μm^2. This camera can only be triggered at 3−4 Hz depending on the binning, but the readout time is fast enough to separate the single shots.

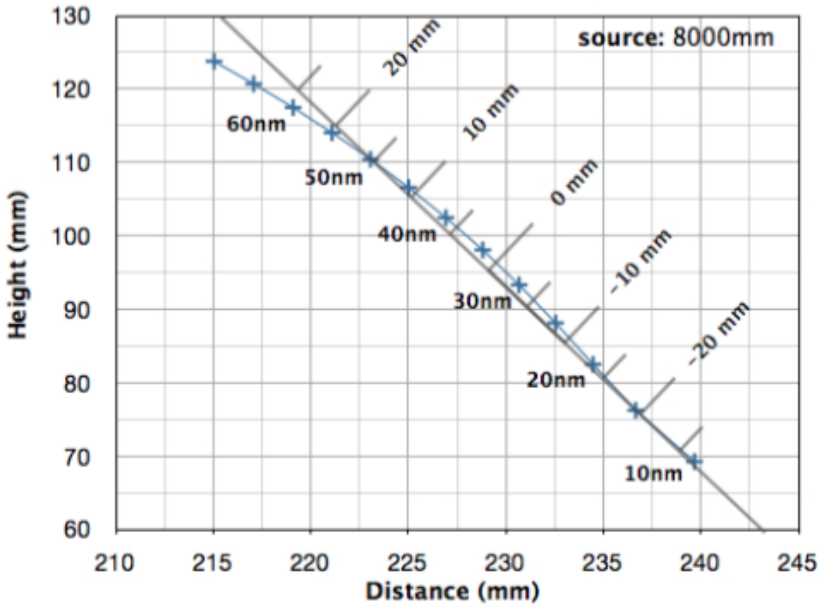

Figure 3.18: Image plane on the XUV camera and the corresponding wavelength positions. (Source: Ultrafast Inovations GmbH).

Chapter summary

- The experimental setup allows the use of a loose-focusing geometry in addition to the alignment and characterization of the NIR driving laser focus.
- Through the use of a 8 m and 16 m focal length mirrors, intensities of 1.0×10^{16} W/cm^2 and 3.0×10^{15} W/cm^2 are achieved respectively. These values allow to drive the HHG process at the depletion and above BSI intensities for neon.
- A real-time focus monitoring system allows to detect possible drifts during experiments with the XUV beam, reducing sources of systematic errors during long measurements with the system.

- The XUV pulse energy, beam profile and spectra are characterized in single shot. By monitoring these properties as a function of the phase-matching parameters, it is possible to optimization of the XUV source in a time-efficient manner.

Chapter 4

High-harmonic generation results

In chapter 2 the correct energy scaling procedure for the HHG process is described for the LWS-20 system as the driving laser. With the experimental setup described in the previous chapter, it is possible to control all the relevant parameters in order to drive the HHG process at phase-matched conditions. Through the use of a 8 m and 16 m focusing mirrors, it is possible to drive the HHG process at intensities up to approximately 10^{16} W/cm^2 and 3×10^{15} W/cm^2, respectively. These driving intensities correspond to the depletion intensity and above-BSI intensity, as described in chapter 2.

In this chapter, the general HHG optimization procedure is described, after which the main results for the different generation conditions are shown. These are first described for the 8 m focusing geometry, where the successful tagging of the CEP-dependent XUV spectra is first demonstrated, followed by the main results under this depletion intensity regime. Then the results for the 16 m focusing geometry are described along with simulations supporting the interpretation of the measured results. The simulation results are courtesy of B. Major and K. Varjú from the Department of Optics and Quantum Electronics at the University of Szeged.

4.1 Optimization procedure

After temporal compression and optimizing the near-infrared (NIR) focus, the gas nozzle's exit is positioned near the focus. If the previous steps are realized properly, and the backing pressure is slowly increased a plasma should become visible at the nozzle's output, arising from the gas ionization. At this point, the different XUV detection devices should show a signal, and the optimization procedure described in the next sections can be carried out.

4.1.1 GDD scans

The first step on the HHG optimization procedure is to make sure the laser pulses are compressed as they enter the generation medium. The pulse characterization device described in chapter 1 is positioned after the last mirror in the beamline, but it uses a silver mirror to send the beam into the BBO for SH generation, which might not have a completely flat phase. Even if it is not the case, this step helps to discard any possible mistake done when using the chirp-scan algorithm.

The test consists in scanning the GDD with the Dazzler while monitoring the XUV radiation cutoff position. When the harmonics are driven at a low ionization regime, the cutoff increases with increasing intensity, as explained in chapter 2. If the pulses are initially chirped, changing the GDD would shorten them and therefore the cutoff would increase. To make sure the HHG process is driven below the BSI intensity, the iris before the compressor is closed as much as possible such that there is still XUV signal.

Unless specified otherwise, for all of the spectrum measurements, 100 shots are averaged and a 10 pixel wide area is integrated to construct one-dimensional line-outs . The vertical position of the integration area is chosen such that the integrated signal is the highest. A typical GDD scan is shown in figure 4.1, where an optimum around 1202-1204 fs^2 is seen. The GDD value shown is the total amount compensated with the Dazzler, which for that day should have been 1195 fs^2 for optimal compression according to the chirp-scan (this 7 fs^2 would elongate a 4.5 fs pulse to 6.2 fs if higher-order phase terms are not present).

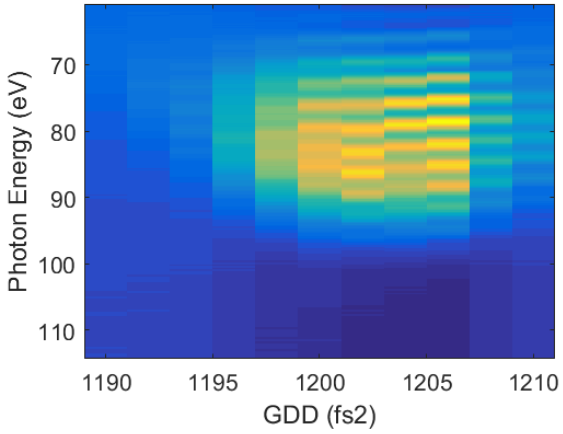

Figure 4.1: XUV spectra as a function of GDD for a generation intensity of 4.8×10^{14} W/cm^2. The maximum cutoff is obtained at 1202 fs^2.

The cutoff energy is approximately 100 eV, which according to equation 2.5 corresponds to an intensity of 4.8×10^{14} W/cm^2, which is below the BSI intensity of neon (8.6×10^{13} W/cm^2). It is important to notice that it is possible to extend the cutoff by chirping the driving pulse as reported on references [116] or [117]. However, for the first case the pulses are 28 fs long (817 nm central wavelength) and for the second case the chirp was not linear. The harmonic line energy change with GDD is also observed in [116]. By simulating the single-atom response (by solving the time-dependent Schrödinger equation) we confirm that adding a positive or negative linear chirp to a 4.5 fs long pulse reduces the cutoff, as shown in figure 4.2. Simulations are done for a peak intensity of 5×10^{14} W/cm^2 when no chirp is added.

As it is explained in section 4.4, for intensities above the saturation regime, the pulse experiences strong phase modulations during propagation. Optimizing the pulse duration for higher cutoff at low intensities is a good starting point, but the optimum GDD yielded by these scans might not be the optimum, for example, when the driving pulse experiences strong

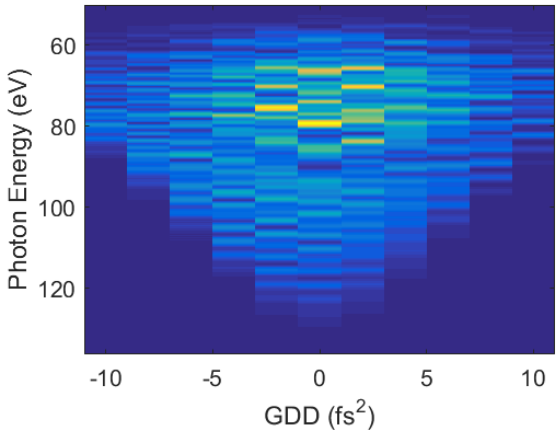

Figure 4.2: Single-atom response simulation for a GDD scan with a 4.5 fs long driving pulse with a peak intensity of 5×10^{14} W/cm^2. (Courtesy of B. Major.)

phase modulations during propagation (see section 4.4.4). Further explorations need to be done in order to make definite conclusions on this topic.

4.1.2 Parameter scans and phase-matching

Once the pulses used for generation are chirp-free, the first figure-of-merit used for optimizing the XUV beam is the pulse energy in the zirconium transmission window (above 70 eV), measured with the XUV photodiode. A typical diode measurement is shown in figure 4.3. The integrated signal corresponds to 0.861 $V\mu s$, which for this case is a factor of 2 lower because of an impedance mismatch[1].

Accounting for this mismatch and using the procedure described in section 3.2.2 for a gain of 1000 V/A used in that case, the integrated signal would correspond to an energy of 6.37 nJ on target. In this case two 150 nm zirconium filters with mesh were used. Taking the zirconium transmission of 34% at 90 eV for 300 nm (instead of the 200 nm shown in figure 3.15) and the 82% mesh transmission of each filter[2], leads to a total transmission of 23%, which would correspond to an energy of 27.7 nJ after generation inside the transmission window of the filter.

Unless specified otherwise for all parameter scans an average of 100 shots is taken per step. This average is plotted along with the standard error, which might not be the best indicator given the slow drifts of the system. This topic is further discussed at the end of this section.

[1] The digitizer card used (Acqiris, AP240) only measures with 50 Ω impedance, which was confirmed by comparing to a high-impedance scope.

[2] This neglects any possible overlap between the meshes.

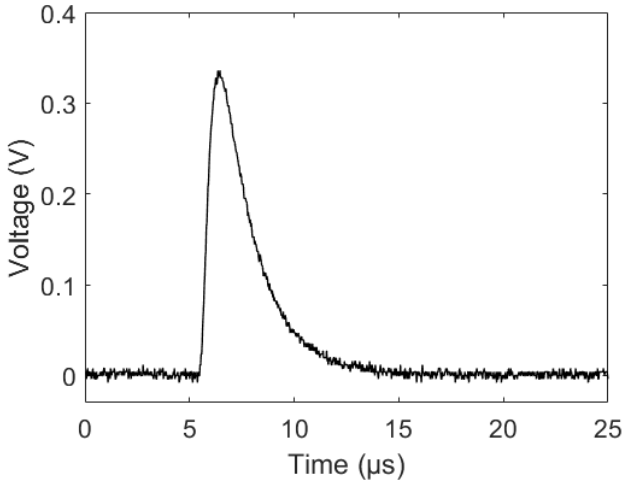

Figure 4.3: Raw signal measured from the XUV photodiode, which corresponds to an energy of 27.7 nJ after generation inside the transmission window of zirconium.

Pressure

The first phase-matching parameter to scan is the gas pressure of the generating medium (*pressure scan*). Figure 4.4 (a) shows a nozzle's backing pressure scan versus measured energy for the 16 m focusing geometry with neon as the generation gas. A gas density 10 times smaller than the backing pressure is expected up to one diameter away from the nozzle's aperture [114]. The plot shows that the signal rapidly increases with increasing backing pressure but then reaches a value which slowly decreases. Because of this, when using the nozzle the pressure is fixed to a value of around 4-5 bar instead of scanning the parameter each time. The same behavior was observed on other days for both the 8 m and 16 m focusing geometry for backing pressures up to 10 bar, which was the gas-line limit.

A typical pressure scan for the 10 cm gas cell is shown in figure 4.4 (b). In this case, the pressure dependence behaves as expected from the theory: at low pressures the signal increases with increasing pressure, which then saturates and finally decreases. A clear optimum is visible with a width of a few millibars. In simple terms, this initial increase at lower pressures is due to better phase-matching and the decrease at higher pressures is due to loss of phase-matching and increase of absorption, as described in section 2.2.

Beam diameter

The next parameter scanned is the NIR beam diameter before the compressor chamber, which is controlled with the motorized iris (*iris scan*). As seen in section 3.1.2, cutting out the first few milliliters from the beam does not have such an important effect, which is also visible on the XUV energy (see figure 4.5). Here the XUV pulse energy is plotted against iris diameter for the 16 m focusing geometry. It can be seen that the energy slightly increases by closing the iris from 50 mm to 46 mm, which is attributed to better phase-matching. A good approach

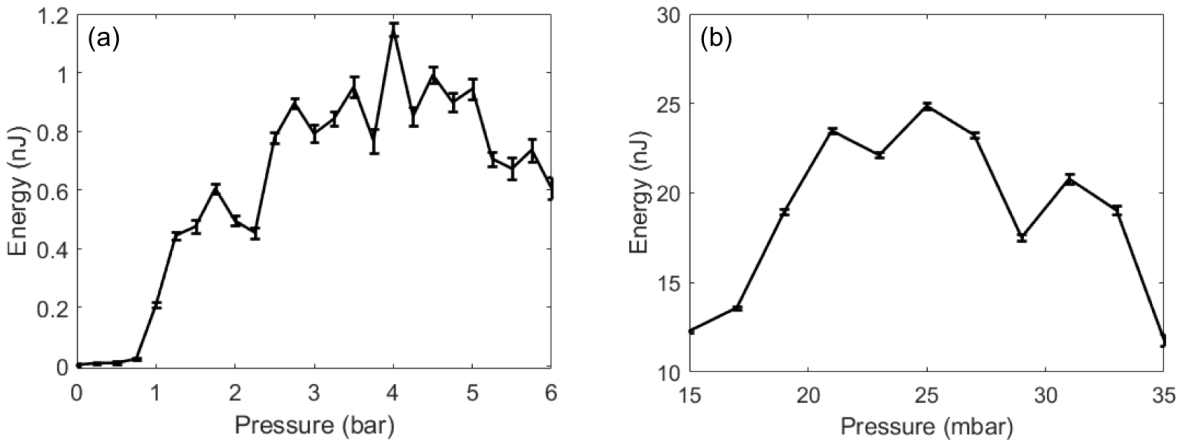

Figure 4.4: Pressure scan for the gas nozzle (a) and gas cell (b) under the 16 m focusing geometry with neon as the generation gas.

for the optimization of this parameter is to close the iris as much as possible without loosing XUV pulse energy. For the example in figure 4.5, this diameter would corresponds to 46 mm, which is close to the values generally used.

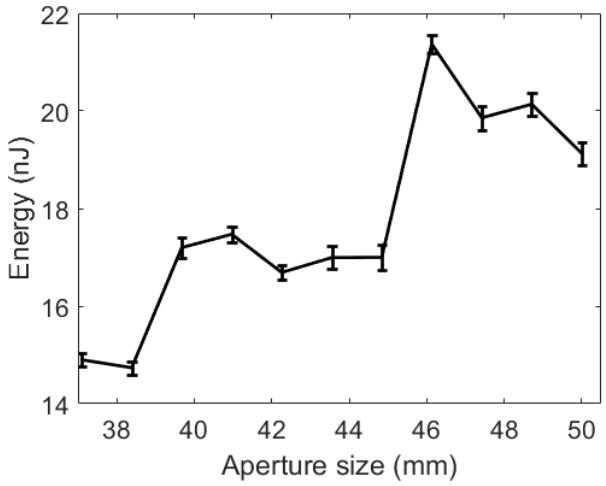

Figure 4.5: Iris scan for the 10 cm gas cell under the 16 m focusing geometry.

Longitudinal focus position

The final parameter to scan is the focus position with respect to the gas medium (z position scan or simply *z-scan*). The target's longitudinal position is kept fixed while the focus is shifted with the adaptive mirror, by slightly changing the beam divergence before the compressor chamber. The general phase-matching model described in chapter 2 shows that there

should be an optimum position before and after the generation medium where the short and long trajectories are respectively phase-matched [100]. In our case the observations are quite different for both the 8 m and 16 m focusing geometries.

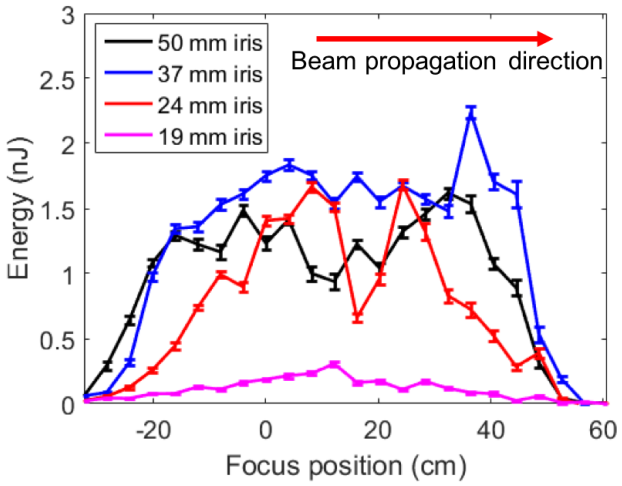

Figure 4.6: Focus position scan for the nozzle with neon, under the 8 m focusing geometry for different iris openings.

Such scans are shown in figure 4.6 for the gas nozzle with neon as the gas medium, under the 8 m focusing geometry. Positive z values mean the focus is positioned further in the beam propagation direction. The 0 cm position corresponds to the approximate nozzle position on that day, which unfortunately was not precisely measured this time (nevertheless from the magenta curve we could expect its position to be around the maximum).

When closing the iris, the energy seems to improve and then decrease again towards 24 mm, but for these big changes in intensities the change in XUV yield is not significant, which we attribute to the effects of the highly ionized medium, as described in section 2.3. The apparent optimum at $z = 40$ cm for the 37 mm corresponds to an outlier. At 19 mm there is still measurable XUV energy, though it is much smaller than the reached optimum.

For the gas nozzle under the 16 m focusing geometry a different behavior is observed (see figure 4.7). In this case, the peak NIR intensity is much closer to the neon BSI intensity, and therefore the effects of ionization should not be so extreme. This is clearly visible in the figure where the XUV yield is clearly smaller at an iris of 45 mm. For an opening of 47.5 the energy seems to be higher for a broader range of focus positions, and the optimum is located slightly before the nozzle position.

Finally the behavior is comparable when scanning the focus position for the 10 cm gas cell (see figure 4.8). The gray shaded area corresponds to the approximate position of the gas cell and therefore the optimum yield occurs when the focus is located in the cell.

The possibility of scanning the driving pulse energy without changing the beam diameter is also discussed in chapter 2. For completeness this was implemented and tested but no significant energy increase was measured.

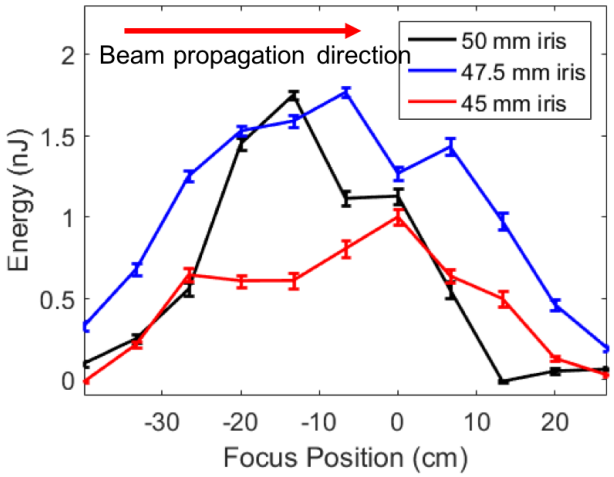

Figure 4.7: Focus position scan for the nozzle with neon, under the 16 m focusing geometry.

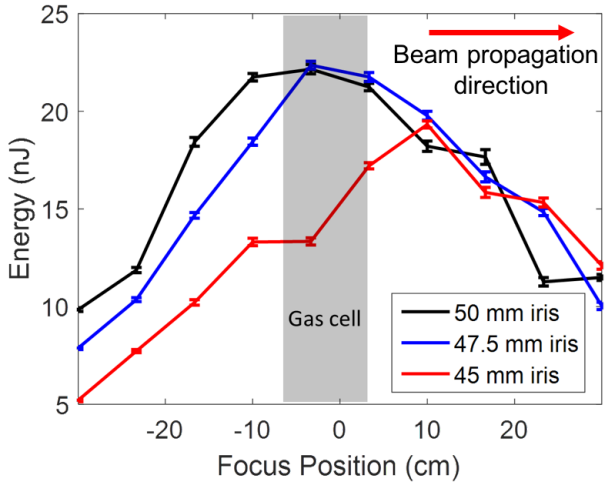

Figure 4.8: Longitudinal focus position scan for the 10 cm cell with neon, under the 16 m focusing geometry.

Optimum achieved XUV energy

Figure 4.9 shows a 40 min long energy measurement with 25 nJ of energy and a 3 nJ standard deviation, where the black line shows the shot-to-shot energy and the red line shows a 99-shot running average. The running average shows fluctuations of up to 10 nJ peak-to-peak, which defines the precision of the optimization procedure, given that in the scans 100 shots are averaged per step. Averaging for longer periods might solve the problem if the long-term stability of the system allowed and if the optimization time was not a constraint. Keeping in mind that the main goal of the system is to try the complex experiments described in the next chapter, reducing the optimization time of the source is an important factor to consider.

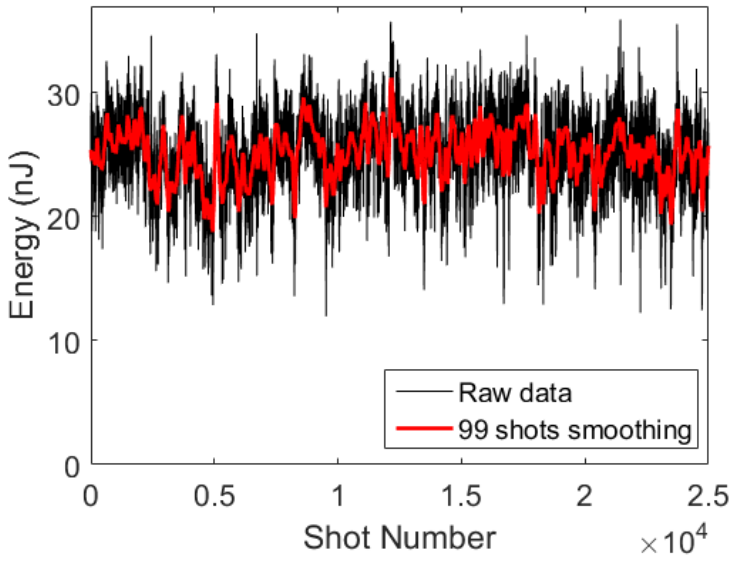

Figure 4.9: 40 min long XUV pulse energy measurement showing the single shots (black line) and a 99-shot running average (red line). The average measured energy after generation and inside the zirconium window is 25 nJ (1.6 × 10^9 photons) with a 3 nJ standard deviation.

With the procedure just described, energies above 20 nJ (above 10^9 photons) are reached on a daily basis, a value that fits what is expected from the energy-scaling scheme (a few tens of nJ, see chapter 2). The procedure described above plus a few extra adjustments regarding the beam profile (see next sections) is therefore good enough in order to carry experiments with the XUV beam. We can therefore conclude that through this optimization procedure the measured yield with the 10 cm cell is in agreement with the what is expected from the energy scaling scheme. However, under these conditions the expected yield dependence on focus position from the established phase-matching theory (see chapter 2) is not in accordance to what is observed. This topic is further discussed in section 4.4.4.

4.2 8 m focal length results

4.2.1 CEP tagged spectra

In section 1.5 the working principle and main results of the phase meter were introduced. Towards the long term goal of experiments with isolated attosecond pulse (IAP), it is necessary to demonstrate the correlation between the measured CEP and the generated HHG spectra. To test this, the well-known CEP-dependent effects on the XUV spectra are measured, namely the harmonic line energy movement, changes of cutoff energy and disappearance of the modulations at the cutoff spectral region [77, 87, 113].

High-harmonics were generated with the nozzle under the 8 m focusing geometry, with neon

as the generation medium. Detailed optimization of the XUV beam was not performed, but the approach was simply to close the iris enough to have a stable beam with distinguishable harmonic lines (opening the iris generated two or more overlapping beams as shown in the next section). Additionally, at the moment the laser cover box was not implemented yet, leading to RMS intensity instabilities above 15% at the NIR focus. This made the measurement particularly challenging given that the mentioned CEP-dependent effects are also intensity-dependent.

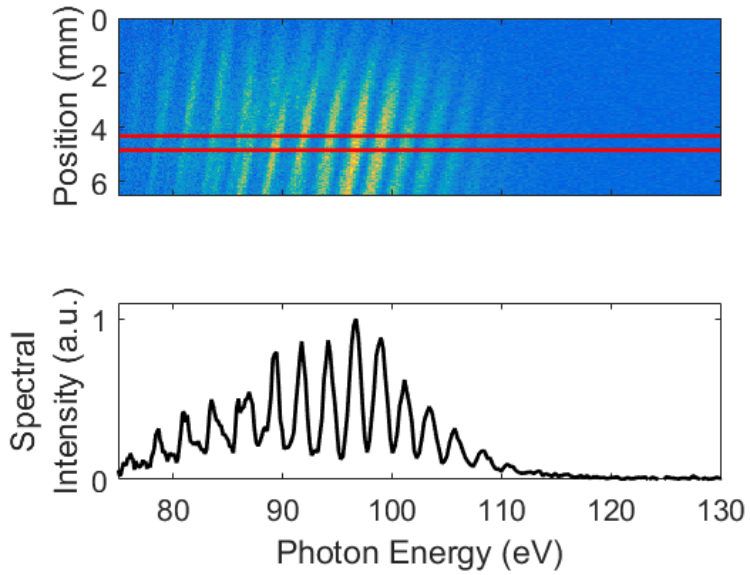

Figure 4.10: (a) Single-shot 2D spectrum used for tagging. (b) Spectrum line-out made by summing the signal over a 10 pixel window centered at 4.58 mm.

1000 shots are measured while synchronously running the phase meter. Figure 4.10 (a) shows a single-shot spectrum from the measured set, while figure 4.10 (b) shows its line-out, calculated by spatially integrating over the window enclosed by the red lines. The selection of a small spatial window is particularly important in this case given the tilting of the spectral lines. This is due to wave-front aberrations, which can be corrected with the adaptive mirror but was not done at the time.

From the CEP data an asymmetry plot is made as explained in section 1.5 (see figure 4.11), which in this case is far below optimum in comparison with the one in figure 1.15. Despite this, from the data a RMS phase error of 0.3 rad can be estimated, which is good enough to see the effects in question, which have a π rad periodicity. Additionally, this value is still comparable to the typical stabilities achieved with CEP stabilization systems (for example, the Femtopower, Spectra-Physics provides < 0.250 rad RMS [82]). Knowing the relative CEP phase of every shot, the spectra line-outs are plotted as a function of CEP (see figure 4.12). The 0 position on the CEP axis is chosen arbitrarily.

Due to the high shot-to-shot fluctuations no clear CEP effects can be seen on the raw data. An RMS error of 48% and 9 eV is measured in the overall counts and cutoff respectively, which

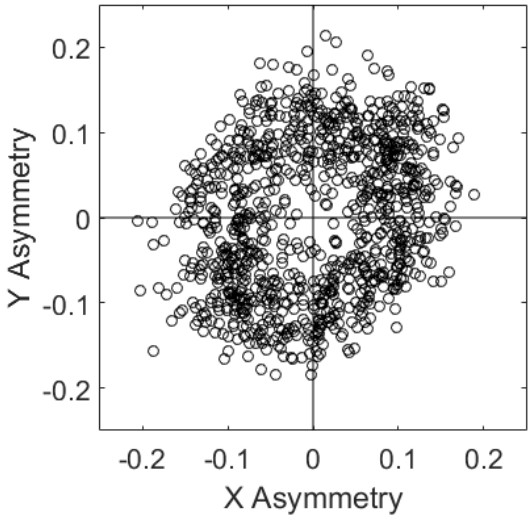

Figure 4.11: Asymmetry plot from where the CEP is extracted in order to tag the measured spectra, with an uncertainty of $\Delta\phi = 0.3$ rad.

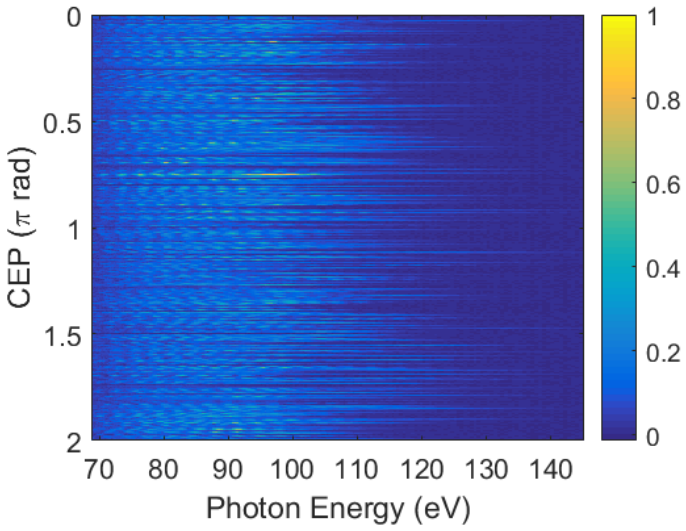

Figure 4.12: Raw single-shot spectrum line-outs ordered by CEP. Due to the high fluctuations no CEP-dependent effects are apparent.

smears out the effects in question (these values are significantly improved later, as shown in section 4.4.2). In order to smooth out these fluctuations a moving filter of 100 shots is applied. Additionally the single shots are corrected for grating efficiency [118], zirconium transmission (see figure 3.15) and camera efficiency drop (see appendix C). The resulting plot is shown in figure 4.13.

After smoothing, two of the expected effects become very clear. First, harmonic line energy

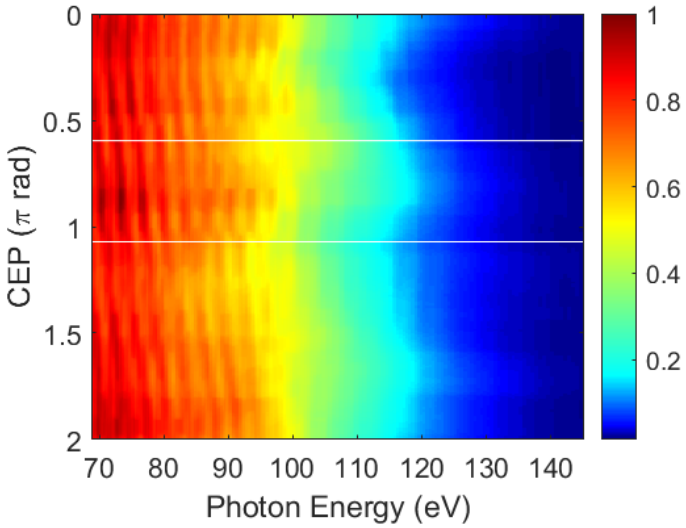

Figure 4.13: Single-shot spectra ordered by CEP after smoothing. The effect of CEP on harmonic line and cutoff energy is clearly visible. The white lines mark the position of the lineouts shown in figure 4.14, at a CEP of 0.6π for the continuous and 1.1π for the modulated spectrum.

changes with CEP are observed in the region below 100 eV, with the expected π-periodicity. Above this photon energy the lines become less clear and a change of yield in the cutoff region is observed, also with a π-periodicity.

However, when observing the spectra in single-shot, both modulations and continua are visible in the cutoff spectral region at all CEPs. Nevertheless, on average it is more probable to observe a continuous spectrum for a CEP of approximatelz 0.6π or 1.6π, as expected. Figures 4.14 (a) and (b) show two raw spectra with modulations and a continuum in its cutoff respectively, for CEPs separated by $\pi/2$ rad.

To better understand the reason for this fluctuation, further investigations should be done (hopefully under optimized laser and HHG conditions, which unfortunately was not possible due to time constraints). A possible explanation for the effect is the intensity-dependent changes on the pulse shape as it propagates through the gas medium. Changes in intensity affect how much self-phase modulation occurs during pulse propagation, influencing the pulse's temporal shape and consequently the generation process (this topic is further discussed in 4.4.4). Additionally, the long distance (approximately 30 m) between the generation medium and the phase-meter might contribute to this effect. Nevertheless, the measurement confirms that it is possible to observe CEP dependent phenomena by using phase-tagging and that most of the shots behave as expected. Consequently the CEP meter can be used to ensure IAPs for the future XUV-pump/XUV-probe experiments.

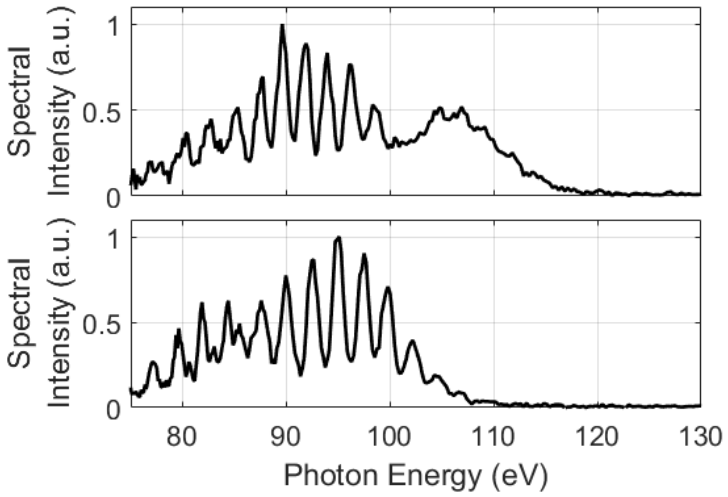

Figure 4.14: Two single-shot line-outs separated by $\pi/2$ rad showing a continuum and modulations at the cutoff spectral region.

4.2.2 Highly ionized regime

As described in section 2.3, for 5 fs driving pulses with intensities above 4.5×10^{15} W/cm^2 the medium is depleted in a sub-cycle time window when using neon as the generation gas [107]. For the 8 m focusing geometry, a peak intensity of 1.1×10^{16} W/cm^2 is reached, which corresponds to this depletion regime. Even though this is a promising approach for broadband IAP generation, to the best of our knowledge, no work has been reported on using such a IAP source for applications. Nevertheless, we tested this approach with the loose-focusing geometry, and the results are summarized in what follows.

When these experiments were done the automated devices for scanning the phase-matching parameters were still not implemented, so the optimization procedure was not applied exactly as described in section 4.1.2. In particular, the integrated counts on the spectrometer were used as a measure of the XUV energy. On one hand, this device has the advantage of providing spectral information in addition to the relative energy changes. However, given the grazing angle used for the grating (84.4°), the effective detection size is less than 2.5 mm in the vertical direction. If during optimization the beam divergence significantly changes, this would be falsely interpreted as an energy change. In addition to this, the laser system was still in development and higher fluctuations in energy and intensity were present, in comparison to what is reported with the 16 m focusing geometry. Regardless of these issues, important conclusion are made under this geometry.

In the previous section it was briefly mentioned that closing the iris improved the beam quality. In this case, a strong dependence of yield as a function of iris diameter is observed (see figure 4.15). At the peak position of 35 mm, an energy of 3-4 nJ is measured with the XUV photodiode. A possible explanation for the decrease in the yield at higher iris openings can be

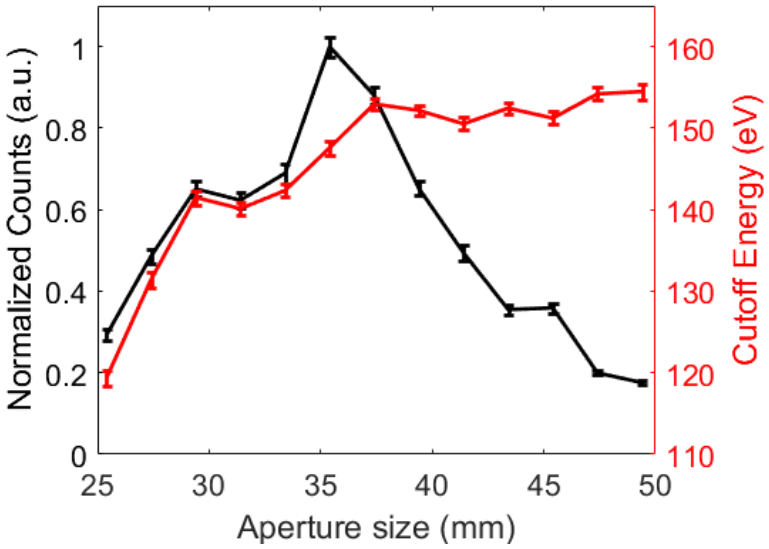

Figure 4.15: Average number of counts integrated over the whole spectrometer CCD area as a function of iris diameter, when using the gas nozzle. The error bars correspond to the standard error at each point. A clear optimum is seen approximately at 35 mm, where an energy of 3-4 nJ is measured with the XUV photodiode.

obtained from the model from Strelkov et al. [95]. There they predict a decrease in generation efficiency when the ionization process changes from tunnel ionization to BSI [95] (though, they predict this to happen at a peak intensity of $I_0 \approx 3 \times I_{BSI}$ and we observe the decrease at $I_0 \approx 6 \times I_{BSI}$).

This effect can also be observed through the changes in cutoff energy as a function of iris opening (see figure 4.15). In order to avoid background problems and the influence of clipping of the higher photon energies at the border of the camera, the cutoff is defined simply as the photon energy at which the signal drops below 20% of the peak. After the 35 mm opening this cutoff energy does not increase significantly with increasing intensity, confirming that harmonics are being generated earlier during the NIR pulse propagation due to ionization gating, as described in chapter 2. Propagation effects are not considered in this analysis, which are expected to be minimized given the short medium length (1.5 mm).

According to figure 3.10 at an iris opening of 35 mm the intensity decreases to approximately half of its peak value, which is still at the depletion intensity regime for neon. Under these conditions, the single-shot spectra shows a very unstable behavior (see for example figures 4.16 (a),(c),(e) and (g)). In these shots it is possible to observe multiple beams, harmonic lines with varying degree of tiling and significant changes from shot to shot.

By integrating over a 10 pixel window as done before, the line-outs are constructed (see figures 4.16 (b),(d),(f), and (h)). For comparison, the same is done for two single-shots at an iris of 25 mm, which are shown in figure 4.17).

For the smaller iris opening, the strong instabilities are not present anymore and the modula-

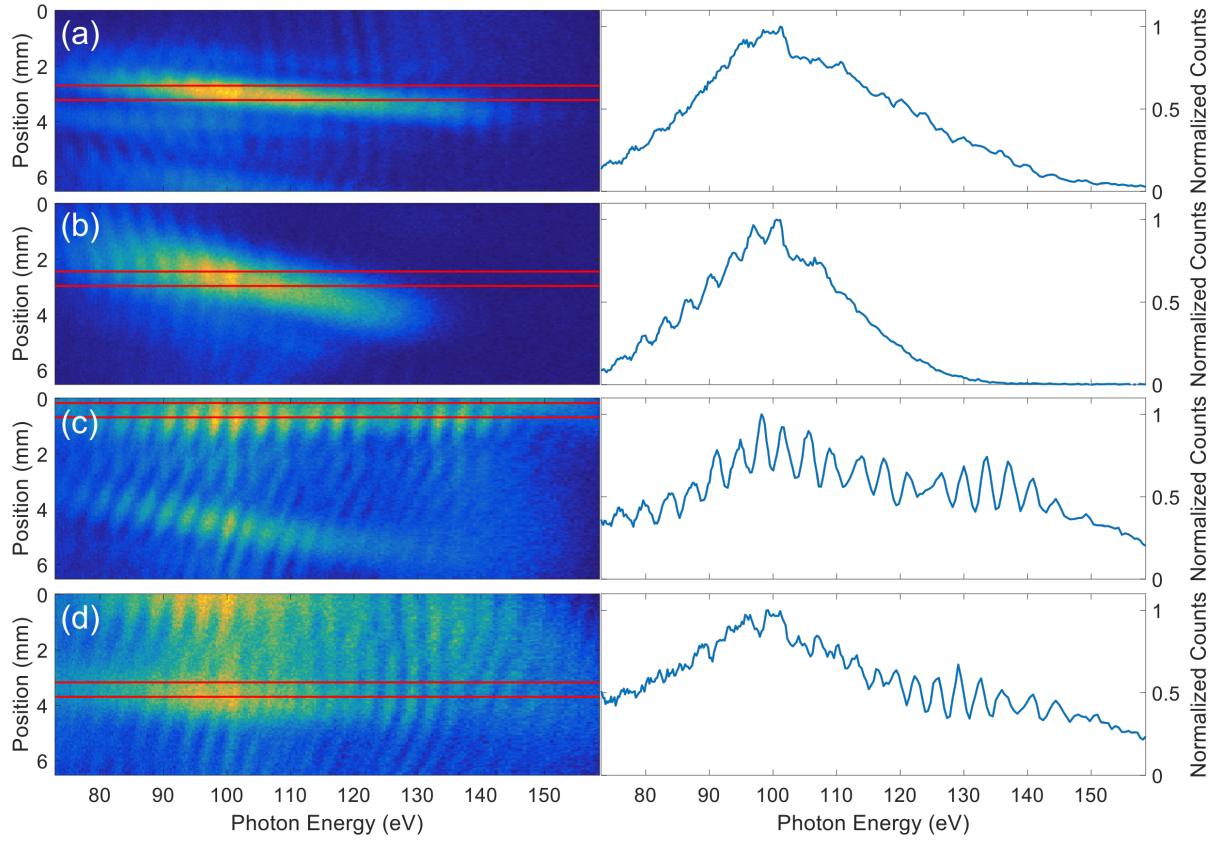

Figure 4.16: Measured single-shot spectra and their respective line-outs generated from the nozzle with neon, at an iris opening of 35 mm. Big instabilities are observed but on some shots a broad continuum is present [(a) and (b)].

tions are clearly visible in the region below 100 eV (equivalent to what is described in section 4.2.1). Therefore we can attribute the instabilities at the 35 mm iris to the strong ionization regime. On the other hand, for this iris opening, the spectrum changes between a broad continua and modulations over the whole measured spectral region, as reported in [107]. Though, the present shot-to-shot fluctuations are too high for reproducible experiments.

A similar behavior is also observed when using the 10 cm cell, though in this case no harmonic lines are observed at all in the cutoff region, regardless of CEP (see figure 4.18). Additional investigations are needed in order to make conclusions regarding this effect, but it might be related to the strong phase modulations experienced by the pulse during propagation in addition to the expected fast depletion of the medium. More details about the pulse propagation are given in section 4.4.4. It worth mentioning that the observation of continua for both cosine and sine pulses is predicted for this depletion regime [95]. The achieved energy with the cell is comparable to the nozzle (only 3-4 nJ), not reaching the expected values from the scaling scheme (see chapter 2).

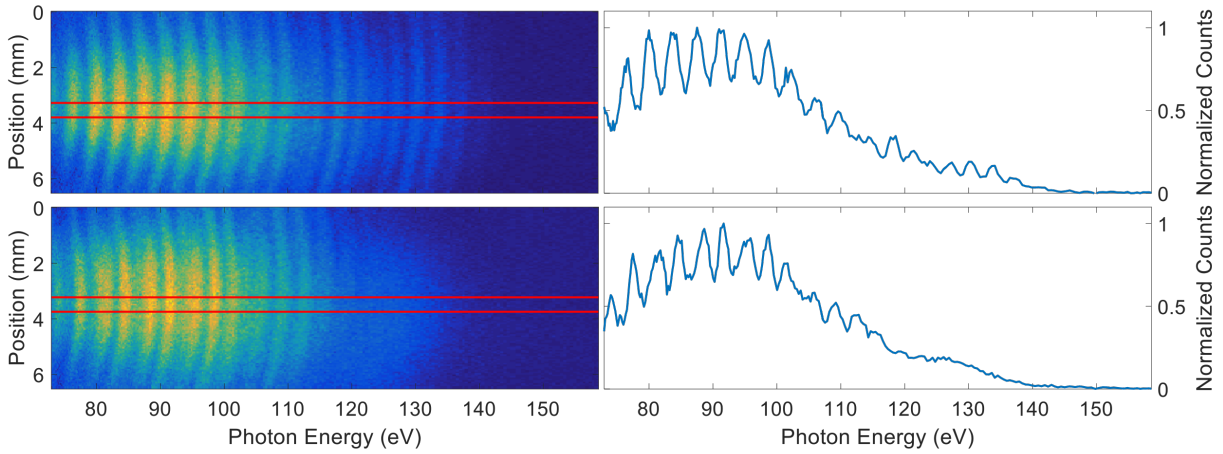

Figure 4.17: Measured single-shot spectra and their respective line-outs generated from the nozzle with neon, at an iris opening of 25 mm. The beam is stable from shot to shot and the cutoff region changes from spectral modulations to a continuum.

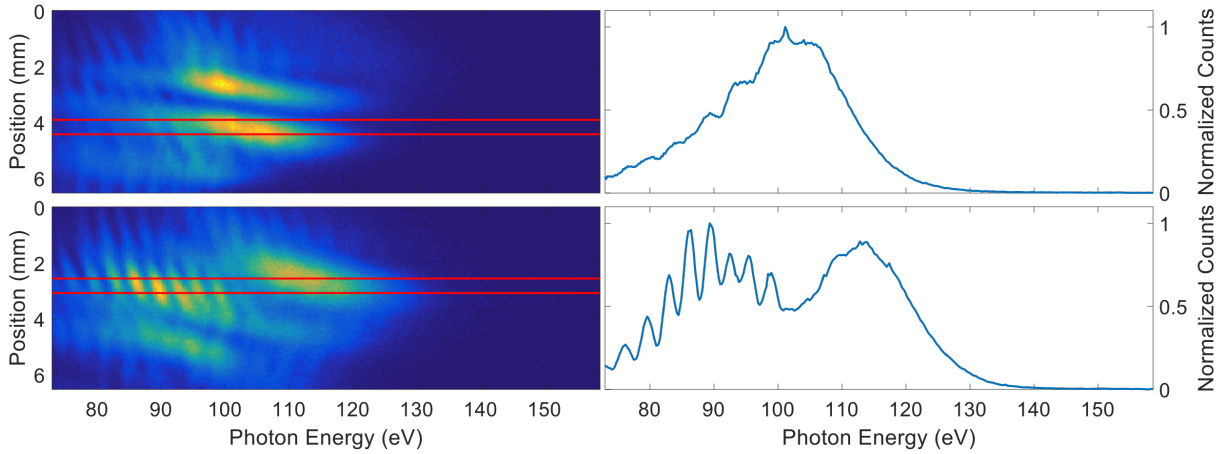

Figure 4.18: Measured single-shot spectra and their respective line-outs generated from the 10 cm cell with neon, at an iris opening of 35 mm. Big instabilities are observed and a continuum is always present at the cutoff region.

To gain additional insight on the observed instabilities, the beam is optimized with the nozzle while using the quality of the XUV profile as the figure of merit instead of maximizing the counts on the spectrometer. By using the two 75% neutral density filters described in section 3.1.2, the iris is closed until a single and stable beam is obtained (see figure 4.19), which occurs at an iris of 27 mm[3]. From figure 3.10 and 3.11, it can be estimated that this corresponds to 4 times less intensity in comparison to the open iris. When the iris is opened to 35 mm, multiple beams are again visible (see figure 4.20), confirming that these instabilities are caused by the

[3]The obtained beam was not round due to wave-front aberrations in the NIR focus, which can be corrected with the adaptive mirror but was not done at the time.

high intensities.

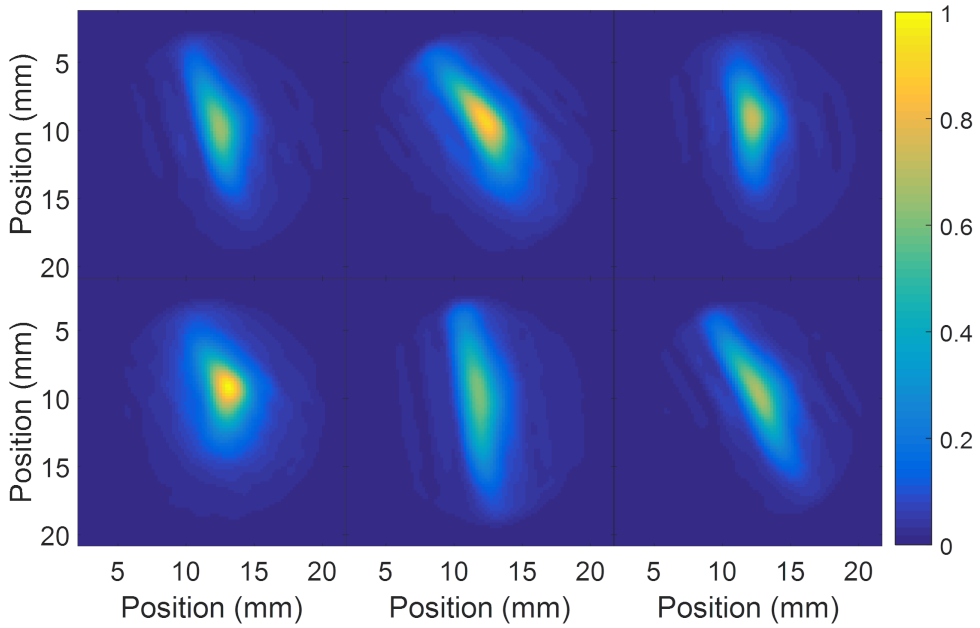

Figure 4.19: Single-shot XUV profiles from the nozzle, with neon as the generating gas, for an iris of 27 mm and two 75% neutral density filters. Even though there are some shot-to-shot fluctuations, there is a single XUV beam.

In conclusion, working in the depletion-intensity regime leads to broad continuum over the whole measured spectral range as reported in [107]. The intensity still needs to be reduced at least a factor of 2 in order to reach optimum yields, and these are still below the expected values from the scaling scheme. Changing the focusing geometry to 11 m approximately might achieve this intensity reduction while using a higher portion of the beam.

In any case, under these conditions, the measured stability does not allow the use of the XUV source for experiments. In order to get a stable beam the intensity needed to be reduced approximately by an order of magnitude. An alternative could be the use of a pinhole after generation in order to spatially filter the beam and achieve a more stable behavior (as done in [107]). However, this approach reduces the available XUV energies, reaching even lower values than the expected from the scaling scheme.

Further exploration can be done with the system under more stable conditions, but for the purpose of maximizing the XUV energy for XUV-pump/XUV-probe experiments, these results clearly point towards using the 16 m focusing geometry for more efficient generation.

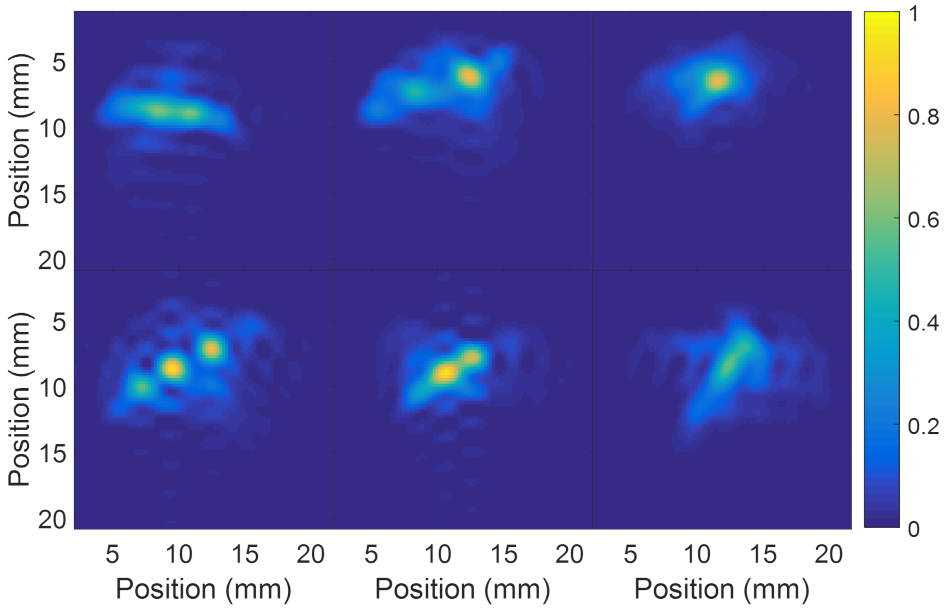

Figure 4.20: Single-shot XUV profiles from the nozzle, with neon as the generating gas, for an iris of 35 mm and two 75% neutral density filters. Fluctuations are clearly visible at the different shots, showing two or even three separate XUV beams.

4.3 16 m focal length results (nozzle)

Under the 16 m focusing geometry the generation conditions differ from what was previously described for the 8 m. Even though for correct energy scaling the generation medium needs to be extended to account for the lower pressures, the use of a short medium provides some advantages. As a starting point for the optimization, aligning a gas nozzle is much easier than the gas cell given that it is possible to directly observe the ionized gas medium and roughly optimize the parameters by using the brightness of the generated plasma as a figure of merit. Additionally, some insight on the generation process can be obtained by observing the properties of the XUV beam coming from this short medium, where propagation effects are minimized.

When using the energy optimization procedure described in section 4.1.2 with the nozzle as the generation medium, energies around a few nJ can be obtained for neon and slightly less for helium. These values are far below from what can be obtained with the gas cells but are high enough to characterize the beam in single shot.

4.3.1 Intensity determination

For short medium lengths, the achievable cutoffs are generally higher, though the overall energy is smaller. This can be explained through the phase-matching theory, where the photon energies with lower coherence lengths do not propagate enough to get out of phase. Ad-

ditionally the NIR beam experiences less propagation effects as described in section 4.4.4. Therefore, the cutoffs obtained with the gas nozzle should be a better estimation of the input laser intensity, whose knowledge is crucial for correctly simulating the generation process. For these investigations the spectra obtained both from neon and helium are used. Using helium gives additional insights on the generation process given that the driving intensity is close to its BSI intensity ($I_{BSI} = 1.5 \times 10^{15}$W/cm^2) and thus ionization is not such an important factor as for neon.

By spatially integrating the XUV spectra obtained from neon and helium, a cutoff of 175 eV and > 195 eV are estimated respectively (see figure 4.21)[4]. The helium cutoff is slightly outside the range of the camera, so only a lower limit can be given. From equation B.2 these cutoffs correspond to intensities of 9.5×10^{14} W/cm^2 and $> 1.1 \times 10^{15}$ W/cm^2 respectively.

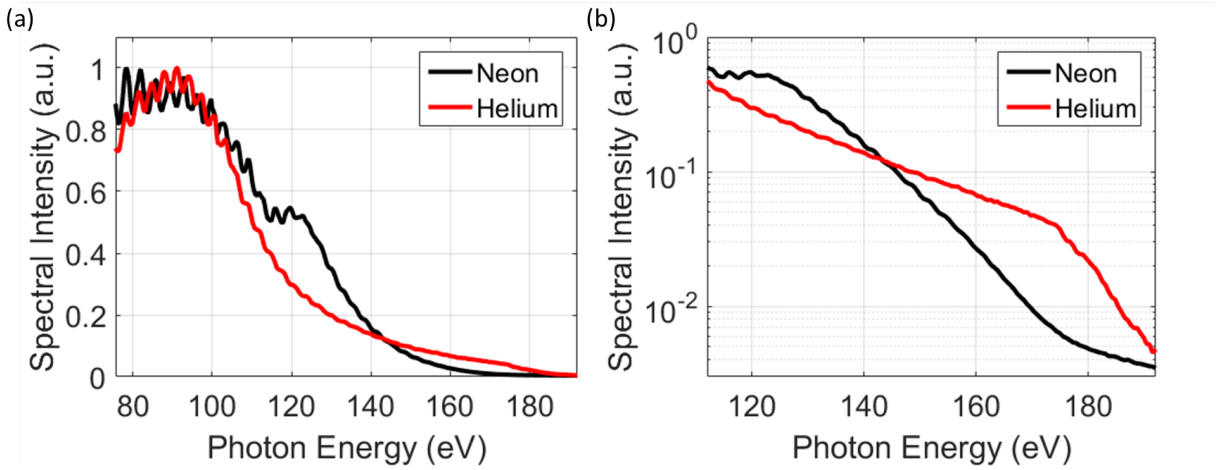

Figure 4.21: (a) Spatially integrated and averaged spectra for neon (black) and helium (red). (b) Same spectra plotted on a semi-logarithmic scale showing a cutoff energy of 175 eV for neon (black) and above 195 eV for helium (red) . The spectral intensities are normalized independently to the peak value and are not on relative scales to each other. The signal drop in the helium spectra at 176 eV is due to the spectral transmission of zirconium (see figure 3.15)

Comparing to the 8 m focusing geometry, in this case the intensity is still above the BSI for neon but below the depletion intensity. This partially explains the difference in the measured cutoff from the neon and helium. Given that the BSI intensity for helium is 1.5×10^{15} W/cm^2, the cutoff position gives a better lower limit estimate on the generation intensity. However, it still differs from the directly measured focus intensity of 3.0×10^{15} W/cm^2, due to the still high level of ionization reached (see chapter 2) in addition to possible uncertainties in the focus characterization.

[4]Experimentally, the exact cut-off position cannot be determined precisely and here it is defined as the approximate photon energy where the signal reaches the noise level (see appendix D).

4.3.2 Spatio-spectral structures

The results presented in this section are slightly off the topic of optimizing the source towards high energies at 100 eV, but they are an interesting effect observed during the optimization process. The effect is still not completely understood and might yield additional insights on the generation process.

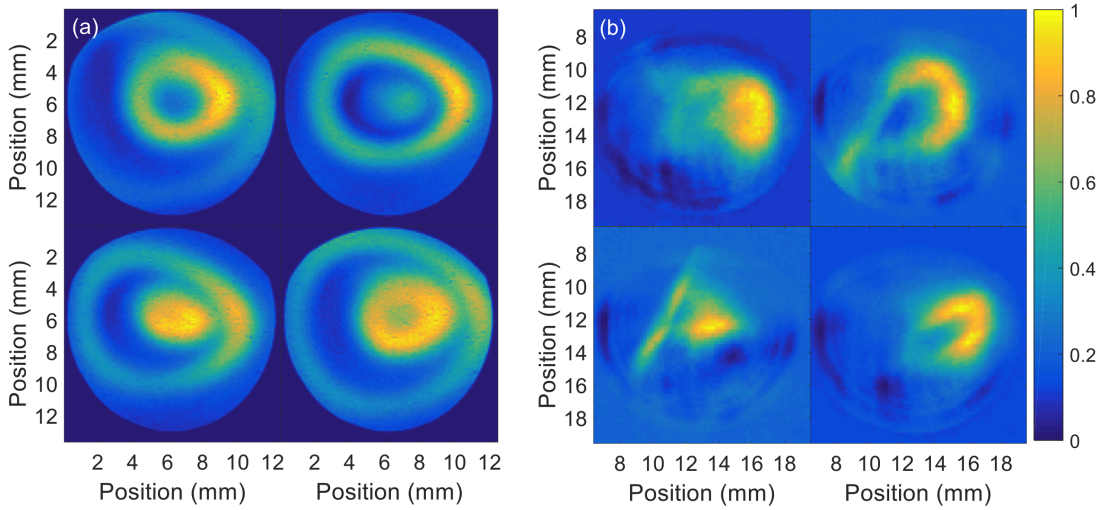

Figure 4.22: Single-shot XUV profile generated from the gas nozzle with neon (a) and helium (b) as the generation gases, when the focus is located at the nozzle's exit. The concentric ring structure changes from shot-to-shot, though in (b) it is barely visible.

Notably, after reducing the intensity through the 16 m focusing mirror, the measured profile with the nozzle is not round and stable as expected, but fluctuates. The profile exhibits a concentric ring structure, whose radii change from shot to shot, but keeps its shape relatively constant (see figure 4.22(a)). This structure is stable and reproducible, with only the size of the structure fluctuating randomly. Therefore these changes are not attributed to instabilities of the system but to other physical mechanism. At the time these experiments started the laser cover was already implemented, providing a peak intensity stability of 4%, as described in the previous chapter.

Qualitatively, a similar behavior is observed for helium, but much less pronounced, suggesting that this might be an intensity dependent behavior (see figure 4.22) (b)). By changing the longitudinal focus position (z) it is possible to change the average size of the structure (see figure 4.23), though the absolute yield changes significantly (see figure 4.7).

Additional information can be obtained from the single-shot spectra (see figure 4.24). As with the profile, the spatial distribution of the radiation changes continuously from completely on axis (figure 4.24 (a)), slightly off-axis (figure 4.24 (b)), mostly off-axis and a second beam appearing on-axis (figure 4.24 (c)), and two beams: one on-axis and one off-axis (figure 4.24 (d)). Even though the XUV spectrometer camera chip is smaller than the profiler chip, the spatially integrated signal is plotted to the right of each spectra for comparison with the profile

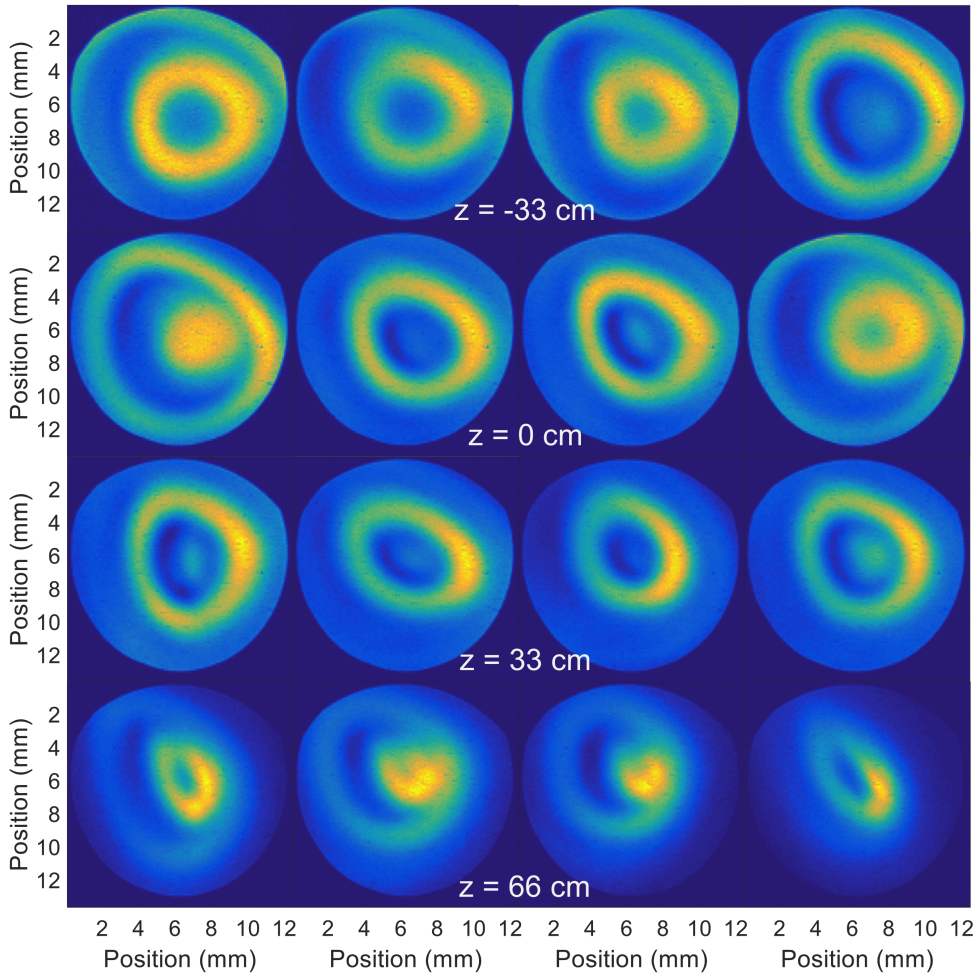

Figure 4.23: Single-shot XUV profiles for different longitudinal focus positions (z). $z = 0$ corresponds to the focus located at the nozzle exit, and positive values correspond to the focus after the nozzle. Profiles are each normalized separately so the absolute yields are not comparable (for a absolute yield comparison see figure 4.7).

images. It is worth mentioning that the broadband continua observed with the 8 m focusing optics is no longer visible in this configuration, confirming that the generation process occurs below the depletion regime.

When the radiation is located on-axis, modulations are present all over the spectrum, but as the beams moves off-axis the modulations disappear at the cut-off region . Additionally, when the radiation is present both on- and off-axis, the modulations disappear only off-axis (see figure 4.24 (d) and its respective lineouts in figure 4.25). Additionally, it can be seen that the effective ring radius is larger for photon energies around 120 eV and gets slightly smaller for energies above or below that.

Similar ring-structures have been reported before and attributed to phase-matching at a critical medium location with respect to the focus [119–121], which is different to what is observed

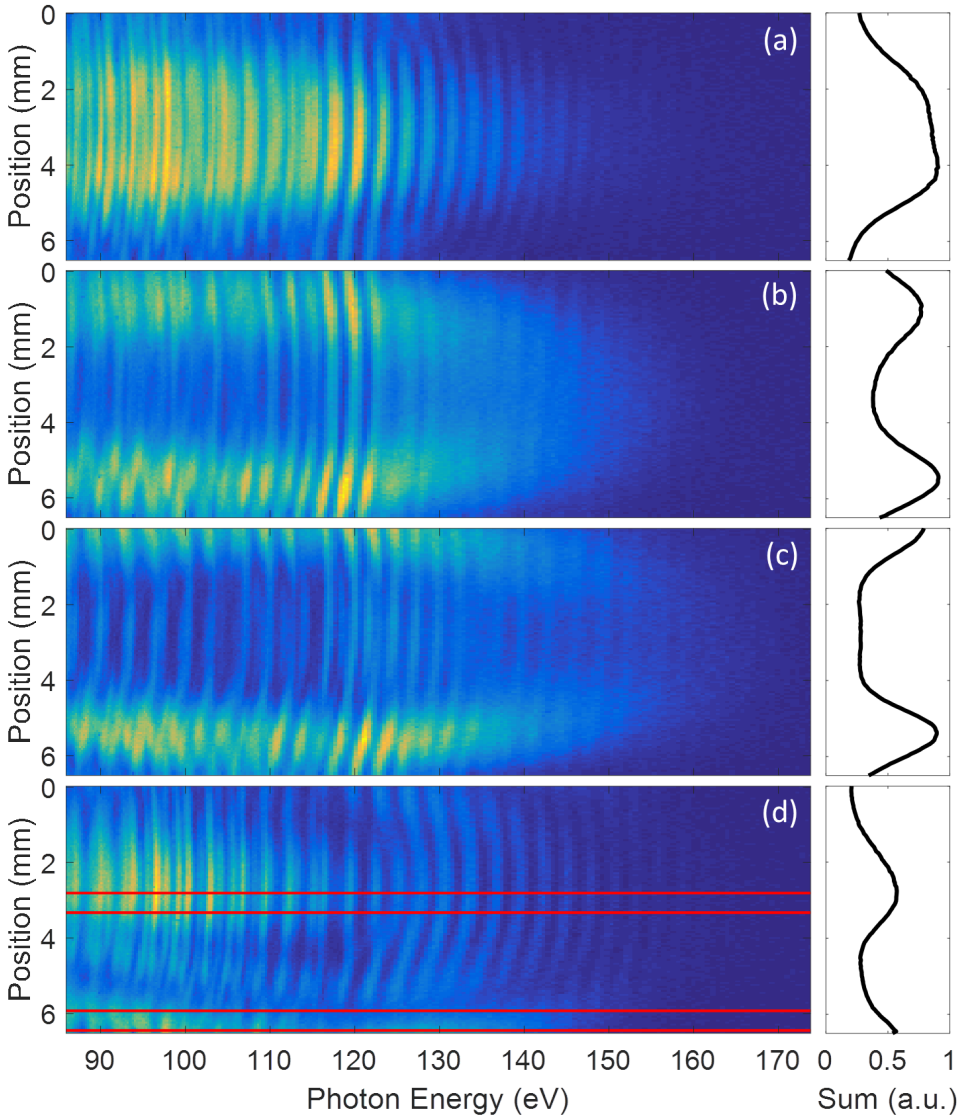

Figure 4.24: Single-shot XUV spectra generated from neon coming from the gas nozzle and its respective spectral integrations, when the focus is located at the nozzle's exit. The spatial distribution of the radiation changes continuously from completely on axis (figure 4.24 (a)), slightly off-axis (figure 4.24 (b)), mostly off-axis and a second beam appearing on-axis (figure 4.24 (c)), and two beams: one on-axis and one off-axis (figure 4.24 (d)). The red lines mark the line-outs for figure 4.25.

here. For these reported cases the radius of the rings depend on the focus position and do not change from shot to shot (this can be claimed because in those cases the ring is visible even if their profile measurement is an average over many shots). To the best of our knowledge, these shot-to-shot variations with the described characteristics have not been reported before. Given that the continuous spectra is observed only off-axis, this effect might be related

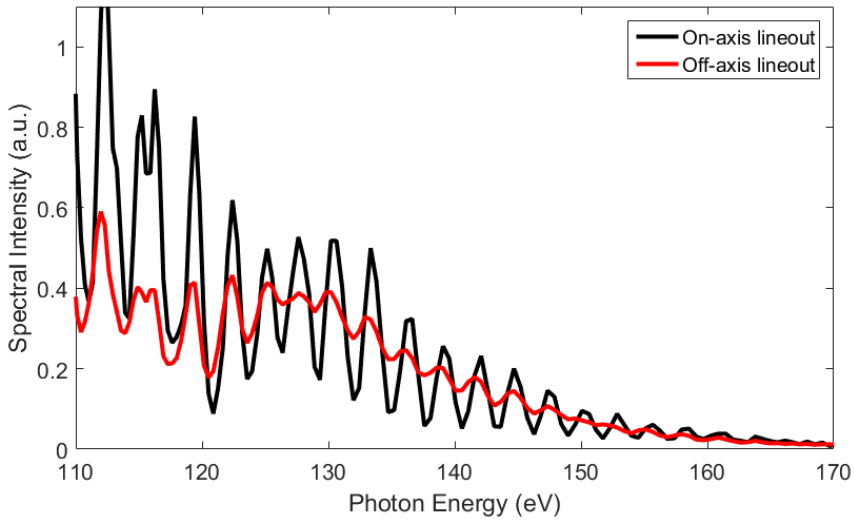

Figure 4.25: Line-outs from figure 4.24 (d), showing the modulation difference between the central portion and the outside of the beam at the cutoff region.

to CEP fluctuation, though changes in intensity or NIR wave-front cannot be discarded as a possible cause.

For further understanding of this effect, simulations similar to the ones described in 4.4.4 are being carried out. It is important to emphasize that these type of observations additionally support the importance of single-shot measurements towards the understanding and control of the HHG process, as stated in [122].

4.4 16m focal length results (cell)

4.4.1 Gas cell length scan

The scaling procedure described in section 2.2 requires the use of long generation media in order to account for the reduction in pressure. To this goal, four different gas cells lengths are tested: 5 cm, 10 cm, 20 cm and 30 cm. Given the importance of the NIR pulse propagation for these long media, part of the interpretation of these results is included in section 4.4.4.

Initially, the 10, 20 and 30 cm cells were optimized on the same day, in that respective order, with approximately one hour difference between them. The optimum values for the 10 cm cell were achieved for an iris of 46 mm and a pressure of 26 mbar. After its optimization, the energy stability was measured for a long period of time (see figure 4.9) in order to have a reference of the fluctuations. This measurement showed an energy of 25 nJ, with an RMS error of 3 nJ. Among the energy changes observed on this long measurement, no significant difference was observed in the pulse energy coming from the 10 and 20 cm cell. The 30 cm cell showed slightly lower energies on average (around 16 nJ), though during the scans it reached

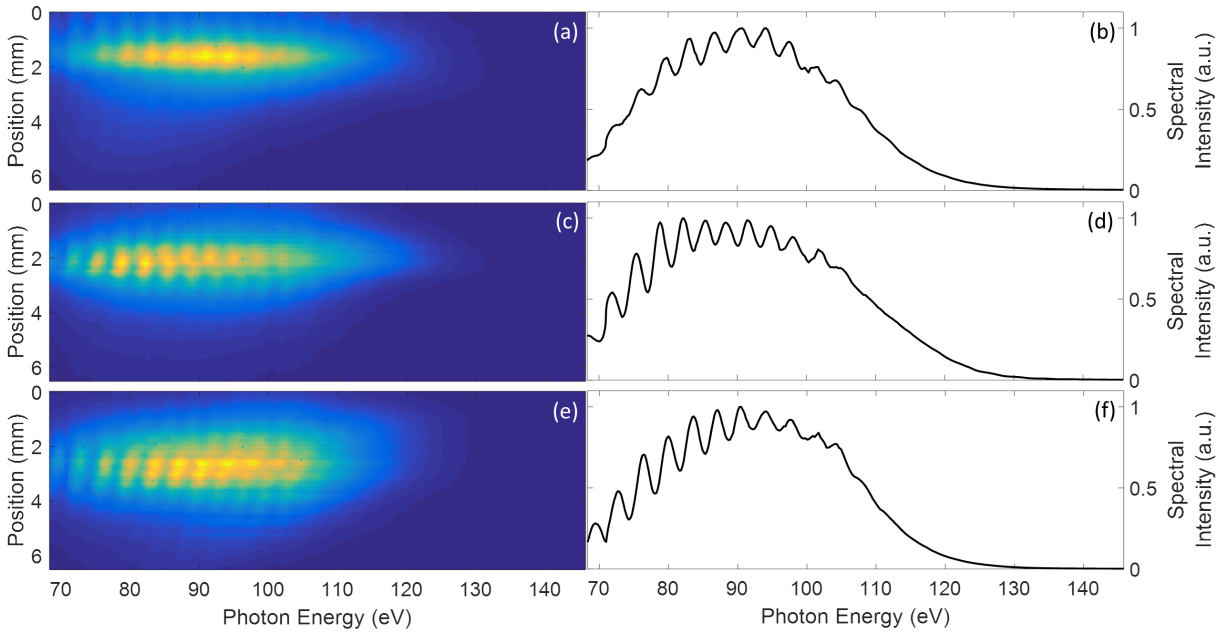

Figure 4.26: Averaged XUV spectra coming from the 10 (a), 20 (c) and 30 (e) cm gas cells, with their respective lineout ((b), (d), (f)). The three of them exhibit a similar shape, with a cutoff at 130 eV approximately. The spectra coming from the 30 cm cell seems to be larger in size, but this is due to decreased pointing stability.

energies above 20 nJ. This energy reduction is attributed to degrading of the laser system, which was not realigned during the measurement.

The same applies to the spectrum and profile. The spectrum showed a cutoff around 130 eV (see figure 4.26), which is the value reached in most of the measurements done in subsequent days (see next section)[5]. The beam profile had an approximate diameter of 1.4 mm FWHM for all thres cells. The RMS pointing stability was approximately 410 μm for the 10 cm cell, and increased for the 20 cm and 30 cm cell to 460 μm and 534 μm respectively (see figure 4.27). The pointing stability is calculated as the RMS differences from the average peak position. In order to account for these pointing fluctuations, each individual measured profile is centered to the average peak position before averaging.

For the long-term goal of time resolved nonlinear optics with the XUV beam a bigger profile is desired, given that in principle it can be focused down to a smaller size, reaching higher intensities. For this goal, the 5 cm cell was separately tested as a generation medium, which is expected to have a lower divergence (this effect is discussed in section 4.4.4).

With this cell it was possible to reach pulse energies up to 18 nJ. The beam profile was approximately 2.9 mm FWHM, which is effectively double the beam size reached with the longer cells (see figure 4.28 (a)). The RMS pointing fluctuation was still comparable to the one from

[5]Even though the spectra are averaged, clear harmonics are visible in the low photon energy range. This is because the line energy change is not linear with CEP in this region [123].

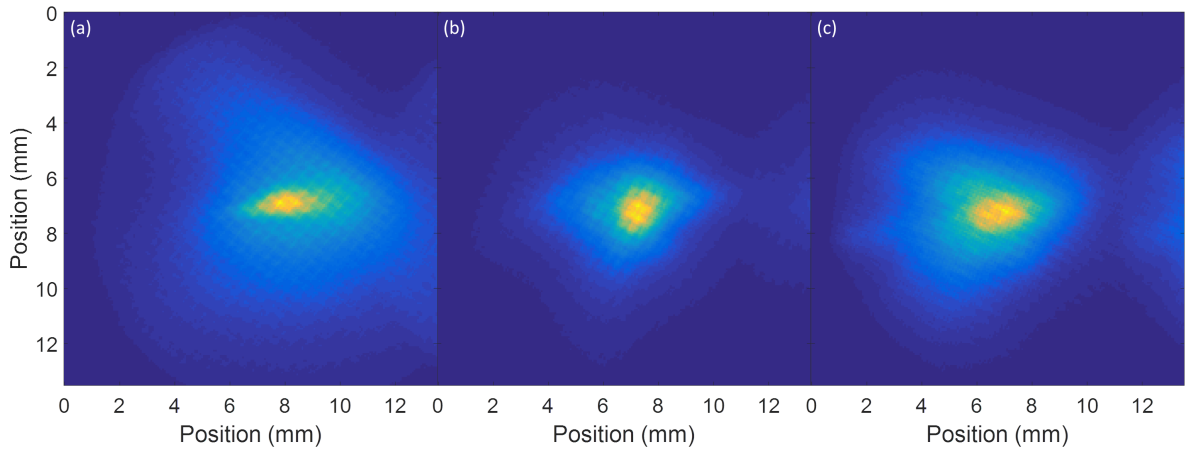

Figure 4.27: Centered and averaged XUV beam profiles coming from the (a) 10 cm, (b) 20 cm and (c) 30 cm gas cells. They have a beam size of 1.43 ± 0.3 mm, 1.40 ± 0.21 mm and 1.45 ± 0.33 mm FWHM, with a pointing stability of 410 μm, 460 μm and 534 μm respectively. Even though the profiles are corrected for pointing, the mesh on the filters is still slightly visible.

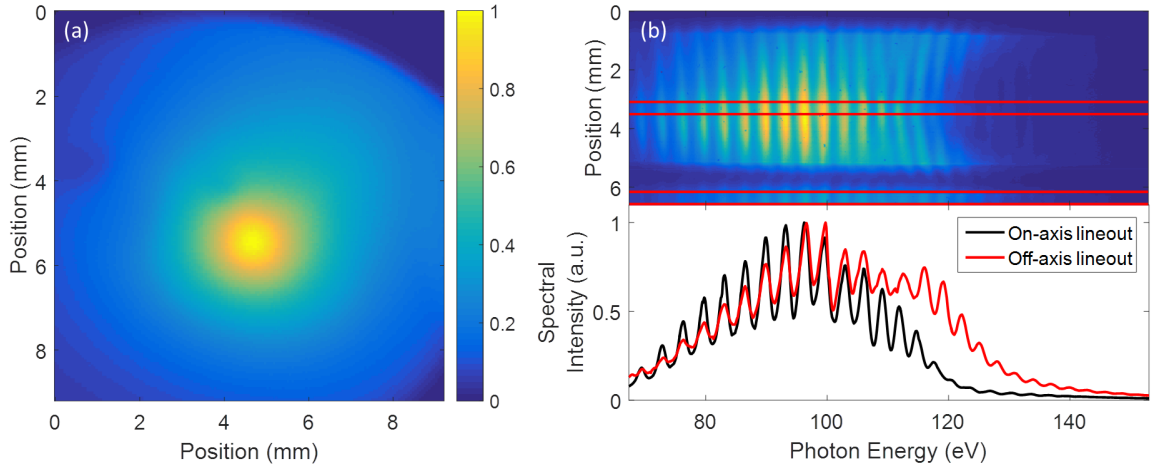

Figure 4.28: (a) Centered and averaged XUV beam profile coming from the 5 cm cell. It has a diameter of 2.9 mm FWHM and a RMS pointing stability of 325 μm. (b) Corresponding averaged XUV spectra and its lineout. On axis, the cutoff energy is approximately 130 eV while off-axis it reaches up to 150 eV. On this day the pulses were approximately 5.4 fs FWHM in duration, which explains the absence of a continuous spectrum at the cutoff region.

the longer cells, with a value of 325 μm. Even though the pulse energy is slightly smaller, the increase in beam size might be better for the pump/probe experiments and it was used on some of the experiments described in the next chapter.

The average spectrum exhibits a different spectral shape at the cutoff region in comparison to the spectrum generated from the optimized 10 cm cell (see figure 4.28 (b)). On axis, the

spectral intensity drops around 130 eV, similar to the 10 cm cell, but there is a small amount of energy extending up to 140 eV. On the other hand, the cut-off is slightly higher off-axis. This structure is stable from shot-to-shot, unlike the structures observed with the nozzle, because the propagation effects are already significant for the 5 cm cell. The clipping on the borders is due to additional devices in the beam path installed for the nonlinear experiments. Additionally, the clear spectral lines at the cutoff region are due to the use of XPW that day (the pulse duration was 5.4 fs FWHM, see section 1.4 for more information).

In conclusion, the 10 and 20 cm cells yielded similar energies around 25 nJ, and slightly less for the 30 cm cell. The beam coming from the three cells had a size of 1.4 mm FWHM approximately on the detector, with increasing pointing fluctuation as the length increased. For this reason, the 10 cm cell was mainly used for further experiments. Additionally, the 5 cm cell provided energies around 18 nJ, with a beam size of 2.9 mm FWHM and a similar pointing stability as the 10 cm cell, which could be focused tighter in order to reach higher intensities.

4.4.2 Optimized parameters for experiments

When having the goal of using the XUV beam for experiments, the 'turn-on' time becomes an important constraint during the optimization procedure. For experiments, the main required conditions are: high-enough XUV pulse energy (18-25 nJ after generation), and a single and stable beam profile. A summary of the source's optimized parameters is provided in table 4.1. Preliminary results with the 10 cm gas cell while using other gases are provided in appendix E.

For optimization, after the GDD scan, the first and most critical parameter to scan is the pressure. Through this scan, an optimum value above 18 nJ should already be reached if the laser is in good conditions (assuming the focus position is already close to the target after the GDD scan). A typical optimum backing pressure reaches a values close to 25 mbar. The iris and focus position can be tuned slightly to improve on the pulse energy. As explained in section 4.1.2, the iris is closed a few mm until just before the energy starts decreasing (see figure 4.5) and the focus longitudinal position is checked in order to make sure it is located close to the cell position.

After this step, the beam profile regularly reaches diameters of approximately 1.1-1.5 mm FWHM and a pointing stability of 300-400 μm (see figure 4.29). On average the beam has a smooth, Gaussian-like profile but additional fluctuations are visible when observing the measured single shots. By additionally closing the iris, the beam profile fluctuations are reduced but the overall XUV energy content decreases as well. These shot-to-shot changes in XUV beam profile are attributed to the above-BSI generation regime, where the generation process is particularly sensitive to wavefront and intensity fluctuations in the driving laser.

Beside the GDD scans, the XUV spectrum is rarely used as a measure for optimization. If the conditions of high pulse energy and stable profile are met, the spectra is usually constant. A cutoff energy of 120-130 eV is regularly achieved with a RMS stability down to 2% (see figure 4.30). Even though the cutoff position is related to the peak intensity (which had a 4% stability) through equation 2.5, its final value depends on the propagation effects in the medium,

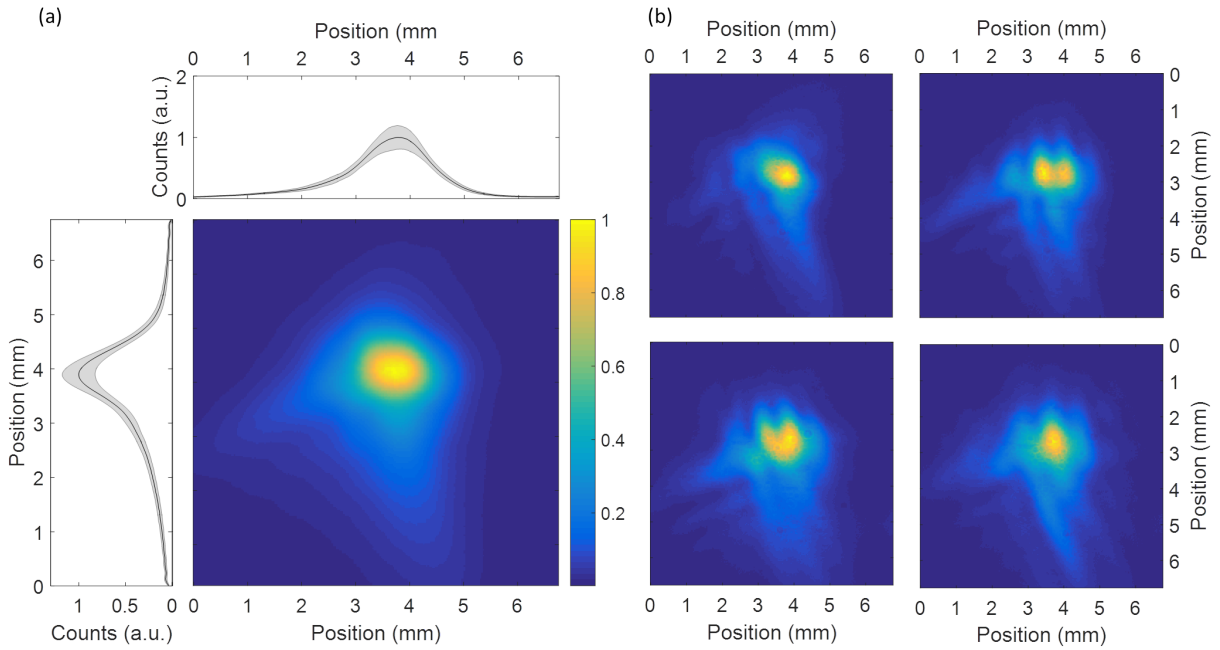

Figure 4.29: (a) Centered and averaged XUV beam profile with its x- and y-axis integration. The shaded region corresponds to the RMS fluctuations. The beam diameter for this case is 1.2 mm FWHM with a pointing stability of 400 μm. b) Single-shot beam profiles qualitatively showing the fluctuation experienced by the beam.

as described in section 4.4.4. After correcting for the zirconium transmission and reported grating efficiency [118], the signal is approximately constant below the region 100 eV, which corresponds to the efficiency plateau region.

When the driving NIR laser is carefully optimized to provide < 5 fs pulses, shot-to-shot changes between continuum and modulations in the cutoff region are clearly visible (see figure 4.31). As explained in chapter 2 this is attributed to random changes in the CEP. A continuum bandwidth between 20-30 eV can be achieved, depending on the driving laser conditions. This effect, in addition to the phase-meter (described in section 1.5) and proper spectral filtering (described in the next chapter) allows the isolation of pulses with attosecond durations. Additionally, odd off-axis harmonics are regularly seen in the single-shot spectra (see figure 4.31 (c) and (d)), which is related to the strong phase modulations experienced by the beam during propagation (as described in section 4.4.4).

During a measurement day, these parameters can be kept for hours. In the first few hours after turning on the system, the gas cell needs to be realigned once or twice due to temperature fluctuations in the room (due to the pump laser). This is easy to monitor using the back reflected focus described in section 3.1.1. After this period, hour-long measurement times are achieved, where the system does not change its working parameters, an essential requirement for the experiments described in the next chapter.

To the best of our knowledge, for a few-cycle driving laser, this source provides the highest

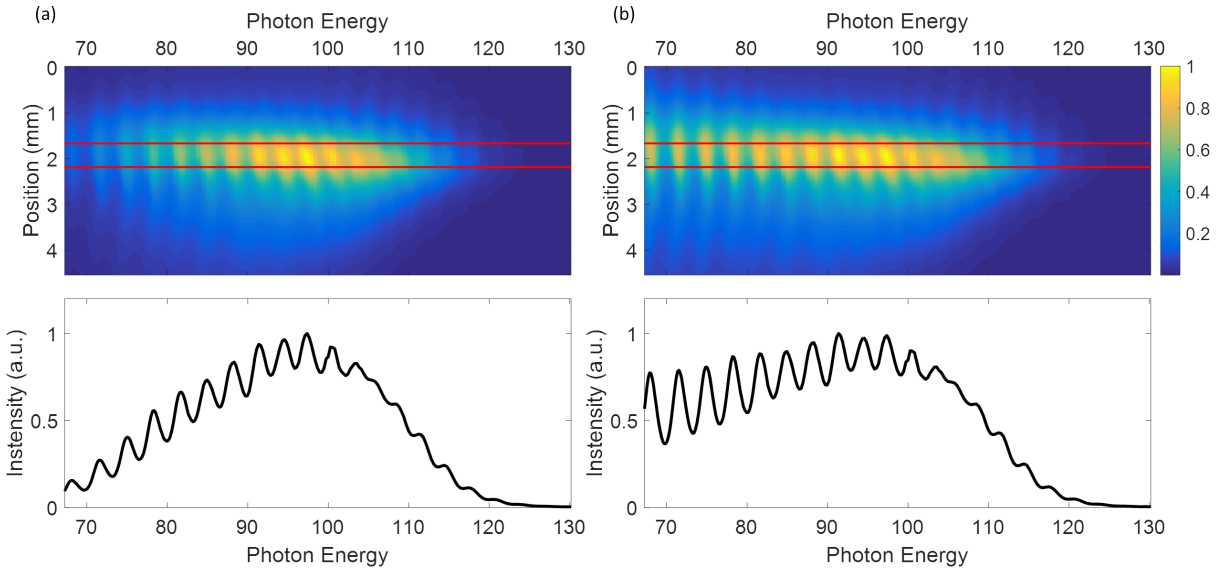

Figure 4.30: (a) Centered and averaged XUV spectra and its respective lineout, showing a cutoff at approximately 130 eV with an RMS stability of 2%. (b) Same spectra and lineout but now corrected for the zirconium transmission and the grating efficiency. A clear harmonic plateau is visible below 100 eV.

XUV pulse energies around 100 eV. From the achieved spectra, it is possible to isolate pulses with attosecond duration through spectral filtering. It is worth mentioning that the highest overall energies reported from a HHG when using neon as the generation gas are of approximately 400 nJ per pulse and a similar spectrum (between 52 and 93 eV) [105]. The source was driven by a 30 fs long driving pulse with an intensity of $I_0 \approx 7 \times 10^{14}$ W/cm^2, which is below the BSI intensity for neon. Even though the reported generation efficiency was higher, a source with these characteristics is not suitable for the generation of IAP without further gating mechanisms. Motivated by these results, using a mirror with a 24 m focal length might allow to increase the energy even more, but at the cost of lower cutoff energy and a narrower continuum.

4.4.3 Intensity tunability

Towards experiments with the XUV source, additional tunability from the optimum operation parameters might be necessary. Particularly, in all demonstrations of two-photon absorption with HHG sources so far, the XUV intensity is scanned by changing the gas backing pressure to show the quadratic dependence of the ion yield [34, 124, 125]. Additionally in the work reported in reference [34], through fine control of the cutoff energy with pressure, they demonstrated that for their experimental conditions the double-ionization of neon occurs mainly through the sequential channel.

Given the complexity of the HHG process, it is challenging to independently control the XUV beam properties. In reference [34] (and probably in the other two as well, though it was not

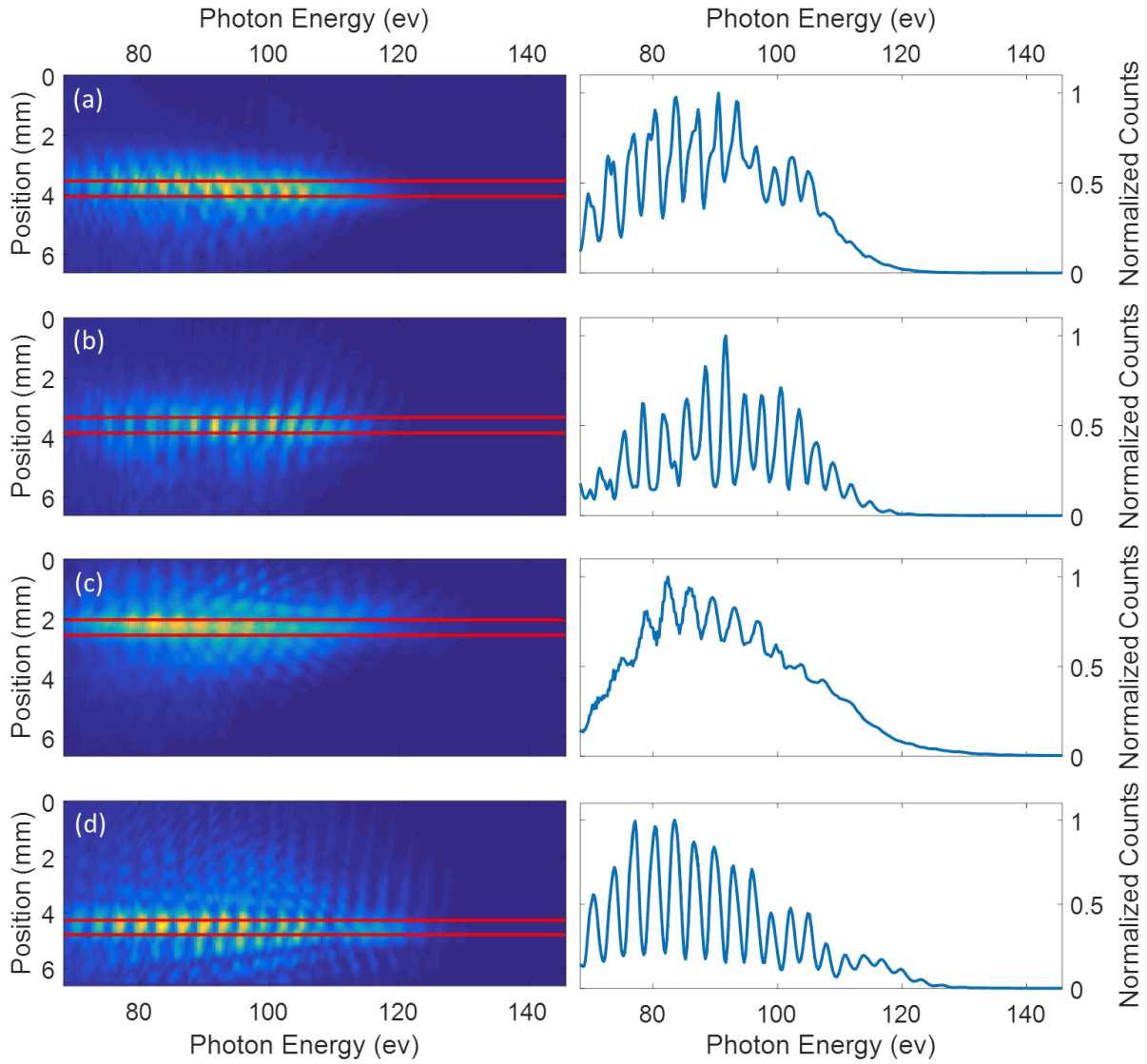

Figure 4.31: Single-shot spectra depicting the different observed properties of the source. Shot (a) and (b) are from the same measurement day and show a continuous and modulated structure at the cutoff region. Shot (c) shows a broad continuum at the cutoff region in addition to odd off-axis harmonics (this shot is presented again in figure 4.35). Shot (d) shows a well modulated structure over the whole spectral region in addition to odd off-axis harmonics.

specified explicitely) the intensity was varied by changing the gas pressure of the generation medium. In all cases, in order to measure the change of *intensity*, an *energy* dependent process was monitored on target, which assumes that changing the pressure does not affect the focused beam properties nor the XUV pulse duration. This could be a source of systematic errors in the measurement.

To test this, the gas pressure is scanned while measuring the XUV spectra. The use of the

Energy (after generation)	18-25 nJ
Energy stability (RMS)	< 10%
Spectral range	70-130 eV
Cutoff stability (RMS)	< 3%
Beam size (FWHM)	1.1 - 1.5 mm
Pointing stability (RMS)	300 - 400 μm

Table 4.1: Summary of XUV source optimized parameters.

spectrometer instead of the profiler allows to measure the effective beam size (in only one dimension) as a function of photon energy. For most of the experiment described in the next chapter, photon energies between 88-98 eV were used, so only that spectral region is considered for the beam diameter determination. The effective energy (determined through the counts at the selected spectral region) and beam size are plotted as a function of pressure (see figure 4.32). Additionally, the normalized fluence (energy divided by beam area) is displayed along the energy curve, in order to show the influence of the varying beam size.

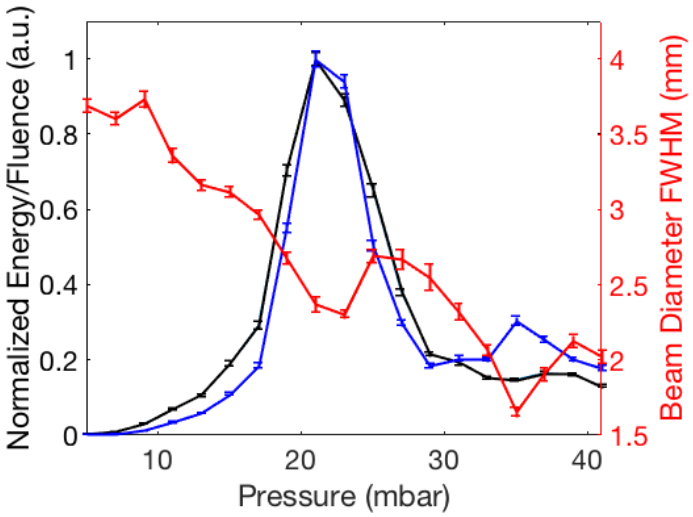

Figure 4.32: Beam energy (black curve), fluence (blue curve) and FWHM size (red curve) as a function of pressure, measured with the XUV spectrometer.

An intensity scan can be carried out by reducing the pressure from approximately 20 mbar to 15 mbar, where the energy is reduced from its peak down to 10% of it. In such a scan, systematic error of up to 40% are observed between the measured energy and the calculated fluence. Furthermore, this analysis does not consider the changes in wavefront, which might

additionally affect the focus quality. The chirp of the XUV pulses is not expected to change with pressure, given that it solely depends on the driving laser intensity [126]. Changing the iris opening or using a second gas cell as an absorption filter might allow additional degrees of freedom, but these approaches need to be tested.

Nevertheless, as explained in the next chapter, the ion microscope setup offers the possibility of measuring ion yields with a spatial resolution smaller than the Rayleigh length of the XUV focus. This is an effective way of controlling the XUV intensity independent on the generation conditions (by shifting the XUV focus along the beam propagation direction) and therefore the pressure-scan approach was not used during experiments.

4.4.4 Comparison with simulations

For a better understanding of the results described until now simulations of the generation process were carried out in the context of a collaboration between the group at MPQ and the Department of Optics and Quantum Electronics at the University of Szeged. The simulations were carried out by B. Major under the supervision of K. Varjú, using a code developed initially by V. Tosa. All of them have participated in the analysis and interpretation of the data, which is still in not finished. In what follow, the simulation data is presented with their authorization.

The calculation of the XUV radiation is divided in two steps: first the laser propagation is calculated in the gas medium, and once the driving field is known all over the grid the XUV radiation is derived. For calculating the driving laser propagation, a three-dimensional nonadiabatic model is used [127], with the Ammosov-Delone-Krainov model for the ionization rates calculation [103]. Then, for the second step of the calculation, the previous solution to the driving laser propagation is used to calculate the single-atom dipole response in the strong field approximation [86].

A 50 mm FWHM, 8th order Gaussian beam is used as the input, with a 45 mm iris placed 12 m before the focusing element, as we have in the experiment. The best results were obtained for a 22.5 m focal length, which is longer than the actual 16 m focusing mirror used in the experiment. This difference is due to uncertainties in the measured beam size and divergence after the adaptive mirror (already such differences are visible, for example, in figure 3.9). Nevertheless the achieved focus of 360 μm FWHM matches the one measured experimentally.

The driving pulse spectrum is set to Gaussian, centered at 800 nm with a corresponding pulse duration of 4.5 fs. For the generation medium a 10 cm long gas cell is used, filled with 6.7 mbar of neon and its end is positioned at focus. The absolute pressure used in the experiment is not exactly known due to the large opening of the gas cell, so after different pressures were simulated it was concluded that this pressure gave the best results.

With these parameters a peak intensity of 1.6×10^{15} W/cm^2 is reached, which is comparable to what we measured for the experiment. However after a few centimeters of propagation inside the gas cell the intensity is reduced, reaching an approximate flat-top profile with a peak value of 8×10^{14} W/cm^2 (see figure 4.33). This behavior is robust to changes in the initial intensity, always reaching a stable value after a few cm of propagation (see figure 4.34). Using equation

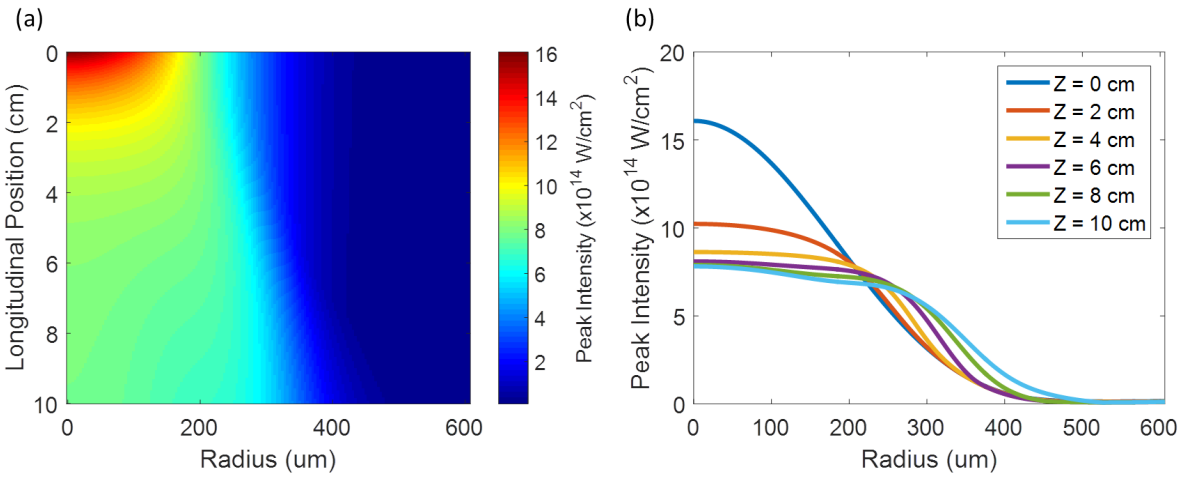

Figure 4.33: (a) Peak intensity spatial distribution inside the gas cell. The peak intensity goes from a Gaussian distribution with a peak value of 1.6×10^{15}W/cm^2, to a flat-top distribution with a value of 8×10^{14}W/cm^2. (b) Intensity lineouts at 6 different positions inside the cell.

2.2, the cutoff for such an intensity would be of 150 eV, so these intensity changes do not completely account for the measured cutoff at 120-130 eV. Additionally, the pulses experience some slight blue-shift and spectral phase modulations, but the pulses do not get longer with propagation. Ideally the simulations should be repeated with the measured spectrum and therefore no additional details are given on this topic.

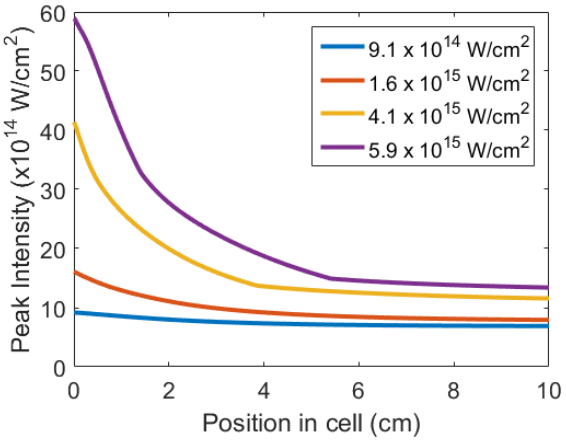

Figure 4.34: Peak intensity as a function of propagation. For all initial values, the intensity decreases with propagation, reaching an asymptotic value after a few cm of propagation.

After the laser propagation, the solution is used to calculate the dipole response, which is then propagated for 12 m in order to calculate the 2-D XUV spectra (see figure 4.35 (a)). The obtained result is in accordance to the one obtained experimentally (see figure 4.35 (b)), although it has a slightly reduced cutoff energy. Off-axis even harmonics are additionally visi-

ble, which were regularly seen in the measured single-shots. For a clear visibility of the odd harmonics, the acquired phase for each photon energy has to be the same at each half-cycle of the laser, therefore we attribute this effect to strong sub-cycle shaping of the electric field during propagation.

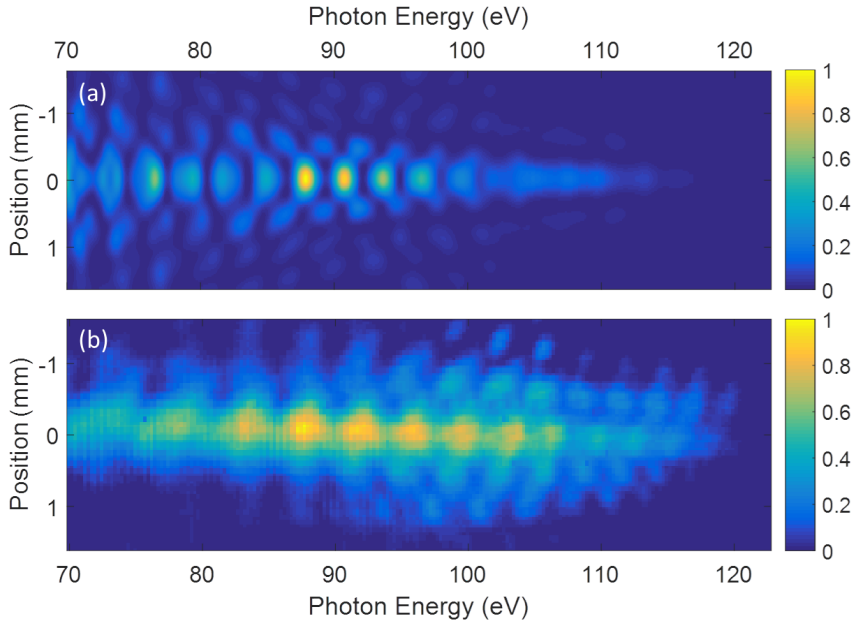

Figure 4.35: (a) Calculated 2-D spectra after 12 m propagation. It has a similar shape as the measured spectra, reproducing approximately the cutoff energy and the observed off-axis even harmonics. (b) Single-shot measured spectrum for comparison with the simulated one.

From the calculated spectrum the obtained beam size is 0.5 mm, which is smaller than the measured one (1.1 mm for the shot shown in figure 4.35 (b)). This has also been reported for a previous use of the same code [128], and is explained through unaccounted wavefront aberrations and the mismatch on the focusing conditions. Nevertheless the agreement between the calculation and the measurement is still acceptable in order to make further conclusions.

Given that the main properties of the simulated emission are in agreement with the experimental results, additional insight can be obtained by analyzing the propagation of the XUV radiation inside the medium (see figure 4.36). In these plots the emitted spectral intensity of four different harmonics is shown as a function of radial and longitudinal position inside the cell. The intensity units are all in the same scale, thus are comparable with each other. For each harmonic, this quantity is related to phase-matching at any particular position: the smaller the phase mismatch, the stronger the generated intensity.

As expected from the measurements, the overall intensities achieved increase with decreasing photon energy, but what can additionally be seen is that higher photon energies are phase-matched earlier in comparison to lower photon energies. By radially integrating the spectral intensity, the overall intensity of each harmonic can be obtained, regardless of where the radiation is generated (see figure 4.37).

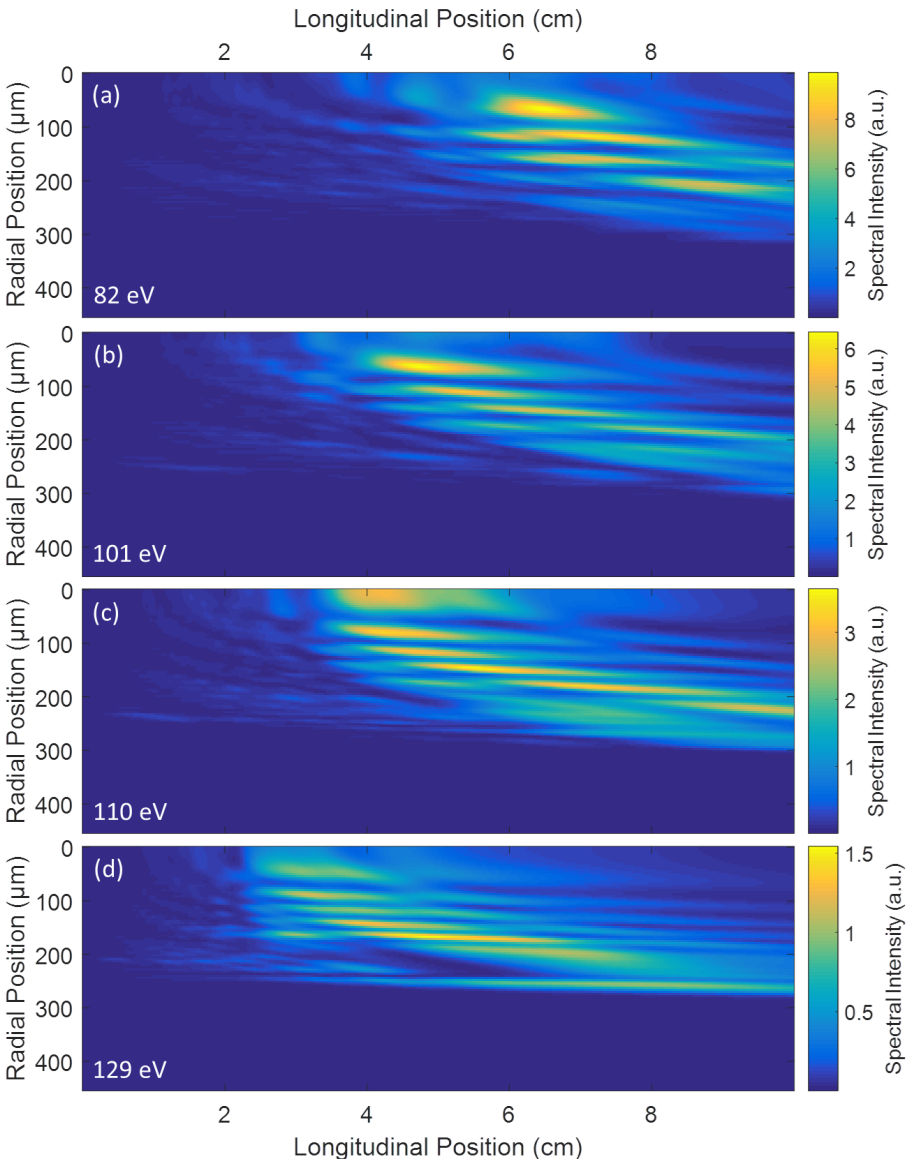

Figure 4.36: Spatial distribution of the emitted spectral intensity inside the gas cell for a photon energy of: (a) 82 eV, (b) 101 eV, (c) 110 eV, and (d) 129 eV.

From this plot we can also conclude that after the peak is reached, the integrated spectral intensity decreases with propagation. These effects explain what is observed with the 5 cm cell, where a higher cutoff and smaller overall energy is reached in comparison to the 10 cm cell. Particularly, for 129 eV, the spectral intensity is reduced at 10 cm in comparison to the intensity at 5 cm, while for 82 eV the opposite observed. This effect is expected to also be present for higher photon energies, but unfortunately such maps were not calculated for photon energies above 129 eV.

Radially, as the pulse propagates, the intensity first starts building up in the center of the beam and later shifts to the sides. When the off-axis intensity builds, at the center it is reduced,

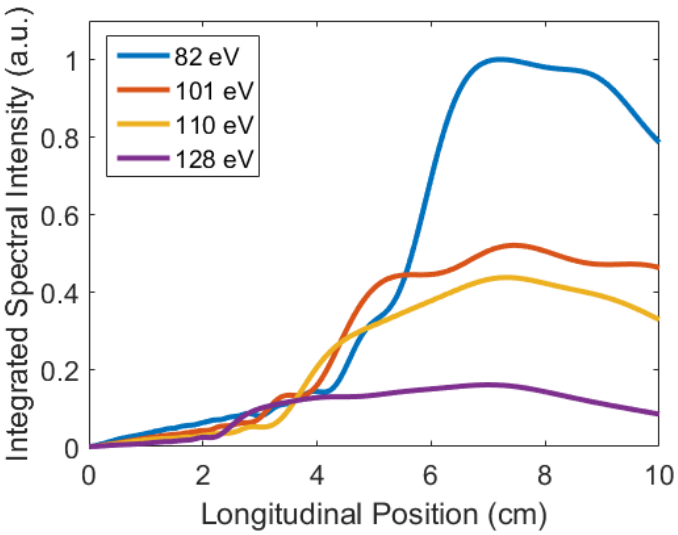

Figure 4.37: Radially integrated spectral intensity for 82, 101, 110 and 129 eV as a function of gas cell longitudinal position.

effectively forming a generation ring. Qualitatively, this ring profile starts occurring when the intensity has reached its stable value. After 5 cm propagation the generation occurs off-axis only for the highest photon energies, while after 7-8 cm of propagation, the generation profile is off-center for the whole spectral range. This effect might be related to the different divergence observed with the 5 cm cell, though the beam profiles after 12 m propagation need to be calculated in order to make further conclusions. Even though after 10 cm the profile is hollow in the center at generation, on the far-field it acquires a Gaussian-like profile, as reported in [128]. Regardless of the driving laser pulse acquiring a flat-top profile, the efficient phase-matching occurs at the borders, depicting the complex dynamics experienced by both the laser and the generated XUV radiation.

An important conclusion obtained from these simulations is the fact that the intensity is reduced by propagation before efficient generation starts taking place. In relation to the model described in chapter 2, the generation process occurs at approximately the BSI intensity and the effects of high-ionization affect mainly the driving pulse properties, before phase-matched generation starts taking place. This means that the harmonics generated at the high input intensities do not reach the detector. This effect might additionally explain why we do not see the expected yield dependence on longitudinal focus position predicted by the phase-matching theory.

This is an important first step towards many possible new investigations. Regarding our measurements, one pending question is the understanding of the high-ionization regime. When starting with an intensity of 6×10^{15} W/cm^2, the value decreases rapidly as shown in figure 4.34. The intensity at which the generation takes place is therefore comparable to the 16 m generation intensity. The different observed behavior in the emitted harmonics can then be attributed to changes experienced by the driving pulse and not only to phase-matching. On

the other hand, we experimentally observe that from a short generation medium, a varying-radius ring structure is observed, which is still under investigation. These and many other questions are the topic of current investigation and hopefully will be answered in the near future.

Chapter summary

- With the automated devices described in the previous chapter, it is possible to scan the phase-matching parameters in a time-efficient manner, reaching an optimum after a few scans.
- By CEP tagging the XUV spectra, three well known CEP-dependent processes were measured, thus confirming it is possible to carry out phase-tagged measurements with the XUV source
- The harmonics generated under the depletion regime with the 8 m focusing mirror exhibit a broad continuum over the spectral region. However the energies and stability reached are not good enough for experiments. This is attributed to the high-ionization regime, concluding longer focal lengths are needed for optimal generation.
- Through the optimization procedure, in addition to a medium length scan, an optimum is found for the 16 m focusing geometry. Energies between 18-25 nJ are regularly achieved, a value expected from the energy-scaling procedure. A continuum is observed at photon energies above 100 eV, which allow the isolation of pulses with attosecond durations through proper spectral filtering. The source's short- and long-term stability allows to use the beam for hour-long measurements.
- The generation process is simulated and the results are in accordance with the measured properties of the beam. These results provide additional understanding of the generation process, where the main conclusion is that phase-matched HHG occurs off-axis after the driving intensity is significantly reduced.

Chapter 5

Nonlinear optics at 100 eV

Through the successful application of the LWS-20 to drive a HHG process in neon, broadband XUV pulses with energies above 20 nJ are achieved, centered at approximately 100 eV. The short driving pulse duration leads to the generation of continuous XUV spectra, which under the proper filtering allows the isolation of pulses with duration in the attosecond range.

To reach the long-term goal of XUV-pump/XUV-probe experiments at this spectral region, a final requirement is needed: a measurable signal generated through the absorption of two (or more) XUV photons. This would first allow to time resolve the photo-absorption process, providing an additional tool to further understand, for example, the dynamics of inner-shell electrons. Additionally, if the right short-lived nonlinearity is found, it would be possible to temporally characterize the XUV pulses in-situ using solely the XUV radiation.

In this chapter the ion-microscope, a device which allows to measure the spatial distribution of XUV-generated ions, is first described. Then, through the imaging capabilities of the device, a value for the XUV intensity can be estimated. As a preliminary experiment, the generation of Xe^{4+} and Xe^{5+} ions through the absorption of two photons is presented. To the best of our knowledge, this constitutes the first time such a measurement is performed at 100 eV with a HHG source.

5.1 The ion microscope

When measuring the ion (or electron) yields generated by intense radiation, the total measured signal is a convolution of both the intensity-dependent yield of the atom or molecule in study and the actual spatial distribution of the radiation. In general, the spatial distribution of the intensity is not easy to measure for shorter wavelengths. Furthermore, even if it is known, other effects such as saturation through depletion of the ionization state would lead to an inaccurate interpretation of the yield data.

For example, the generation of ions through the absorption of two XUV photons coming from HHG sources has been achieved at photon energies up to 50 eV approximately [34, 124, 125]. To prove these ions are generated through two-photon absorption, it is necessary to show that the total yield depends quadratically on the intensity. For this purpose, the HHG-gas pressure was changed in order to change the XUV pulse energy. As mentioned in section 4.4.3, this might additionally affect the XUV focus properties and pulse duration in an uncontrolled way.

For the purpose of overcoming these issues, an ion microscope can be used; it allows to measure the absolute yield and spatial distribution of the generated ions. Developed previously in collaboration with Stephan Käsdorf [129], it was initially used to measure the distribution of IR-generated ions [130] and later to characterize the XUV focus of the FLASH free-electron laser [131]. Its use with HHG sources was later demonstrated first by measuring of single photon ionization [132], and finally by detecting He^+ generated via two-photon absorption [133].

In reference [132] new insights were obtained in the intensity dependent atomic phase during the generation process thanks to the spatial resolution of the interference patterns at focus. Later in reference [133] the actual spatial intensity distribution was used to show the quadratically dependent yield of the ion signal, overcoming the previously mentioned difficulty. Even though these experiments were carried at lower photon energies in comparison to our source, they prove the applicability of the ion microscope for the purpose of this work.

In what follows the main working conditions of the ion microscope used in the experiments are be described. A detailed report on the characterization of the device by using both IR- and XUV-generated ions can be found in reference [134].

The microscope, through electrostatic lenses, generates a magnified image of the ion distribution of the observed region on a detector (see figure 5.1). In order to minimize the interaction between the electrostatic elements, all apertures between them are grounded allowing the independent control of each element's voltage. The whole setup is additionally surrounded by a grounded metal tube in order to minimize the influence of external fields.

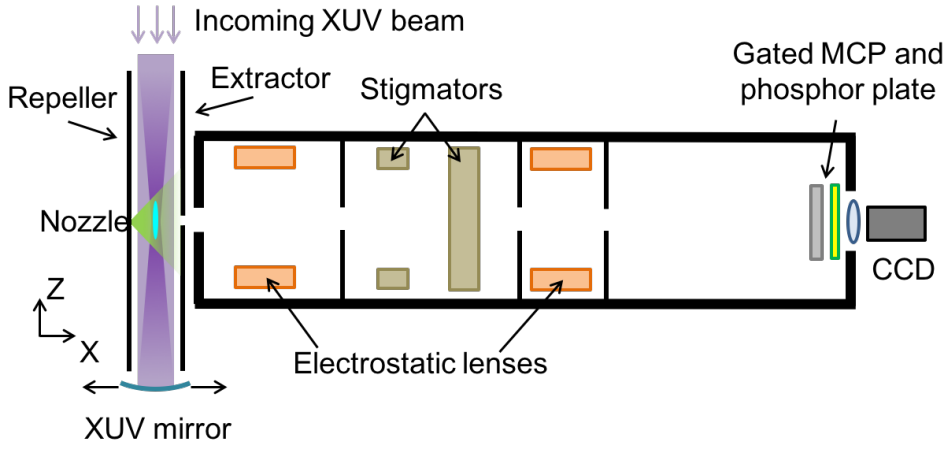

Figure 5.1: Schematic of the ion microscope setup. The XUV radiation ionizes the gas of interest, which is introduced into the observation region through a nozzle or as background gas. The ions travel in the X direction accelerated by the repeller and extractor plates. The electrostatic lenses generate a magnified image of the ion distribution on the MCP detector, which generates a signal on the phosphor screen. The signal is finally recorded with a CCD.

The device's observation region is located in the experimental chamber, before the spectrometer (see figure 3.16). This region is floated with neutral gas (or gas is delivered through a nozzle, as explained later), which is then ionized by the XUV radiation. The interaction be-

tween the XUV and the atoms occur between a pair of positively charged repeller and extractor plates. The plates are separated by 11 mm distance and their voltage is set to 18 kV and 16 kV respectively. There is a 0.5 mm hole on the extractor, through which the ions leave the interaction region and go towards the detector. This hole defines the field of view of the ion microscope.

After leaving the interaction region, a first electrostatic lens focuses the ions at an intermediate point before reaching the detector. A pair of oppositely charged parallel plates, named the stigmator plates, allow to both change the direction of the ion beam and compensate for aberrations. They can be adjusted separately within a range of ±1 kV.

A second electrostatic lens finally images the intermediate image onto a MCP and phosphor screen assembly. Each ion generates an electron signal on the MCP which is then turned into photons at the phosphor screen, which are finally measured with a CCD camera. Under typical working conditions, the imaging system has a magnification of 0.82 μm/px. However, the resolution is limited by the spot generated by the MCP on the phosphor screen in response to a single ion, which has a diameter of approximately 5.7 μm [134].

In addition to the high-voltage controllers, a delay box is used to trigger the MCP between its 'on' and 'off' state. The gating pulse duration can be adjusted in order to control the temporal resolution of the measurement, with a minimum value of 6 ± 1 ns FWHM. In addition, the gate position can be changed in steps of 0.1 ns, allowing to use the microscope as a TOF mass spectrometer. Ions with different mass to charge ratios (m/q) will have different arrival times, which can be selected by changing the gate delay.

When floating the interaction region with the gas of interest, the working pressure is limited to 10^{-3} mbar. Even though the MCP chamber is differentially pumped, further increasing the pressure leads to an MCP chamber pressure of 10^{-5} mbar, which is on the limit before generating a discharge between the channels. In general it is advantageous to increase the ion-yield signal, for which increasing the pressure at the interaction region is necessary. For this purpose, a nozzle located in the repeller plate can provide a gas density increase in the interaction region of approximately one order of magnitude (see figure 5.1). More details are described in reference [134].

5.2 XUV focus characterization

In order to focus the XUV radiation into the field of view of the ion microscope, a 1" diameter home-made XUV multilayer mirrors is mounted at a normal incidence angle with respect to the beam propagation[1]. Two different mirrors are used for the experiment, both having a 12.5 cm focal length. The reflectivity of each mirror peaks at 93 eV and 115 eV, with a respective FWHM bandwidth of 10 eV and 11 eV (see figure 5.2). In the following sections these mirrors are referred according to their central reflectivity peak.

The incoming beam has a much broader spectrum and higher energy content in comparison with the reflected beam, which in this geometry creates an additional source of background

[1] The mirror design and production was realized by Dr. Alexander Guggenmos [90].

signal. Because the observation region is much smaller than the incoming beam, this background is homogeneously distributed over the whole microscope's field of view. Due to the microscopes imaging capabilities, the relevant focus region can be spatially filtered, reducing the background signal significantly. This allows the detection of very weak signals, as shown in the next section.

The choice of mirrors is motivated by the previous work done at synchrotron and FEL facilities at these photon energies, as described in the introduction. Of particular importance is the giant 4d resonance of xenon [38, 39], which has been studied through multi-photon absorption with 93 eV radiation [43, 44], with a time-resolution of only 10's of femtoseconds. The 115 eV mirror allow to filter out the lower photon energies in order to isolated pulses with attosecond durations.

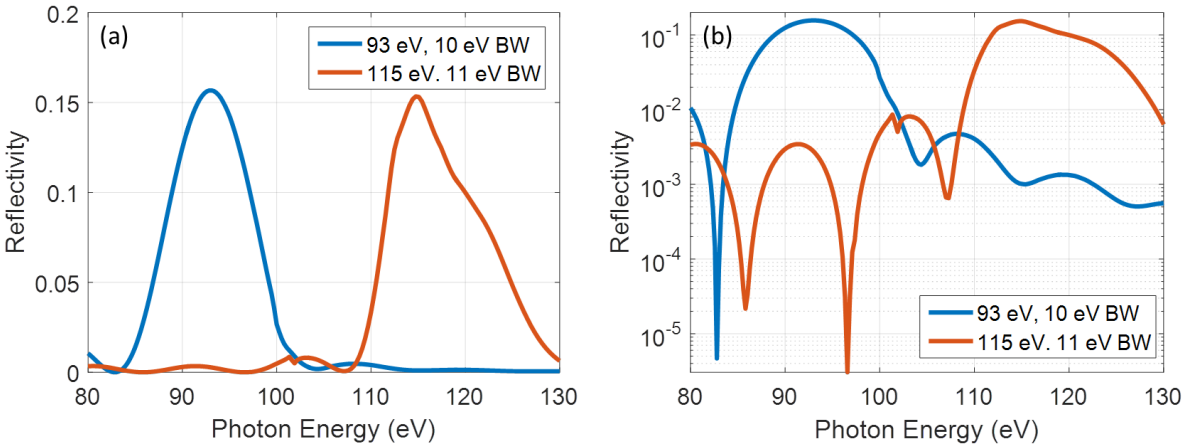

Figure 5.2: (a) XUV mirror reflectivity as a function of photon energies for the 93 eV (blue) and 115 eV (orange) mirrors, with a FWHM of 10 eV and 11 eV, respectively. (b) XUV mirror reflectivity as a function of photon energies plotted in a semi-logarithmic scale.

The mirror holder is mounted on a motorized XYZ stage. The X-axis range is long enough to position and remove the mirror from the beam path between the microscope and the XUV spectrometer (see figure 3.16). Additionally the other two axes serve to align the focus position into the field-of-view of the microscope. The Y- and Z-axis ranges allow to move the focus position in steps significantly smaller than the field-of-view of the microscope. As it is shown in section 5.3, the Z-axis range is longer than the XUV focus Rayleigh length, thus scanning this axis while measuring a two-photon signal corresponds to an intensity scan that keeps the HHG properties constant.

Assuming an ideal Gaussian beam, the FWHM focus diameter can be estimated by:

$$2w_0 = \frac{2\ln(2)\,\lambda}{\pi}\left(\frac{F}{D}\right), \tag{5.1}$$

where λ is the wavelength of the radiation, F is the focal length of the focusing optic and D is the the FWHM beam diameter at the focusing optic. For a central wavelength of 13 nm (93

eV), a focal length of 125 mm and a beam size of 1.2 mm FWHM at the mirror, the diffraction limited FWHM focus is determined to be 0.6 μm. This value is smaller than the effective resolution of the microscope but an upper limit to the focus size can still be be obtained with the device.

With the 5 cm gas cell, a beam with approximately double the diameter is obtained, as explained in section 4.4.1. Ideally this would mean half the focus size, which increases the peak intensity if no other aberrations are dominant when focusing, though this has not been demonstrated yet.

For the focus characterization, the 93 eV mirror is used and the microscope is floated with xenon gas. Additionally, one of the zirconium filters is removed in order to maximize the energy on target. Even though a small portion of NIR radiation goes through when using only one filter, this is not enough to generate any signal on the microscope. This is tested by running the system without the HHG gas medium. It is possible to generate up to three-times ionized xenon with a single 93 eV photon (see figure 5.3). The right delay for the gating window is determined by recording a TOF spectrum and identifying the different species through their relative delays (for more details on this procedure, see reference [134]). In this case, the MCP gate width is set to 2500 ns, which is long enough to include the delays for Xe^{1+}, Xe^{2+} and Xe^{3+}.

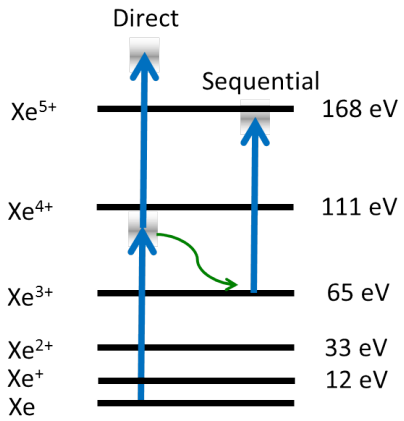

Figure 5.3: Representation of the energy necessary to generate the different ionization states of xenon. With a single photon coming from the 93 eV mirror up to Xe^{3+} can be generated (the blue arrow represent a 93 eV photon and the bandwidth is represented by the gray shaded area). Both Xe^{4+} and Xe^{5+} can be generated from a direct (left) or sequential (right) channel, though the sequential channel is expected to be minimized for Xe^{5+} with 93 eV photons.

When averaging over many shots, changes in the focus position due to pointing effectively increases the measured beam size. Measuring in single shot would allow to eliminate this effect, however, for the configuration used in the following example, the signal generated in a single shot is not enough to accurately determine the focus size. For this reason, the camera is set to acquire 159 images with a 10 s integration time each (corresponding to 100 shots per image). For each image, a line-out is made over a window of 20 pixels and the diameter is

determined by fitting a Gaussian curve to it (see figure 5.4). With this, a FWHM diameter of 6.5 ± 0.082 μm (standard error) is measured [2].

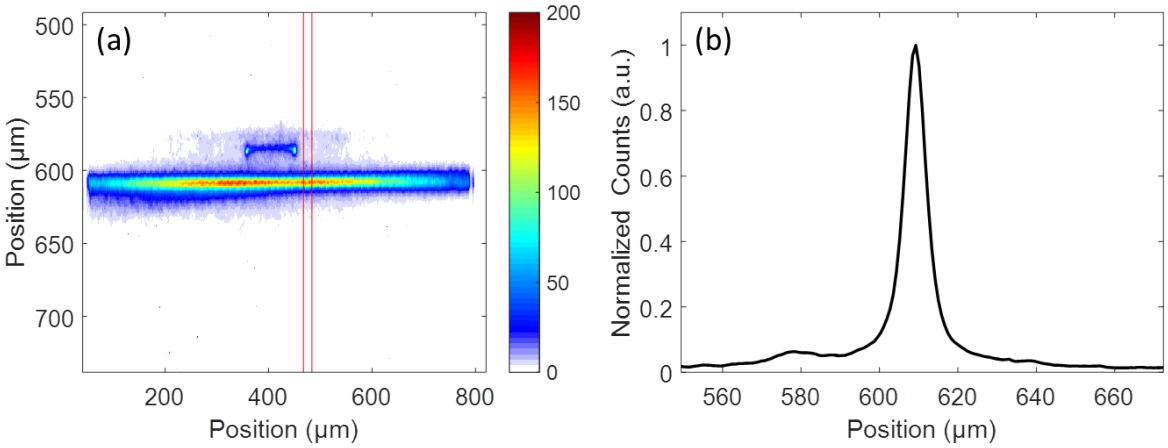

Figure 5.4: a) Spatial distribution of Xe^{1+}, Xe^{2+} and Xe^{3+}, generated by single-photon absorption of photon energies centered at 93 eV. The red lines show the region of integration used to make the lineout. b) Integrated signal over the region shown in red. On average the distribution has a FWHM of 6.5 ± 0.082 μm, which gives an approximate upper limit of 3.1 μm to the focus size.

In addition to the averaging effect, this value is an overestimation of the actual beam size due to the microscope's response to single events. As mentioned in reference [134], a single ion generates a signal of 5.7 ± 0.9 μm in diameter. The measured focus size can be deconvolved from this value to give a FWHM diameter of approximately 3.1 μm, which might still be an overestimation due to the neglected pointing fluctuations.

By using the reflectivity curve of the 93 eV mirror, in addition to the measured spectra it is possible to estimate the XUV energy on target. This is done by normalizing the spectrometer signal to the measured energy with the photodiode. Through this, in addition to the reported efficiency of the grating [118] and the theoretical transmission of zirconium (only one 150 nm thick filter), energies up to 1 nJ are estimated on target.

Knowing the focus size and the energy on target, the intensity at focus can be estimated by assuming a pulse duration of less than 500 as, which is an overestimation of what has been reported previously [52, 53]. It is important to emphasize that in this spectral region the HHG radiation is not an isolated pulse but a few pulses with a half-cycle separation between them. With these values the intensity is estimated to be above 10^{13} W/cm^2, which based on previous measurements done at the FLASH free-electron laser, it should be possible to generate a measurable Xe^{4+} and Xe^{5+} signal [43].

[2] For this measurement the microscope was not calibrated spatially on the same day, so the calibration from reference [134] was used, which is expected to remain approximately constant if the microscope's operating parameters are not changed.

5.3 Two-photon absorption

5.3.1 Xe^{4+} with 93 eV mirror

Two photons are needed from the 93 eV mirror reflected spectrum in order to generate Xe^{4+}. For the detection of this ion, a delay gate width is chosen narrow enough in order to detect a single ionization state. By changing the gate delay, the distribution of Xe^{2+} (generated via single photon absorption) and Xe^{4+} are compared (see figure 5.5). For the Xe^{2+}, the image is acquired with an exposure time of 10 s (100 shots), while for the Xe^{4+} the exposure is increased to 100 s (1000 shots). In order to increase the signal, instead of floating the chamber with xenon the gas nozzle is used (in this measurement and the ones that follow).

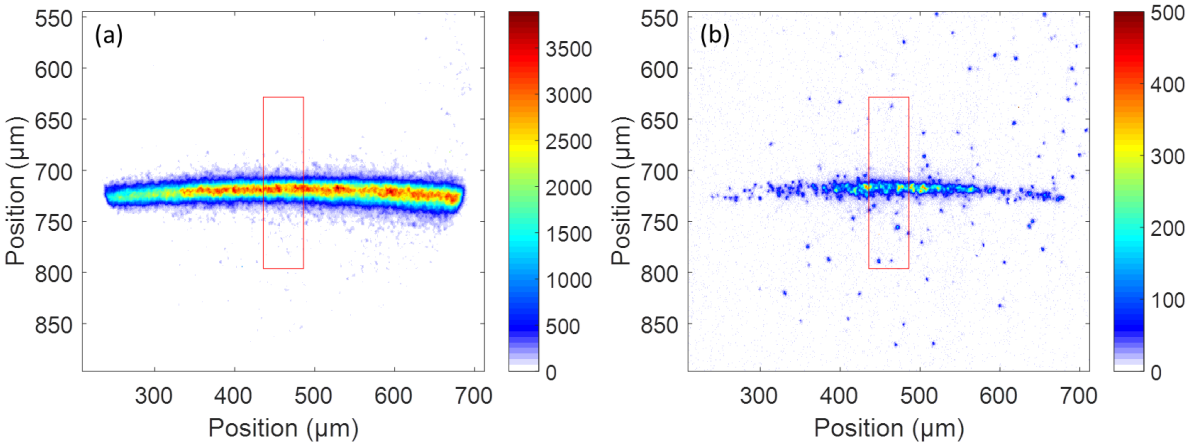

Figure 5.5: Measured spatial distribution for (a) Xe^{2+} and (b) Xe^{4+} with an exposure time of 10 s (100 shots) and 100 s (1000 shots) respectively. The region integrated to measure the number of counts for the z-scan in figure 5.6 is enclosed by the red box.

By qualitatively comparing these two images, the intensity dependence of the Xe^{4+} is already visible. The Xe^{2+} ions are distributed throughout the whole field of view of the microscope, while the Xe^{4+} ions are concentrated towards the center. In order to discard that this is due to spatially inhomogeneous detection efficiency of the microscope, the mirror position is scanned in the beam propagation direction while recording images at the two different delays. Then for each mirror position a region of approximately 50 $\times$ 170 μm^2 is integrated (see regions enclosed in red in figure 5.5). The region is chosen such that longitudinally it corresponds to the step size of the scan, and transversally the beam is inside the region at every longitudinal position of the mirror. Finally the ratio between the integrated signal from Xe^{4+} and Xe^{2+} is plotted against the mirror position, while accounting for the different exposure times (see figure 5.6)).

From the figure, it can be seen that the Xe^{4+} yield is significantly higher when the XUV focus is located at the integration region. This confirms that these ions are generated through nonlinear absorption and that the measured signal does not arise from another mechanism like

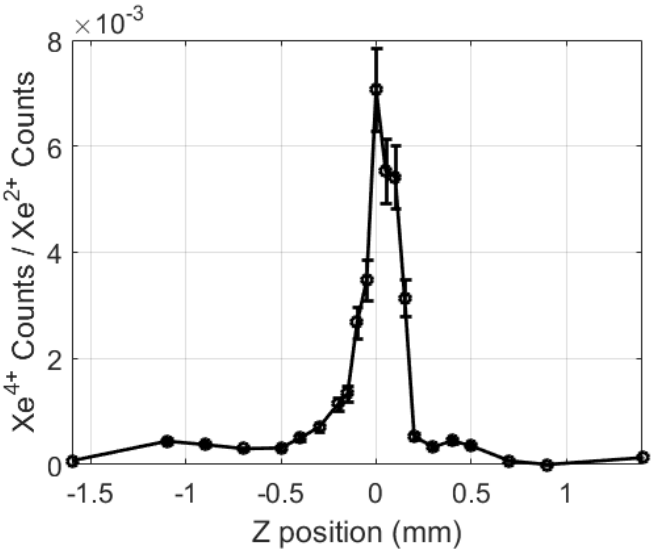

Figure 5.6: Ratio between the Xe^{4+} and Xe^{2+} as a function of the longitudinal position (Z) of the 93 eV focusing mirror. The error bars are the standard deviation of 11% obtained by acquiring 5 images at $Z = 0$.

inhomogeneous detection efficiency, or linear absorption from xenon (the mirror has a slight amount of reflectivity above 111 eV, as shown in figure 5.2) or other background gases.

Knowing that two XUV photons are needed to generate Xe^{4+} it is expected that this process depends quadratically on intensity. The resolution of the microscope is not enough to resolve the changes in beam diameter at different focusing mirror positions, and therefore it is not possible to precisely determine the relative intensity on target in the z-scans. So alternatively, an additional zirconium filter is included which allows to reduce the energy by 53%[3]. The effects of dispersion of this additional filter can be neglected over this bandwidth [135].

By positioning the focusing mirror at $Z = 0$ mm, images are acquired with and without the extra filter, both for Xe^{2+} and Xe^{4+} and then the signal is integrated at the same region as before (see figure 5.7). The exposure times are 10 s and 100 s for Xe^{2+} and Xe^{4+} respectively as before. In order to discard slow drifts of the HHG source during the measurement, 5 alternated images are acquired with and without the extra filter and then separately summed. The error bars correspond to the standard deviation between the images[4]. From these two points a slope of 1.0 ± 0.14 is determined for the Xe^{2+} while a slope of 2.2 ± 0.12 for the Xe^{4+} measurement. Ideally more points should be measured for such an intensity scan, but for the purpose of demonstration this confirms the quadratic dependence of the Xe^{4+} yield with intensity.

The measurement confirms that the Xe^{4+} ion is generated through two-photon absorption

[3]The theoretical transmission of zirconium at 93 eV is 60%, but with the spectrometer a transmission of 53% is measured. This is attributed to a possible inaccuracy on the filters thickness or a thin layer of oxide present on the filters at the moment of the measurement.

[4]From this measurement a standard deviation of 11% is obtained for the ratio between the Xe^{4+} and the Xe^{2+} yield, which is used in figure 5.6

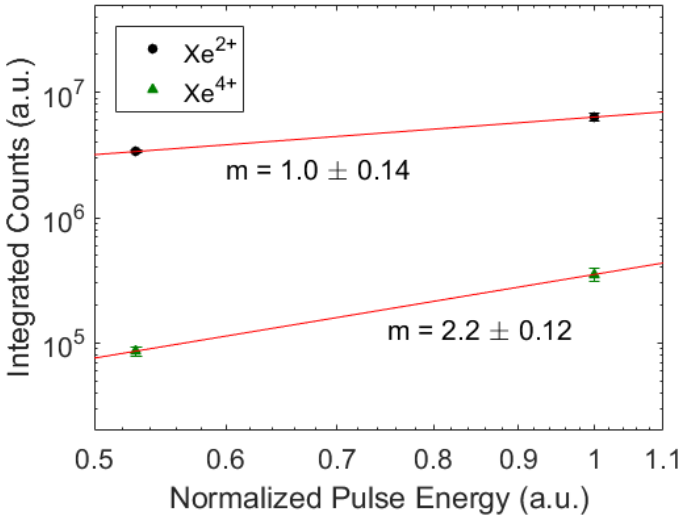

Figure 5.7: Integrated Xe^{2+} (black dots) and Xe^{4+} (blue dots) counts for both one and two zirconium filters. Error bars are the standard deviation of the 5 acquired images. The data points can be fitted to a linear function with slope $m = 1.0 \pm 0.14$ and $m = 2.2 \pm 0.12$ for the Xe^{2+} and Xe^{4+} signal, confirming the Xe^{4+} is generated through the absorption of two photons.

and thus is a suitable candidate for XUV-pump/XUV-probe experiments, through which more information about the ionization mechanism can be obtained. For longer pulses (> 10 fs), the established mechanism for the generation of Xe^{4+} starts with the removal of a single 4d shell electron, which then removes one or two extra electrons through an Auger processes. Then the two- and three-times ionized Xe have a relatively high absorption cross-section to generate the Xe^{4+} (the ion is generated in a *sequential* ionization process). Implicit in this model is the assumption that intermediate excited states do not significantly affect the final ion yields [46]. By carrying a pump/probe experiment additional insight will be gained on the cross-sections of these excited states and their role in the direct two-photon ionization, which is expected to dominate for shorter pulses [136, 137].

5.3.2 Xe^{5+} with 93 eV mirror

For 93 eV photons, the sequential channel is minimized in comparison to the direct channel by studying Xe^{5+} (see figure 5.3). For long pulses (> 10 fs, which is longer than the Auger decay), the main description of Xe^{5+} generation is from first generating Xe^{4+} and then absorbing another photon, making this a higher-order three-photon process [47]. This means the three-photon process is dominant over the energetically-allowed direct two-photon process. However, this intensity dependence is not observed in experiments (a slope of the power dependence of 2.6 instead 3 [43, 46]), which can be attributed to short-lived intermediate states additionally involved in the ionization process, as well to uncertainties in the intensity. Therefore a similar effect as the one observed in reference [32] could be studied, which also allows

an in-situ temporal pulse characterization through an autocorrelation. In this work, the Xe^{2+} yield was measured as a function of pump/probe delay. This was done with photon energies of approximately 20 eV, and given that at least 21 eV are needed to ionize Xe^{1+} to Xe^{2+}, the sequential channel was minimized.

For the case of Xe^{5+}, photon energies below $168-65 = 103$ eV are needed to achieve this, which is partially fulfilled by the 93 eV mirror. The small amount of reflectivity above 103 eV does not allow to completely discard the generation of Xe^{5+} through a sequential channel. Nevertheless in a similar way as for Xe^{4+}, the presence of Xe^{5+} is confirmed (see figure 5.8). As observed in previous experiments [43], the absolute yield is smaller than for Xe^{4+} due to the smaller cross-section. A detailed scan as in the other cases was not performed, but this preliminary result already shows the ion yield dependence on intensity. This confirms the suitability of this ion as a subject for pump/probe experiments and possibly for an autocorrelation.

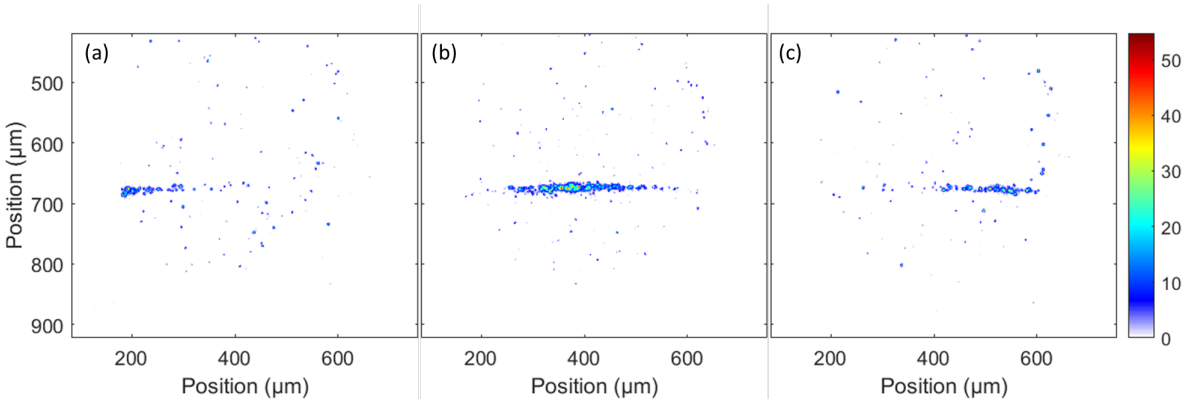

Figure 5.8: Xe^{5+} signal generated with the 93 eV mirror positioned at (a) $Z = -0.8$ mm, (b) $Z = 0.0$ mm and (c) $Z = 0.8$ mm.

5.3.3 115 eV mirror

Without additional gating mechanisms, the continuum region begins at approximately 100 eV (see section 4.4.2). This means that for photon energies below this, the XUV radiation corresponds to a train of attosecond pulses. The 115 eV mirror is used to filter out these lower photon energies for the goal of experiments with isolated attosecond pulses, which however provides approximately 3 times less energy on target. For this measurement the 5 cm cell is used, given it provides slightly higher cutoff and a bigger beam. Otherwise, the Xe^{4+} and Xe^{5+} ion signals are measured in the same way as described in the previous section.

For Xe^{4+}, given that 110 eV are needed for its generation through linear absorption, there is such a contribution to the signal. However, from the cross-section values at these photon energies this contribution is expected to be much smaller, for example, than the Xe^{2+} yield [138]. Figure 5.9 (a) and (b) show the respective Xe^{2+} and Xe^{4+} ion distribution when the XUV focus is positioned at the center of the field of view of the microscope. Xe^{5+} was also

attempted to be measured but the signal was barely distinguishable from a linear background signal (coming from another background gas present in the chamber). This measurement should be repeated while using a narrower gating window for the MCP.

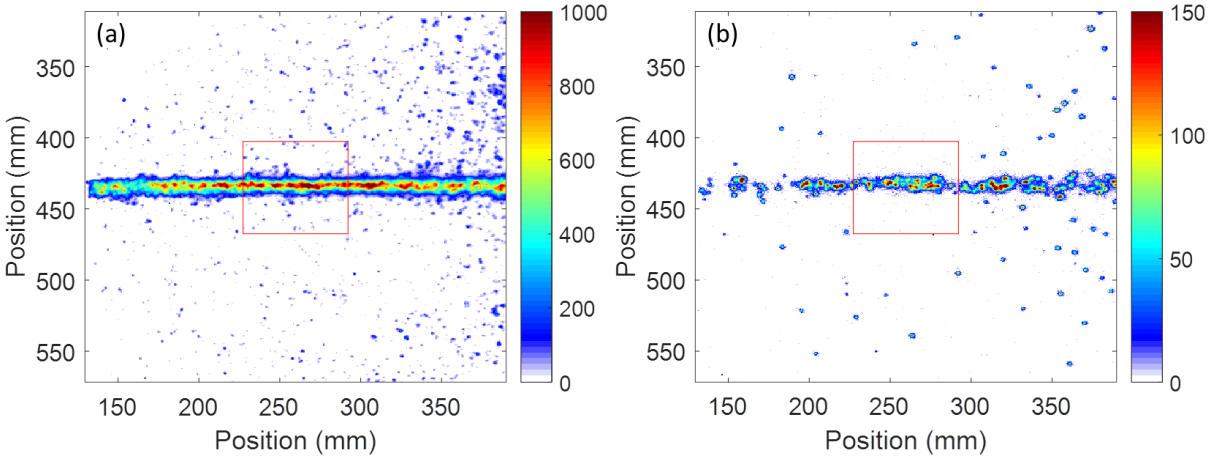

Figure 5.9: Measured spatial distribution for (a) Xe^{2+} and (b) Xe^{4+} with an exposure time of 10 s (100 shots) for (a) and 100 s (1000 shots) for (b), when using the 115 eV mirror. The region integrated to measure the number of counts for the Z-scan in figure 5.10 is enclosed by the red box.

By performing the Z-scan in the same way as previously mentioned, the intensity dependence of the Xe^{4+} signal becomes apparent (see figure 5.10). The error bars corresponds to the standard deviation of 6 images acquired at $Z = 0$, with a value of 18%. This confirms that this ion is a suitable candidate for a pump/probe experiment with the 115 eV mirror. The signal increase at $Z < 0$ is attributed to a slight signal decrease in the Xe^{2+} due to fluctuations.

Although the results presented are still preliminary, they confirm that the XUV energies achieved are enough to generate a measurable signal through the absorption of two photons at the cut-off region. Therefore the measurements are suitable for a XUV-pump/XUV-probe experimental scheme, which together with CEP tagging would allow attosecond temporal resolutions.

All of these images were acquired with 100 s integration time (1000 shots), which would correspond to the measurement time for a single delay step in a pump/probe scheme. For a delay scan of 50 steps, approximately 1.5 hours are needed to complete the measurement. Estimating that for tagging approximately 25% of the shots have the right CEP (depending on the required degree of isolation), a pump/pump measurement with isolated attosecond pulses is within reach thanks to the stability and monitoring capabilities of the source.

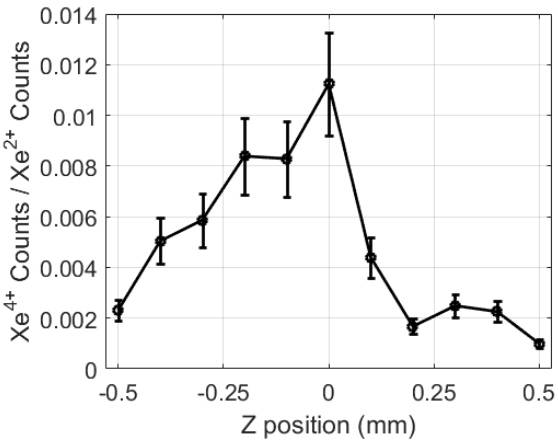

Figure 5.10: Xe^{4+}/Xe^{2+} ratio as a function of the longitudinal position (Z) while using the 115 eV focusing mirror. The error bars corresponds to the standard deviation of 18% measured at the $z = 0$ position.

Chapter summary

- The ion microscope serves as an adequate tool for measuring the ion yield in XUV-pump/XUV-probe experiments. In addition to the properties of a traditional TOF spectrometer, it allows to directly characterize the XUV focus spatial properties and additionally provides a better noise reduction.
- The XUV focus is characterized by measuring the spatial distribution of ions generated by the absorption of a single 93 eV photon. A FWHM diameter of 3.1 μm is estimated, which is on the resolution limit of the microscope. With this focus, intensities above 10^{13} W/cm^2 are expected.
- Xe^{4+} and Xe^{5+} ions, generated through the absorption of two 93 eV photons, are measured. The intensity dependence of the process is confirmed by scanning the focus position in addition to changing the XUV pulse energy on target. This provides a possible candidate for XUV-pump/XUV-probe experiments, though additional gating is necessary to have isolated attosecond pulses in this region
- Xe^{4+} ions, generated through the absorption of two 115 eV photons, are also measured. In this spectral region, isolated pulses are expected for the right CEP, thus allowing a XUV-pump/XUV-probe experiment with attosecond resolution.
- To the best of our knowledge, these measurements constitute the first time a two-photon absorption measurement is performed in this spectral region with a HHG source.

Chapter 6

Summary and outlook

6.1 Summary

The initial step described in this work, was the development of a 16 TW sub-two-cycle OPS, which pushed the frontier of what is achievable at these pulse durations. Starting with a commercially-available front end and pump system, the reached amplification bandwidths were result of the OPCPA technique employed in addition to the two-color pumping approach. After compression, energies above 70 mJ were reached, with a pulse duration of approximately 4.5 fs, making it the most intense few-cycle source currently available. The additional possibility to independently measure the CEP of each shot, makes this system applicable to the generation of intense isolated XUV radiation with attosecond durations.

Several factors were considered for the efficient scaling of the HHG process with the peak powers provided by the OPS, being the driving pulse intensity of utmost importance. The optimal intensity level was reached through a loose-focusing geometry approach, which was implemented in an over 30 m long, evacuated beamline. The experimental setup, besides allowing the use of long focal-length optics, include the necessary elements for the generation, optimization and characterization of the XUV source in a time-efficient manner.

After optimization, broadband XUV pulses centered at 100 eV and with energies above 20 nJ, with an RMS stability of approximately 10% were regularly achieved. Additionally, a continuum of 20-30 eV was observed at the cutoff region, which allow the isolation of isolated pulses with attosecond duration through proper spectral filtering. Due to the high energy and good spatial profile achieved, these pulses can be focused to intensities high enough to probe nonlinear effects. These unprecedented characteristics, in addition to the hour-long stability, allow the use of the source towards novel XUV nonlinear optics experiments.

As a proof-of-principle demonstration of the intensities achieved, the XUV radiation was focused to a < 3.1 μm FWHM diameter spot, which was determined by measuring the spatial distribution of XUV-generated xenon ions with an ion microscope. With the measured pulse energy and focus size an intensity above 10^{13} W/cm^2 was estimated to be reached. Two different mirrors were separately used for focusing the radiation, one centered at 93 eV and the other at 115 eV, with a respective bandwidth of 10 eV and 11 eV. The latter corresponds to the cutoff spectral region from which attosecond pulses can be isolated. At both spectral regions, Xe^{4+} ions were generated (in addition to Xe^{5+} at 93 eV) through two-photon absorp-

tion, which corresponds to the first measurement of this type from a HHG source.

The results presented in this work open up new possibilities in the field of time-resolved XUV nonlinear optics. These processes, until recently were only investigated in FELs, but the increasingly available pulse energies from HHG sources are bringing these research possibilities to laboratories all over the world. The achieved intensities at 100 eV, pave the way towards the unexplored field of time-resolved inner-shell electron dynamics through multiphoton interactions. Until now, these studies were energetically prohibited to HHG sources, due to their low fluxes, and temporally prohibited to FELs, due to their low temporal resolution.

6.2 Outlook

The extension to 16 TW peak-power levels shown in this work is the first demonstration of the scaling capabilities of OPS. Three main development directions can be defined for these type of systems: increase of repetition rate, increase of pulse energy, and increase (or shift) of spectral bandwidth, each offering different advantages for attosecond sources.

The demonstrated nonlinear processes, though quite promising, still suffers from the lack of average signal. This is particularly important for example if tagging is needed, where the effective repetition rate is even lower. Particularly xenon is interesting due to its 'giant' 4d resonance, but other materials with lower cross-sections can also be studied (in realistic measurement times) if higher average fluxes are available. Towards this goal, an upgrade to the LWS-20's pump laser is already planned, where through diode pump technology a repetition rate of 100 Hz can be reached. Effectively this would mean reducing the acquisition times by a factor of 10.

As a future independent approach, yterbium-based thin-disk lasers offer a different alternative towards this goal. The independent demonstration of kW average powers [139] and Joule-level energies [140] opens up the possibility of reaching the necessary pulse energies at higher repetition rates. It is expected that in the near future this technology allows, through the same OPS approach, few-cycle pulses with multiterawatt peak powers at multi-kHz repetition rates [69].

The pulse energy is in principle easily scalable in an OPS, however nonlinear crystal sizes and the pump laser technology currently imposes a limit. For the LWS-20, a pump laser upgrade of additional 2×2.5-3 J of energy is already installed in the system, with the goal of pumping a third pair of OPA stages. BBO crystals with clear-apertures of up to 30 mm are commercially available, which is sufficient for the third pair of OPA stages. Values up to ~ 400 mJ are expected while maintaining or even broadening the amplification bandwidths. Scaling the XUV pulse energy from a gas HHG source might be challenging given the needed focal lengths extension, but it is not fundamentally limited. However, the main application is the scaling of the SHHG sources mentioned in the introduction, which benefit from higher intensities. Focusing to relativistic intensities ($\geq 10^{18}$ W/cm^2) with pulse durations of less than two cycles offer an alternative source of intense isolated attosecond pulses from relativistic overdense plasmas [25, 29, 141, 142].

Without additional pump laser arms, a further bandwidth extension is possible by the use of additional crystals at the current amplification stages [72]. The energy content at both 575 nm and 700 nm can be increased by using a second crystal directly after the second and fourth OPA stages. By using the same pump and tunning the phase-matching angle such that the remaining wavelengths are phase-matched, these spectral regions can be amplified. This technique can both increases the overall energy content and provide < 4 fs pulses. Simulations and experimental investigations for this double-crystal upgrade are currently in progress.

Nevertheless, with extra amplification stages an even bigger step in this direction could be achieved. Amplification and compression has been demonstrated at shorter [143] and longer [144] wavelengths, which could be investigated as a way of extending the LWS-20's bandwidth through additional amplification stages. Extra care should be taken on the seed generation and dispersion management (maybe the parallel-OPS approach is needed), but the result would lead to a octave-spanning spectra, providing an important extension to the attosecond pulse bandwidths.

Despite the possible upgrades that can be implemented to the system, the natural next step with the XUV source is to carry out pump/probe experiments. The separation of the beam can be carried out through a split focusing mirror, which should still provide similar focus characteristics as the ones described. However, a careful beamline design where focusing is achieved through grazing incidence toroidal mirrors, could improve on the < 10% overall reflectivity of the XUV mirror at normal incidence [145, 146].

The spectral filtering necessary for isolated pulses can still be implemented in a grazing incidence configuration, however a broader portion of the XUV spectrum can be used if the generation process is temporally gated [52]. This additionally allows having isolated pulses at different spectral regions, performing novel two-color pump/probe experiments [147], an approach already being pursued in FEL facilities [20, 148, 149].

The overall interest of the scientific community towards this field has recently been represented through the approval of the ELI-ALPS project [150]. This several-hundred million Euro facility dedicated to attosecond physics is expected to provide both high pulse energies and average powers, with photon energies extending up to the keV range. Even more, being a user facility its use will not be only limited to ultrafast laser specialist, who have steered this field until now, but will be open to the general scientific community. In this context, and among other examples, the results presented in this work are a further step towards the establishment of nonlinear attosecond science.

Appendix A

List of Abbreviations

ATI	above-threshold ionization
BSI	barrier-suppression ionization
CEP	carrier-envelope phase
CPA	chirped-pulse amplification
FEL	free-electron laser
GDD	group-delay dispersion
HCF	hollow-core fiber
HHG	high-harmonic generation
IAP	isolated attosecond pulse
LWS-20	Light Wave Synthesizer 20
MCP	micro-channel plate
NIR	near-infrared
NOPCPA	noncollinear optical parametric chirped-pulse amplification
NOPA	noncollinear optical parametric amplification
OPA	optical parametric amplification
OPCPA	optical parametric chirped-pulse amplification
OPS	optical-parametric synthesis
Regen	regenerative amplifier
SH	second harmonic
SHAC	second-harmonic autocorrelator
SHHG	surface high-harmonic generation
TOF	time-of-flight
XPW	cross-polarized wave generation
XUV	extreme ultraviolet

Appendix B

Spectrometer calibration

In order to interpret the measured spectra from the XUV spectrometer, a pixel to photon energy calibration is needed. If aligned properly, the calibration should not differ much from the one provided by the graph in fig 3.18. However, small misalignments lead to big uncertainties in the measured photon energies, particularly for the high energy region.

The calibration involves two steps, an absolute calibration of the spectrometer with respect to a known photon energy, and a relative calibration of the whole range with respect to the absolute reference. To this goal, the XUV radiation from neon and helium coming from the nozzle is used. They radiation is first filtered by the aluminum and silicon filters, which have sharp edges at 73 eV and 100 eV respectively (see figure 3.15). These numbers are used as the absolute reference. An additional 150 nm thick zirconium filter is used in order to eliminate the transmitted IR light through small holes present in the filters.

In what follows, the calibration procedure is explained for a particular camera position, though this procedure needs to be applied accordingly each time the spectrometer is realigned.

By averaging over 100 shots for each filter and using neon as the generation gas, two images are obtained with sharp edges at 73 and 100 eV (see Figure B.1). As described in chapter 4, the line-outs are made over a 10 pixel wide window. From these images the respective position for the edges are found to be at pixel 180 and 308.

Having these two references, the relative calibration is determined by using the fact that the harmonics peaks occur at odd multiples of the fundamental laser photon energy (1.67 eV for this case). The absolute references are then used to determine which peak corresponds to which photon energy. The peaks from the average image with the aluminum filter are used to calibrate the region below 73 eV, and the ones from the silicon filter to calibrate between 73 and 100 eV. In order to observe higher photon energies, only the two zirconium filters are used.

In the same way as before, the peaks are determined for the region above 100 eV. Due to the fact that at higher photon energies the harmonic line energies change with CEP [87], single shots are needed in order to see the peaks clearly (figure B.2 (a)). By using several images and then averaging over the peak positions, this effect is reduced. Additionally, the second order diffraction is used to determine the calibration at the low energy end of the spectrometer.

For calibration at the highest end of the spectrometer, the neon gas is replaced with helium which provides a higher cutoff, and the same procedure is applied (see figure B.2 (b)). The

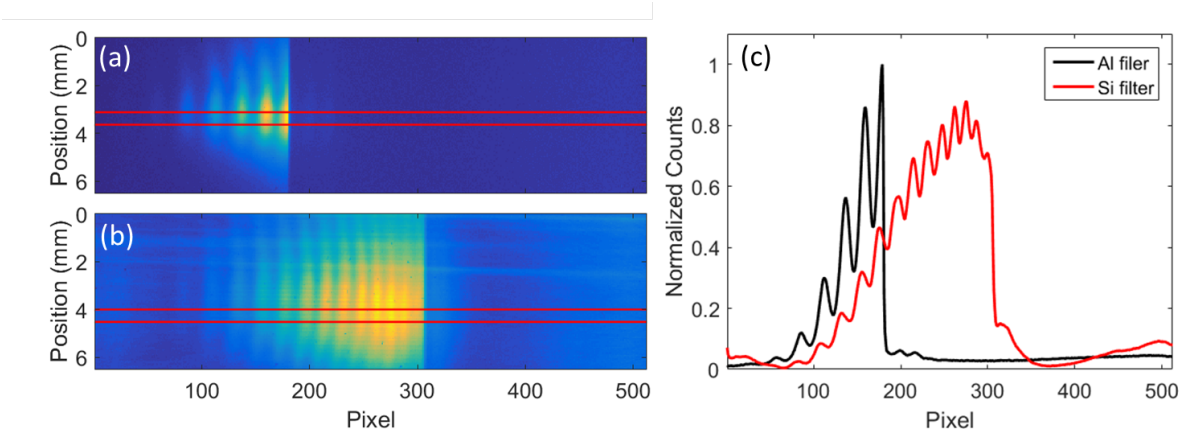

Figure B.1: 100-shot average raw XUV spectra used for calibration, when filtered by an (a) aluminum and a (b) silicon filter, in addition to a zirconium filter. The red lines show the selected region to construct the line-outs. (c) Line-outs of the aluminum- (black) and silicon-filtered (red) spectra. Aluminum cuts at 73 eV and silicon at 100 eV, which correspond respectively to pixel 180 and 308.

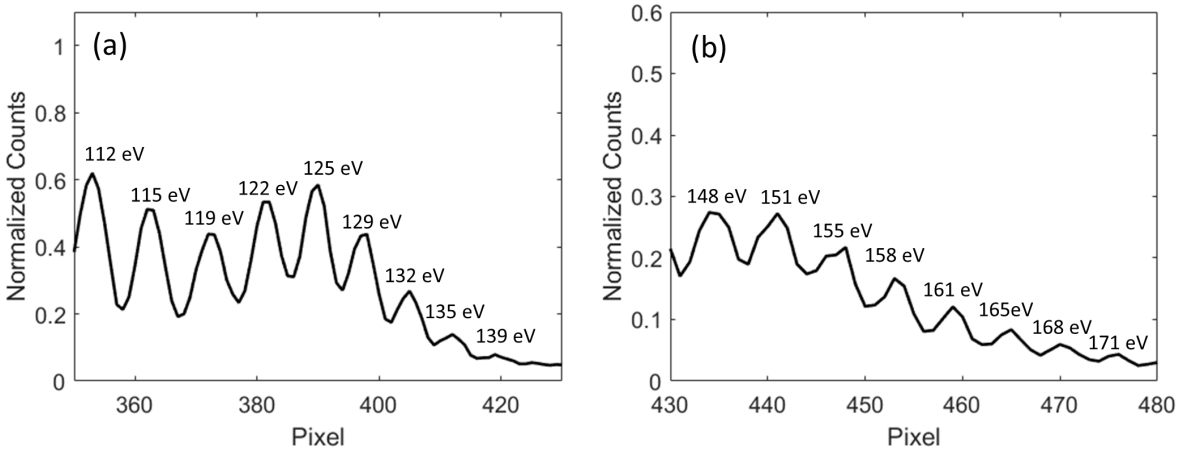

Figure B.2: (a) Spectra used for calibration at the cutoff region when using neon as the generation gas, and the corresponding energy of each peak. (b) Calibration spectra and corresponding energies for helium as the generation gas, which has a higher cut-off energy.

final calibration is determined by doing an extrapolation over the whole detector range.

Appendix C

Correction to measured XUV spectra

In order to produce the plots of XUV spectra presented throughout this thesis, several correction steps are done to the measured raw data. Given the high sensitivity of the XUV CCD, as a first step it is very important to subtract background images to the measured data. A small amount of scattered laser light, or even the lighting in the laboratory might falsify the detected signal. For background measurements, images with the same acquisition conditions are made but with the generation gas turned off.

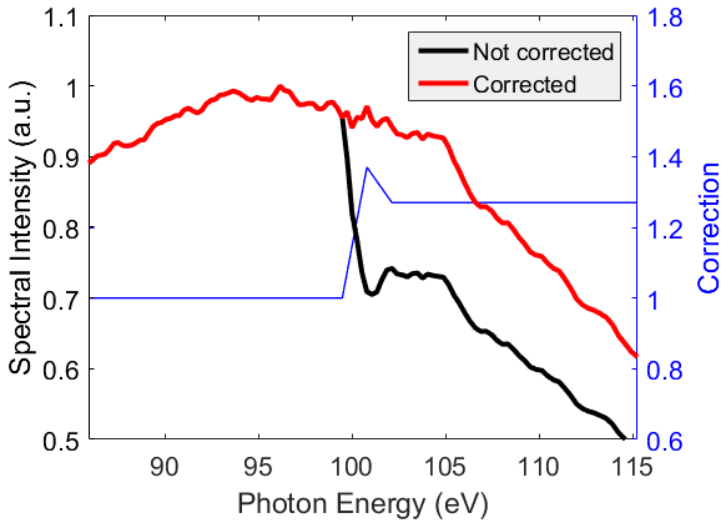

Figure C.1: Measured spectrum before (black curve) and after (red curve) a correction factor (blue curve) is applied in order to account for efficiency loss above 100 eV.

The measured spectra corresponds to the spectral energy density as a function of wavelength. In order to transform this to photon energy space, the well known relation given by $S_\omega(\omega) = S_\lambda(2\pi c/\lambda) \times (2\pi c/\lambda^2)$ is used. A typical measured spectra (integrated in the spatial direction) after these correction are applied is shown as the black curve from figure C.1. For generation the nozzle with helium was used, given that it provides a flatter spectrum at the region around 100 eV. A clear drop in signal is seen at this photon energy, which is attributed to a drop of sensitivity of the XUV camera (Newton, Andor) due to the presence of silicon in the CCD. The reported drop from the camera specification sheet is approximately of 80%, which is not what

is observed in this case. Additionally, a clear dip (strong decrease and then slight increase in signal with increasing photon energy) in the efficiency drop is also observed.

To account for this, a correction factor given by the blue curve in figure C.1 is applied. The corrected spectrum is shown in red in the same figure. This correction factor is applied to every spectrum shown in the the main text, with the respective shift in photon energy, depending on the spectrometer calibration.

Appendix D

Cutoff determination

It is challenging to experimentally determine a cutoff energy which is in accordance to the theoretical definition. In the semiclassical model, the cutoff is defined as the highest possible energy that an electron can acquire during the flight-time, plus the ionization potential. However, experimentally the highest photon energies that are detected depend on other factors such as phase-matching and absorption, in addition to the detector dynamic range and background level.

A straightforward 'experimental' definition of the cutoff is the photon energy at which the signal drops to a certain percent of the maximum, usually like 10-20%. This definition is quite robust and is useful to monitor cutoff energy dependence on a parameter. However, it is not a useful definition in order to estimate the highest photon energy achieved through the generation process, given that the obtained value depends on the used threshold, which is arbitrarily defined.

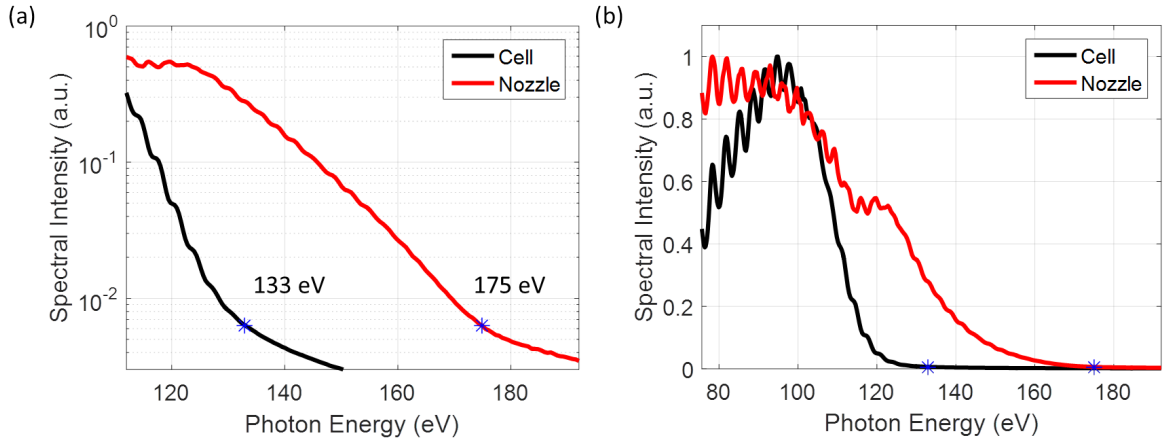

Figure D.1: (a) Spatially integrated spectral intensity as a function of photon energy, plotted on a logarithmic scale. The radiation is generated from neon, while using the gas cell (black) and gas nozzle (red). The cutoff energy is defined as the position where the slope sharply changes, due to the noise being comparable to the measured signal. (b) Same spectra plotted on a linear scale, where the sharp slope change is not clearly visible.

In section 4.3.1, the generation intensity is determined through the cutoff energy, in order to compare to the input intensity. For this estimation, the cutoff is determined as the photon

energy at which the signal reaches the noise level. Theoretically, at the cutoff region the signal drops sharply with increasing photon energy, but in a measured spectrum this occurs only until the noise level is reached. On a logarithmic scale, this is clearly visible as a sharp slope change. Figure D.1 (a) shows two measured spectra from the gas cell and nozzle, for neon as the generation gas. The signal is plotted on a logarithmic scale, where the slope change is marked with a blue star. This position is determined by calculating the inflection point of the curve. For comparison, figure D.1 (b) shows the same spectrum on a linear scale.

The calculated cutoff energy through this definition still depends on the noise level (probably arising from scattered light), but nevertheless provides an estimate of what is the highest photon energy that is detected with the device. By using equation 2.5, a lower limit to the generation intensity can be determined.

Appendix E

Results from other gases

The main goal of the AS6 project was the generation of intense radiation at 100 eV, for XUV-pump/XUV-probe experiments. However, a small portion of the measurement time was spent optimizing other gases, which could be use for experiments at different photon energies. As described in chapter 2, the main effect of changing the gas is a change in efficiency and cutoff: heavier atoms provide higher efficiency but reduced cutoff.

Argon is interesting for experiments around 50 eV and below given that it provides even more energy than neon. Helium provides higher cutoff energies, but with a reduced overall pulse energy. It is important to emphasize that these results are preliminary and could be improved upon in the future. They are described here just as a demonstration, in case a source at other photon energies is needed for future applications.

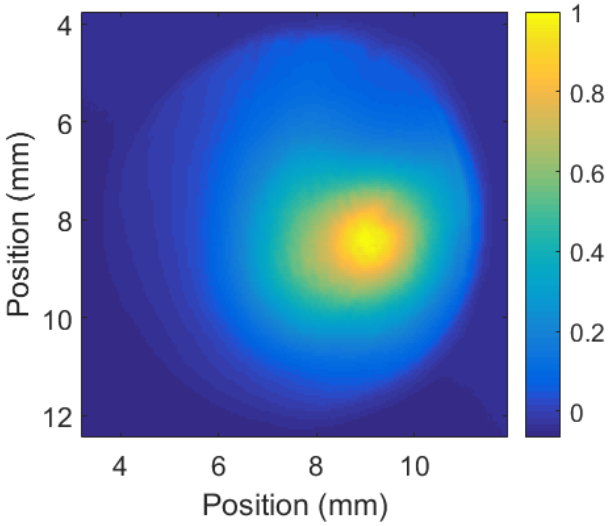

Figure E.1: Centered and averaged XUV beam profile from the 10 cm, filled with argon. The beam reaches a size of 2.6 mm FWHM with a pointing stability of 250 μm. The measured energy corresponds to approximately 300 nJ after generation in the aluminum window.

When argon was tested, the aluminum 200 nm filters used were already in the setup for a long time and a oxide layer was present. In order to measure the filter transmission, the energy is

measured while using the filters both together and separately. This approach underestimates the transmission, given that some NIR light goes through due to the small holes present in the filter. A transmission of 11% and 17% was measured from each filter, much lower than the expected 45%.

Having this issue in mind, from the argon-filled 10 cm long cell, pulse energies above 300 nJ are estimated directly after generation, inside the aluminum window (between 20-70 eV approximately, as shown in figure 3.15). With the spectrometer alignment used, only the cutoff energy was visible, which reached a value above 60 eV. Based on other reported results, the spectral intensity is expected to peak around $30-40$ eV [34, 98, 151].

The beam profile reaches a beam size of 2.6 mm FWHM after the 12 m propagation with a 250 μm RMS pointing stability (see figure E.1). During optimization, the iris was closed down to 39 mm, for which the intensity is still above 10^{15} W/cm^2. Given that the BSI intensity for argon is 2.5×10^{14} W/cm^2, under these conditions the generation process occurs in the depletion regime, similar to the case of neon with the 8 m focusing geometry.

The XUV energy reached in this case is slightly smaller to what has been reported previously ($\sim$ 700 nJ in reference [98] and 800 ± 300 nJ in reference [34]), though in both cases the HHG process was driven with many-cycle laser pulses.

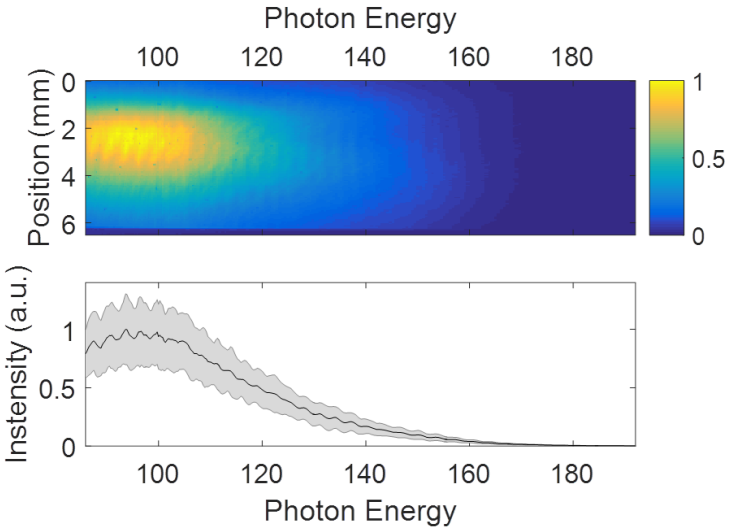

Figure E.2: (a) Averaged XUV spectrum generated with a helium-filled 10 cm gas cell, where photon energies up to 180 eV are reached.

For a helium-filled 10 cm gas cell energies up to 7 nJ were reached in the zirconium window, though with a RMS stability approximately of 25%. From the spectra, a cutoff energy above 180 eV is observed (see figure E.2). The source of these instabilities was not further investigated, though it is expected that for helium the ionization effects are less significant than for argon and thus a better stability should be achieved. Nevertheless, to the best of our knowledge these are the highest pulse energies reported from helium as the generation gas.

To conclude, even though more careful optimization is needed for both argon and helium,

the demonstrated results serve as a lower limit on what is achievable with the current configuration, paving the way towards alternative applications at higher and lower photon energies.

Appendix F

Data archiving

The data and results presented in this thesis can be found on the Data Archive Computer (DAC) of the Division for Attosecond Physics at Max Planck Institute of Quantum Optics for the exception of big raw data files. These are found in the backup drive from Prof. Veisz, located also at the Max Planck Institute of Quantum Optics.

The raw data and Matlab codes are separately stored in a different folder. The data is separated by chapters and figure number. Each figure has a respective 'information.txt' file which includes the date the measurement was performed. If the raw data is not included in the folder, the 'information.txt' additionally includes the name of the relevant file and the respective folder where it is stored. Most of the raw data files are included both in their original format and as a '.mat', in order to make the analysis faster. Each folder includes a Matlab script called 'figure maker.m' which can be run in order to generate the figure. For figures with extra annotations, the final figure is included as a '.png' file.

For the figures in Chapter 4, an additional folder is included with the respective analysis programs for the three XUV characterization devices: the photodiode, spectrometer and profiler. These analysis programs were used for all figures in the chapter, unless another program is provided in the respective folder.

Bibliography

[1] L. Bobis and J. Lequeux. Cassini, Rømer and and the velocity of light. *Journal of Astronomical History and Heritage*, 11(2):97–105, 2008.

[2] B. Clegg. *The Man Who Stopped Time. The Illuminating Story of Eadweard Muybridge: Pioneer Photographer, Father of the Motion Picture, Murderer*. Joseph Henry Press, 2007.

[3] T. H. Maiman. Stimulated Optical Radiation in Ruby. *Nature*, 187(4736):493–494, 1960.

[4] E. P. Ippen, C. V. Shank, and A. Dienes. Passive mode locking of the CW dye laser. *Applied Physics Letters*, 21(8):348–350, 1972.

[5] A. Zewail. Laser Femtochemistry. *Science*, 242(4886):1645–1653, 1988.

[6] A. McPherson *et al.* Studies of multiphoton production of vacuum-ultraviolet radiation in the rare gases. *Journal of the Optical Society of America B*, 4(4):595, 1987.

[7] M. Ferray *et al.* Multiple-harmonic conversion of 1064 nm radiation in rare gases. *Journal of Physics B: Atomic, Molecular and Optical Physics*, 21(3):L31–L35, 1988.

[8] N. Bloembergen. Nonlinear optics and spectroscopy. *Reviews of Modern Physics*, 54(3):685–695, 1982.

[9] M. Hentschel *et al.* Attosecond metrology. *Nature*, 414(6863):509–513, 2001.

[10] F. Krausz and M. Ivanov. Attosecond physics. *Reviews of Modern Physics*, 81(1):163–234, 2009.

[11] W. Ackermann *et al.* Operation of a free-electron laser from the extreme ultraviolet to the water window. *Nature Photonics*, 1(6):336–342, 2007.

[12] T. Shintake *et al.* A compact free-electron laser for generating coherent radiation in the extreme ultraviolet region. *Nature Photonics*, 2(9):555–559, 2008.

[13] P. Emma *et al.* First lasing and operation of an ångstrom-wavelength free-electron laser. *Nature Photonics*, 4(9):641–647, 2010.

[14] C. Bostedt *et al.* Ultra-fast and ultra-intense x-ray sciences: first results from the Linac Coherent Light Source free-electron laser. *Journal of Physics B: Atomic, Molecular and Optical Physics*, 46(16):164003, 2013.

[15] J. Feldhaus *et al.* AMO science at the FLASH and European XFEL free-electron laser facilities. *Journal of Physics B: Atomic, Molecular and Optical Physics*, 46(16):164002, 2013.

[16] M. Yabashi *et al.* Compact XFEL and AMO sciences: SACLA and SCSS. *Journal of Physics B: Atomic, Molecular and Optical Physics*, 46(16):164001, 2013.

[17] H. Chapman *et al.* Femtosecond time-delay X-ray holography. *Nature*, 448(7154):676–679, 2007.

[18] R. Mitzner *et al.* Direct autocorrelation of soft-x-ray free-electron-laser pulses by time-resolved two-photon double ionization of He. *Physical Review A*, 80(2):8–11, 2009.

[19] J. Ullrich, A. Rudenko, and R. Moshammer. Free-Electron Lasers: New Avenues in Molecular Physics and Photochemistry. *Annual Review of Physical Chemistry*, 63:635–660, 2012.

[20] F. Bencivenga *et al.* Multi-colour pulses from seeded free-electron-lasers: towards the development of non-linear core-level coherent spectroscopies. *Faraday discussions*, 171:487–503, 2014.

[21] A. A. Zholents. Method of an enhanced self-amplified spontaneous emission for x-ray free electron lasers. *Physical Review Accelerators and Beams*, 8(4):040701, 2005.

[22] E. Springate and J. W. G. Tisch. High harmonic generation as a seed source for free electron lasers. *Journal of Modern Optics*, 58(16):1351–1361, 2011.

[23] S. Kohlweyer *et al.* Harmonic generation from solid-vacuum interface irradiated at high laser intensities. *Optics Communications*, 117(5-6):431–438, 1995.

[24] S. Gordienko *et al.* Relativistic Doppler Effect: Universal Spectra and Zeptosecond Pulses. *Physical Review Letters*, 93(11):115002, 2004.

[25] G. D. Tsakiris *et al.* Route to intense single attosecond pulses. *New Journal of Physics*, 8(1):19, 2006.

[26] A. Borot *et al.* Attosecond control of collective electron motion in plasmas. *Nature Physics*, 8(5):416–421, 2012.

[27] Y. Nomura *et al.* Attosecond phase locking of harmonics emitted from laser-produced plasmas. *Nature Physics*, 5(2):124–128, 2009.

[28] R. Hörlein *et al.* Temporal characterization of attosecond pulses emitted from solid-density plasmas. *New Journal of Physics*, 12(4):043020, 2010.

[29] P. Heissler *et al.* Two-photon above-threshold ionization using extreme-ultraviolet harmonic emission from relativistic laser-plasma interaction. *New Journal of Physics*, 14(4):043025, 2012.

[30] J. A. Wheeler *et al.* Attosecond lighthouses from plasma mirrors. *Nature Photonics*, 6(12):829–833, 2012.

[31] P. Tzallas *et al.* Second-order autocorrelation measurements of attosecond XUV pulse trains. *Journal of Modern Optics*, 52(2-3):321–338, 2005.

[32] P. Tzallas *et al.* Extreme-ultraviolet pump-probe studies of one femtosecond scale electron dynamics. *Nature Physics*, 7(10):27, 2011.

[33] E. J. Takahashi *et al.* Attosecond nonlinear optics using gigawatt-scale isolated attosecond pulses. *Nature communications*, 4:2691, 2013.

[34] B. Manschwetus *et al.* Two-photon double ionization of neon using an intense attosecond pulse train. *Physical Review A*, 93(6):061402, 2016.

[35] A. Gordon *et al.* Role of many-electron dynamics in high harmonic generation. *Physical Review Letters*, 96(22):9–12, 2006.

[36] D. L. Ederer. Photoionization of the 4d electrons in xenon. *Physical Review Letters*, 13(25):760–762, 1964.

[37] A. P. Lukirskii, I. A. Brytov, and T. M. Zimkina. (Title not available). *Optika i Spectroskopiâ*, 17:438, 1964.

[38] J. B. West. Photoionization of atomic ions. *Journal of Physics B: Atomic, Molecular and Optical Physics*, 34(18):R45–R91, 2001.

[39] J. M. Bizau *et al.* Absolute photoionization cross sections along the Xe isonuclear sequence: Xe3+ to Xe6+. *Physical Review A*, 73(2):022718, 2006.

[40] L. Juschkin *et al.* EUV emission from Kr and Xe capillary discharge plasmas. *Journal of Physics D: Applied Physics*, 35(3):219–227, 2002.

[41] A. Aguilar *et al.* Absolute photoionization cross sections for Xe4+, Xe5+, and Xe6+ near 13.5 nm: Experiment and theory. *Physical Review A*, 73(3):032717, 2006.

[42] C. H. Zhang *et al.* Xenon discharge-produced plasma radiation source for EUV lithography. *IEEE Transactions on Industry Applications*, 46(4):1661–1666, 2010.

[43] A. A. Sorokin *et al.* Photoelectric effect at ultrahigh intensities. *Physical Review Letters*, 99(21):213002, 2007.

[44] V. Richardson *et al.* Two-photon inner-shell ionization in the extreme ultraviolet. *Physical Review Letters*, 105(1):14–17, 2010.

[45] T. Mazza *et al.* Sensitivity of nonlinear photoionization to resonance substructure in collective excitation. *Nature Communications*, 6:6799, 2015.

[46] M. G. Makris, P. Lambropoulos, and A. Mihelič. Theory of multiphoton multielectron ionization of xenon under strong 93-eV radiation. *Physical Review Letters*, 102(3):033002, 2009.

[47] P. Lambropoulos, K. G. Papamihail, and P. Decleva. Theory of multiple ionization of xenon under strong XUV radiation and the role of the giant resonance. *Journal of Physics B: Atomic, Molecular and Optical Physics*, 44(17):175402, 2011.

[48] D. Herrmann *et al.* Generation of sub-three-cycle, 16 TW light pulses by using noncollinear optical parametric chirped-pulse amplification. *Optics Letters*, 34(16):2459–2461, 2009.

[49] P. Heissler *et al.* Toward single attosecond pulses using harmonic emission from solid-density plasmas. *Applied Physics B*, 101(3):511–521, 2010.

[50] P. Heissler *et al.* Few-cycle driven relativistically oscillating plasma mirrors: A source of intense isolated attosecond pulses. *Physical Review Letters*, 108(23):235003, 2012.

[51] W. Helml. *PhD thesis: Development & Characterization of Sources for high-energy, high-intensity coherent Radiation.* Technische Universität München, 2012.

[52] G. Sansone, L. Poletto, and M. Nisoli. High-energy attosecond light sources. *Nature Photonics*, 5(11):655–663, 2011.

[53] M. Chini, K. Zhao, and Z. Chang. The generation, characterization and applications of broadband isolated attosecond pulses. *Nature Photonics*, 8(3):178–186, 2014.

[54] D. Herrmann *et al.* Approaching the full octave: noncollinear optical parametric chirped pulse amplification with two-color pumping. *Optics Express*, 18(18):18752–18762, 2010.

[55] A. Harth *et al.* Two-color pumped OPCPA system emitting spectra spanning 15 octaves from VIS to NIR. *Optics Express*, 20(3):3076, 2012.

[56] D. Rivas *et al.* Next generation driver of intense attosecond sources. *Submitted to Nature Photonics.*

[57] B. Bergues *et al.* Table-top nonlinear optics at 100 eV. *To be submitted to Nature Physics.*

[58] Rivas *et al.* Propagation effects on the generation of intense high-harmonics continua at 100 eV. *In preparation.*

[59] A. Dubietis, G. Jonušauskas, and A. Piskarskas. Powerful femtosecond pulse generation by chirped and stretched pulse parametric amplification in BBO crystal. *Optics Communications*, 88(4-6):437–440, 1992.

[60] A. Vaupel *et al.* Concepts, performance review, and prospects of table-top, few-cycle optical parametric chirped-pulse amplification. *Optical Engineering*, 53(5):51507, 2013.

[61] R. W. Boyd. *Nonlinear Optics*. Academic Press, second edition, 2008.

[62] R. L. Sutherland. *Handbook of Nonlinear Optics*. Marcel Dekker, New York, NY, 2003.

[63] G. Mourou D. Strickland. Compression of amplified chirped optical pulses. *Optics Communications*, 56(3):219–221, 1985.

[64] B. C. Stuart *et al.* Nanosecond-to-femtosecond laser-induced breakdown in dielectrics. *Physical Review B*, 53,(4), 1996.

[65] B. W. Mayer. *Master's thesis: State-of-the-art high power laser development - Observation and control of phase matching in optical parametric chirped pulse amplification*. Technische Universität München, 2011.

[66] D. Herrmann *et al.* Investigation of two-beam-pumped noncollinear optical parametric chirped-pulse amplification for the generation of few-cycle light pulses. *Optics Express*, 18(5):4170–4183, 2010.

[67] M. Th. Hassan *et al.* Optical attosecond pulses and tracking the nonlinear response of bound electrons. *Nature*, 530(7588):66–70, 2016.

[68] S.-W. Huang *et al.* High-energy pulse synthesis with sub-cycle waveform control for strong-field physics. *Nature Photonics*, 5(8):475–479, 2011.

[69] H. Fattahi *et al.* Third-generation femtosecond technology. *Optica*, 1(1):45–63, 2014.

[70] T. H. Dou *et al.* Dispersion control with reflection grisms of an ultra-broadband spectrum approaching a full octave. *Optics Express*, 18(26):27900–27909, 2010.

[71] J. Tan. *Master's thesis: Contrast and Dispersion Management in an OPCPA System*. Ludwig-Maximilians-Universität München, 2016.

[72] P. Weinert. *Master's thesis: Optimization of a high-energy few-cycle optical parametric chirped pulse amplifier system*. Ludwig-Maximilians-Universität München, 2016.

[73] C. Y. Teisset *et al.* Soliton-based pump – seed synchronization for few-cycle OPCPA. *Optics Express*, 13(17):140–142, 2005.

[74] T. Amotchkina *et al.* Stress compensation with antireflection coatings for ultrafast laser applications: from theory to practice. *Optics Express*, 22:30387, 2014.

[75] V. Loriot, G. Gitzinger, and N. Forget. Self-referenced characterization of femtosecond laser pulses by chirp scan. *Optics Express*, 21(21):24879–24893, 2013.

[76] V. V. Lozovoy, I. Pastirk, and M. Dantus. Multiphoton intrapulse interference. IV. Ultrashort laser pulse spectral phase characterization and compensation. *Optics Letters*, 29(7):775, 2004.

[77] A. Baltuška *et al.* Attosecond control of electronic processes by intense light fields. *Nature*, 421(6923):611–615, 2003.

[78] E. Cunningham, Y. Wu, and Z. Chang. Carrier-envelope phase control of a 10 Hz, 25 TW laser for high-flux extreme ultraviolet quasi-continuum generation. *Applied Physics Letters*, 107(20):2013–2016, 2015.

[79] E. J.. Takahashi, Y. Fu, and K. Midorikawa. Carrier-envelope phase stabilization of a 16 TW, 10 Hz Ti:sapphire laser. *Optics Letters*, 40(21):4835–4838, 2015.

[80] T. Wittmann *et al.* Single-shot carrier–envelope phase measurement of few-cycle laser pulses. *Nature Physics*, 5(5):357–362, 2009.

[81] A. M.. Sayler *et al.* Precise, real-time, every-single-shot, carrier-envelope phase measurement of ultrashort laser pulses. *Optics Letters*, 36(1):1–3, 2011.

[82] www.spectra-physics.com.

[83] A. M. Sayler *et al.* Real-time pulse length measurement of few-cycle laser pulses using above-threshold ionization. *Optics Express*, 19(5):4464, 2011.

[84] P. B. Corkum. Plasma perspective on strong field multiphoton ionization. *Physical Review Letters*, 71(13):1994–1997, 1993.

[85] K. C. Kulander, K. J. Schafer, and J. L. Krause. *Dynamics of Short-Pulse Excitation, Ionization and Harmonic Conversion*, pages 95–110. Springer US, Boston, MA, 1993.

[86] M. Lewenstein *et al.* Theory of high-harmonic generation by low-frequency laser fields. *Physical Review A*, 49(3):2117–2132, 1994.

[87] M. Nisoli *et al.* Effects of carrier-envelope phase differences of few-optical-cycle light pulses in single-shot high-order-harmonic spectra. *Physical Review Letters*, 91(21):213905, 2003.

[88] E. Goulielmakis *et al.* Single-cycle nonlinear optics. *Science*, 320(5883):1614–1617, 2008.

[89] W. Holgado *et al.* Continuous spectra in high-harmonic generation driven by multicycle laser pulses. *Physical Review A*, 013816:013816, 2015.

[90] A. Guggenmos *et al.* Aperiodic CrSc multilayer mirrors for attosecond water window pulses. *Optics Express*, 21(19):21728–21740, 2013.

[91] Y. Mairesse *et al.* Attosecond synchronization of high-harmonic soft x-rays. *Science*, 302(5650):1540–3, 2003.

[92] K. Zhao *et al.* Tailoring a 67 attosecond pulse through advantageous. *Optics Letters*, 37(18):3891–3893, 2012.

[93] P. Colosimo *et al.* Scaling strong-field interactions towards the classical limit. *Nature Physics*, 4(5):386–389, 2008.

[94] J. L. Krause, K. J. Schafer, and K. C. Kulander. High-order harmonic generation from atoms and ions in the high intensity regime. *Physical Review Letters*, 68(24):3535–3538, 1992.

[95] V. V. Strelkov *et al.* XUV generation with several-cycle laser pulse in barrier-suppression regime. *Journal of Physics B: Atomic Molecular and Optical Physics*, 39(3):577–589, 2006.

[96] E. Constant *et al.* Optimizing High Harmonic Generation in Absorbing Gases: Model and Experiment. *Physical Review Letters*, 82(8):1668–1671, 1999.

[97] J.a.R. Samson and W.C. Stolte. Precision measurements of the total photoionization cross-sections of He, Ne, Ar, Kr, and Xe. *Journal of Electron Spectroscopy and Related Phenomena*, 123(2-3):265–276, 2002.

[98] E. Takahashi *et al.* Generation of highly coherent submicrojoule soft x rays by high-order harmonics. *Physical Review A*, 66(2):021802, 2002.

[99] P. Rudawski *et al.* A high-flux high-order harmonic source. *Review of Scientific Instruments*, 84(7), 2013.

[100] P. Balcou *et al.* Generalized phase-matching conditions for high harmonics: The role of field-gradient forces. *Physical Review A*, 55(4):3204–3210, 1997.

[101] A. Rundquist *et al.* Phase-Matched Generation of Coherent Soft X-rays. *Science*, 280(5368):1412–1415, 1998.

[102] M. J. Abel *et al.* Isolated attosecond pulses from ionization gating of high-harmonic emission. *Chemical Physics*, 366(1-3):9–14, 2009.

[103] M. V. Ammosov, N. Delone, and V. P. Krainov. Tunnel ionization of complex atoms and of atomic ions in an alternating electromagnetic field. *Journal of Experimental and Theoretical Physics*, 91(6), 1986.

[104] M. Schnürer *et al.* Absorption-Limited Generation of Coherent Ultrashort Soft-X-Ray Pulses. *Physical Review Letters*, 83(4):722–725, 1999.

[105] E. J. Takahashi, Y. Nabekawa, and K. Midorikawa. Low-divergence coherent soft x-ray source at 13 nm by high-order harmonics. *Applied Physics Letters*, 84(1):4, 2004.

[106] J.-F. Hergott *et al.* Extreme-ultraviolet high-order harmonic pulses in the microjoule range. *Physical Review A*, 66(2):021801, 2002.

[107] F. Ferrari *et al.* High-energy isolated attosecond pulses generated by above-saturation few-cycle fields. *Nature Photonics*, 4(12):875–879, 2010.

[108] A. Bouhal *et al.* Temporal dependence of high-order harmonics in the presence of strong ionization. *Physical Review A*, 58(1):389–399, 1998.

[109] T. Pfeifer *et al.* Generating coherent broadband continuum soft-x-ray radiation by attosecond ionization gating. *Optics Express*, 15(25):17120, 2007.

[110] A. Jullien *et al.* Ionization phase-match gating for wavelength-tunable isolated attosecond pulse generation. *Applied Physics B*, 93(2-3):433–442, 2008.

[111] I. Thomann *et al.* Characterizing isolated attosecond pulses from hollow-core waveguides using multi-cycle driving pulses. *Optics Express*, 17(6):4611–4633, 2009.

[112] F. Calegari *et al.* Temporal gating methods for the generation of isolated attosecond pulses. *Journal of Physics B: Atomic Molecuar and Optical Physics*, 45(45):74002–9, 2012.

[113] F. Calegari *et al.* Quantum path control in harmonic generation by temporal shaping of few-optical-cycle pulses in ionizing media. *Physical Review A*, 84, 2011.

[114] K. Schmid. *PhD thesis: Supersonic Micro-Jets and their Application to Few-Cycle Laser-Driven Electron Acceleration.* Ludwig-Maximilians-Universität München, 2009.

[115] B. L. Henke, E. M. Gullikson, and J.C. Davis. Attosecond metrology. *Atomic Data and Nuclear Data Tales*, 54:181–342, 1993.

[116] D. G. Lee *et al.* Coherent Control of High-Order Harmonics with Chirped Femtosecond Laser Pulses. *Physical Review Letters*, 87(24):243902, 2001.

[117] J. J. Carrera and S. I. Chu. Extension of high-order harmonic generation cutoff via coherent control of intense few-cycle chirped laser pulses. *Physical Review A*, 75(3):033807, 2007.

[118] D. Neely *et al.* A multi-channel soft X-ray flat-field spectrometer. *Superstrong Fields in Plasma: First International Conference*, pages 479–484, 1998.

[119] P. Saliéres, A. L'Huillier, and M. Lewenstein. Coherence Control of High-Order Harmonics. *Physical Review Letters*, 74(8), 1995.

[120] C. A. Haworth *et al.* Half-cycle cutoffs in harmonic spectra and robust carrier-envelope phase retrieval. *Nature Physics*, 3(1):52–57, 2006.

[121] P. Ye *et al.* Full quantum trajectories resolved high-order harmonic generation. *Physical Review Letters*, 113(7):073601, 2014.

[122] A. Dubrouil *et al.* Spatio–spectral structures in high-order harmonic beams generated with Terawatt 10-fs pulses. *Nature Communications*, 5:4637, 2014.

[123] P. Tzallas, E. Skantzakis, and D. Charalambidis. Measuring the absolute carrier-envelope phase of many-cycle laser fields. *Physical Review A*, 82(6):061401, 2010.

[124] L. A. A. Nikolopoulos *et al.* Second order autocorrelation of an XUV attosecond pulse train. *Physical Review Letters*, 94(11):113905, 2005.

[125] Y. Nabekawa *et al.* Production of Doubly Charged Helium Ions by Two-Photon Absorption of an Intense Sub-10-fs Soft X-Ray Pulse at 42 eV Photon Energy. *Physical Review Letters*, 94(4):043001, 2005.

[126] S. Kazamias and P. Balcou. Intrinsic chirp of attosecond pulses: Single-atom model versus experiment. *Physical Review A*, 69:063416, 2004.

[127] V. Tosa *et al.* High-order harmonic generation by chirped and self-guided femtosecond laser pulses. I. Spatial and spectral analysis. *Physical Review A*, 71(6):063807, 2005.

[128] V. Tosa, E. Balogh, and K. Kovács. Phase-matched generation of water-window x rays. *Physical Review A*, 80(4):4–6, 2009.

[129] Kaesdorf S. *Geräte für Forschung und Industrie*. Gabelsbergerstr. 59 D-80333 Munich, Germany.

[130] M. Schultze *et al.* Spatially resolved measurement of ionization yields in the focus of an intense laser pulse. *New Journal of Physics*, 13(3):033001, 2011.

[131] B. Bergues *et al.* Spatially Resolved Multiphoton XUV Ionization. *DESY Annual Report*, 2009.

[132] G. Kolliopoulos *et al.* Revealing quantum path details in high-field physics. *Physical Review A*, 90(1):013822, 2014.

[133] N. Tsatrafyllis *et al.* The ion microscope as a tool for quantitative measurements in the extreme ultraviolet. *Scientific Reports*, 6(1):21556, 2016.

[134] A. Muschet. *Master thesis: Characterization of intensive attosecond XUV pulses*. Ludwig-Maximilians-University of Munich, 2016.

[135] E. Gustafsson *et al.* Broadband attosecond pulse shaping. *Optics Letters*, 32(11):1353, 2007.

[136] A. Emmanouilidou, V. Hakobyan, and P. Lambropoulos. Direct three-photon triple ionization of Li and double ionization of Li +. *Journal of Physics B: Atomic, Molecular and Optical Physics*, 46(46):111001, 1110.

[137] P. Lambropoulos, G. M. Nikolopoulos, and K. G. Papamihail. Route to direct multiphoton multiple ionization. *Physical Review A*, 83(2):021407, 2011.

[138] D. M. P. Holland *et al.* Multiple photoionisation in the rare gases from threshold to 280 eV. *Journal of Physics B: Atomic and Molecular Physics*, 12(15):2465–2484, 1979.

[139] J.-P. Negel *et al.* 1.1 kW average output power from a thin-disk multipass amplifier for ultrashort laser pulses. *Optics Letters*, 38(24):5442, 2013.

[140] J. Tümmler *et al.* High-repetition-rate chirped-pulse-amplification thin-disk laser system with joule-level pulse energy. *Optics Letters*, 34(9):1378–1380, 2009.

[141] N. M. Naumova *et al.* Relativistic Generation of Isolated Attosecond Pulses in a λ^3 Focal Volume. *Physical Review Letters*, 92(6):063902, 2004.

[142] G. Ma *et al.* Intense isolated attosecond pulse generation from relativistic laser plasmas using few-cycle laser pulses. *Physics of Plasmas*, 22(3):033105, 2015.

[143] A. Shirakawa *et al.* Sub-5-fs visible pulse generation by pulse-front-matched noncollinear optical parametric amplification. *Applied Physics Letters*, 74(71):2268–3616, 1999.

[144] C. Skrobol *et al.* Broadband amplification by picosecond OPCPA in DKDP pumped at 515 nm. *Optics Express*, 20(4):4619, 2012.

[145] F. Frassetto *et al.* High-throughput beamline for attosecond pulses based on toroidal mirrors with microfocusing capabilities. *Review of Scientific Instruments*, 85(10):103115, 2014.

[146] F. Campi *et al.* Design and test of a broadband split-and-delay unit for attosecond XUV-XUV pump-probe experiments. *Review of Scientific Instruments*, 87(2):023106, 2016.

[147] D. Fabris *et al.* Synchronized pulses generated at 20 eV and 90 eV for attosecond pump–probe experiments. *Nature Photonics*, 9(6):383–387, 2015.

[148] E. Allaria *et al.* Two-colour pump–probe experiments with a twin-pulse-seed extreme ultraviolet free-electron laser. *Nature Communications*, 4:2476, 2013.

[149] E. Ferrari *et al.* Widely tunable two-colour seeded free-electron laser source for resonant-pump resonant-probe magnetic scattering. *Nature Communications*, 7:10343, 2016.

[150] ELI-ALPS, www.eli-hu.hu, august 2016.

[151] Y. Wu *et al.* Generation of high-flux attosecond extreme ultraviolet continuum with a 10 TW laser. *Applied Physics Letters*, 102(20), 2013.

Publications by the Author

D. E. Rivas, A. Borot, D. E. Cardenas, G. Marcus, X. Gu, D. Herrmann, J. Xu, J. Tan, D. Kormin, G. Ma, W. Dallari, G. D. Tsakiris, I. B. Földes, S.-w. Chou, M. Weidman, B. Bergues, T. Wittmann, H. Schröder, P. Tzallas, D. Charalambidis, O. Raszkazovskaya, V. Pervak, F. Krausz, L. Veisz. *Generation Driver for Attosecond and Laser-plasma Physics.* Submitted to Nature Photonics.

D.E. Cardenas, S. Chou, J. Xu, L. Hofmann, A. Buck, K. Schmid, C.M.S. Sears, **D.E. Rivas**, B. Shen, and L. Veisz. *Energy limitation of laser-plasma electron accelerators.* Submitted to Scientific Reports.

D. Rivas, M. Weidman, B. Bergues, A. Muschet, A. Guggenmos, O. Razskazovskaya, H. Schröder, W. Helm, R. Kienberger, V. Pervak, P. Tzallas, D. Charalambidis, F. Krausz, L. Veisz. *Generation of High-Energy Isolated Attosecond Pulses for XUV-pump/XUV-probe Experiments at 100 eV*, High-Brightness Sources and Light-Driven Interactions, HT1B.1, OSA 2016.

D. Rivas, M. Weidman, B. Bergues, A. Muschet, L. Hofmann, O. Razskazovskaya, H. Schröder, W. Helml, G. Marcus, V. Pervak, P. Tzallas, D. Charalambidis, F. Krausz, L. Veisz. *Generation of high-energy isolated attosecond pulses for XUV-pump/XUVprobe experiments at 100 eV*, 2015 European Conference on Lasers and Electro-Optics - European Quantum Electronics Conference, CG_1_3, OSA 2015

Boris Bergues, **Daniel Rivas**, Matthew Weidmann, Hartmut Schröder, Gilad Marcus, Wolfram Helml, Xun Gu, Tibor Wittmann, Reinhard Kienberger, Paraskevas Tzallas, Dimitris Charalambidis, Ferenc Krausz, and Laszlo Veisz. *Production of intense isolated attosecond pulses for nonlinearXUV-XUV pump-probe experiments with 100 eV photons*, Frontiers in Optics 2014, JTu4E.2, 2014 OSA.

L. Veisz, **D. Rivas**, G. Marcus, X. Gu, D. Cardenas, J. Mikhailova, A. Buck, T. Wittmann, C.M. Sears, S.-W. Chou, J. Xu, G. Ma, D. Herrmann, O. Raszkazovskaya, V. Pervak, F. Krausz. *Generation and applications of sub-5-fs multi-10-TW light pulses*, 2013 Conference on Lasers and Electro-Optics Pacific Rim, TuD2_3, IEEE 2013, .

S.-W. Chou, J. Xu, D. Cardenas, **D. Rivas**, T. Wittmann, G. Marcus, F. Krausz, S. Karsch, L. Veisz. *Sub-2-cycle laser-driven Wakefield electron acceleration*, 2013 Conference on Lasers and Electro-Optics - International Quantum Electronics Conference, CG_3_2, IEEE 2013.

Publications by the Author

L. Veisz, **D. Rivas**, G. Marcus, X. Gu, D. Cardenas, J. Mikhailova, A. Buck, T. Wittmann, C.M.S. Sears, J. Xu, D. Hermann, O. Razskazovskaya, V. Pervak, F. Krausz. *Sub-5-fs multi-TW optical parametric synthesizer*, 2013 Conference on Lasers and Electro-Optics - International Quantum Electronics Conference, CG_4_3, IEEE 2013,.

L. Veisz, **D. Rivas**, G. Marcus, X. Gu, J. Mikhailova, A. Buck, T. Wittmann, C.M.S Sears, J. Xu, D. Hermann, V. Pervak, F. Krausz. *Two-Color Pumped Sub-5-fs Multi-TW Optical Parametric Chirped Pulse Amplifier*, Frontiers in Optics 2012/Laser Science XXVIII, FTu5B.4, OSA 2012.

Acknowledgements

Contrary to general impressions, a scientist rarely works alone. Probably more important than the final results of a PhD thesis, are the relationships formed while sharing and discussing with others. I am very grateful for the experiences I had and the marvelous people I met during these last five years. I want to first thank all of you in general for taking part in this important part in my life.

I want to start by greatly thanking Laszlo Veisz for his guidance and patience throughout this time. It is a general fear among young students that their advisor will not be able to provide the necessary support needed for their work. With you this was the opposite! I am grateful for your advice and that you always made the time to discuss and explain with great patience, no matter how dumb the problem was (which was usually the case). I hope this characteristic of you doesn't change now that you are a professor. I am very glad I had the opportunity to get to know you both professionally and personally. The best of luck in your new home, which I hope to visit again in the future. Egészségedre!

I want to also thank Ferenc Krausz for the great opportunity of working in his laboratory. Even though managing such a big group is a daunting task, you always make time for your students. Thank you for your advice and guidance and I hope we have the chance to keep collaborating in the future.

Working with two experienced scientists in the lab can be challenging for a student, specially after midnight! On the other hand, it would have never been possible to learn so much in these years without the experiences I shared with Matthew Weidman and Boris Bergues. I know it is not always easy to work with me, and I am grateful for your patience.

I want to generally thank the whole LWS-20 team for the support during and outside the context of this work. I want to thank Hartmut Schröder and George Tsakiris for the invaluable insights provided. Probably the completion of this work would have been slightly faster, but definitely not as interesting, without the company of Daniel Cardenas. Thank you for the great times! Additionally I want to thank Antonin Borot, Shao-wei Chou, William Dallari, Luisa Hofmann, Dmitrii Kormin, Guangjin Ma, Benedikt Mayer, Julia Mikhailova, Alexander Muschet, Jeryl Tan, Pascal Weinert, Tibor Wittmann and Jiancai Xu, who provided invaluable support throughout this work (both socially and scientifically!).

Great thanks also to the external collaborators who contributed to this work: Balazs Major, Katalin Varjú, Valer Tosa, Wolfram Helml, Reinhard Kienberger, Paris Tzallas and Dimitris Charalambidis. Additionally I want to thank Olga Razskazovskaya, Alexander Guggenmos and Volodymyr Pervak for their support and useful discussions.

Special thanks as well to Mathias Krüger, Olga Lysov, Sabine Keiber, Hanieh Fattahi, Alexan-

der Schwartz, Marcelo Ciappina, Nicholas Karpowicz, Vladislav Yakovlev, Eleftherios Goulielmakis, and Stefan Karsch, who contributed to this work in one way or another.

I want to generally thank the great technical and administrative support offered at MPQ, which was an essential part of this work. In particular, I want to thank Tobias Kleinhenz, Monika Wild, Amu Shrestha, Harald Hass, Anton Horn, Franziska Hoss, Michael Rogg, Tanya Bergues, Wolfgang Huber and Christine Pöschko, who probably had to deal with me a little more than they would have liked to.

Finally I thank my family and friends for their unconditional support throughout these years.